

Aus dem Experimental and Clinical Research Center der Medizinischen
Fakultät Charité – Universitätsmedizin Berlin

DISSERTATION

Investigation of brain extracellular matrix and application of
experimental MRI to understand disease development in a
murine model of multiple sclerosis

Untersuchung der extrazellulären Matrix des Gehirns und
Anwendung experimenteller MRT zum Verständnis der
Krankheitsentwicklung in einem Mausmodell der Multiplen
Sklerose

zur Erlangung des akademischen Grades
Doctor of Philosophy (PhD)

vorgelegt der Medizinischen Fakultät
Charité – Universitätsmedizin Berlin

von

Rafaela Vieira da Silva
aus Rio de Janeiro, Brasilien

Datum der Promotion: 23.03.2024

Table of Contents

List of tables	5
List of figures	6
List of abbreviations	7
Abstract	10
1 Introduction	14
1.1 <i>Multiple Sclerosis</i>	14
1.1.1 Magnetic resonance elastography applied to MS research.....	15
1.1.2 ECM involvement in MS pathology	16
1.2 <i>Motivation and objectives</i>	17
2 Methods	18
2.1 <i>Animals</i>	18
2.2 <i>Experimental autoimmune encephalomyelitis</i>	18
2.2.1 Active EAE	19
2.2.2 Adoptive transfer EAE	20
2.3 <i>In vivo imaging protocol</i>	20
2.3.1 MRE	21
<i>MRE acquisition and parameter maps reconstruction</i>	21
<i>Atlas registration</i>	21
2.3.2 MRI.....	22
2.4 <i>Quantification of GAG disaccharides</i>	22
2.5 <i>Gene expression analyses</i>	24
2.5.1 Genome-wide Microarray	24
2.5.2 Real time quantitative polymerase chain reaction (RT-qPCR)	24
2.6 <i>Histological investigations</i>	25
2.6.1 Imaging Mass Cytometry	25
2.6.2 Immunofluorescence	25
2.7 <i>In vivo study design</i>	26
2.7.1 Study I: Contribution of Tissue Inflammation and Blood-Brain Barrier Disruption to Brain Softening in a Mouse Model of Multiple Sclerosis	26
2.7.2 Study II: Sexual Dimorphism in Extracellular Matrix Composition and Viscoelasticity of the Healthy and Inflamed Mouse Brain	26
2.7.3 Study III: Brain inflammation induces alterations in glycosaminoglycan metabolism and subsequent changes in CS-4S and hyaluronic acid	27
2.8 <i>Statistical assessment and reproducibility</i>	28
3 Results	28
3.1 <i>MRE reveals neuroinflammatory processes beyond BBB-disruption associated with Eu-VSOPs accumulation and tissue remodeling</i>	28
3.2 <i>Basement membrane matrix composition contributes to regional alterations in brain stiffness</i>	32
3.3 <i>Genetic signature of CS degradation followed by altered sulfation profile denote matrix involvement in EAE disease development and progression</i>	33

4	Discussion	39
4.1	<i>In vivo MRE to assess EAE pathophysiology</i>	41
4.2	<i>Neuroinflammation-induced matrix remodeling for disease development.....</i>	45
4.3	<i>Limitations of the studies</i>	48
4.4	<i>Clinical implications and future directions</i>	49
5	Conclusions.....	51
6	Reference list	52
	Statutory Declaration	61
	Declaration of your own contribution to the publications	62
	Publication 1: Contribution of Tissue Inflammation and Blood-Brain Barrier Disruption to Brain Softening in a Mouse Model of Multiple Sclerosis	64
	Publication 2: Sexual Dimorphism in Extracellular Matrix Composition and Viscoelasticity of the Healthy and Inflamed Mouse Brain.....	84
	Publication 3: Brain inflammation induces alterations in glycosaminoglycan metabolism and subsequent changes in CS-4S and hyaluronic acid	102
	Curriculum Vitae	115
	Publication list	117
	Acknowledgments	120

List of tables

Table 1: Structure of 9 standard disaccharides used for HPLC analysis of ChABC digested murine brain samples.23

List of figures

Figure 1: Overview of the neuropathological hallmarks of MS.	15
Figure 2: Experimental design of in vivo studies.	27
Figure 3: Stiffness changes in areas of contrast agent visualization during EAE.....	29
Figure 4: Histological visualization of Eu-VSOPs and the surrounding inflammatory environment by IMC during EAE.	31
Figure 5: Analysis of cortical stiffness changes associated with BM remodeling.	33
Figure 6: Transcriptional analysis of GAG-associated genes in the course of EAE.....	35
Figure 7: GAG disaccharides detection by HPLC.	37
Figure 8: Quantification of the main GAG disaccharide fractions obtained from ChABC digestion of cerebellar samples in the course of EAE.	39
Figure 9: Neuroinflammation-induced changes in brain tissue structure and ECM.....	41

List of abbreviations

BBB – Blood-brain barrier

Bcan – Brevican

BM – Basement membrane

CFA – Complete Freund's adjuvant

Ch – Chondroitinase

ChABC – Chondroitinase ABC

Chst12 – Chondroitin 4-O-sulfotransferase 2

CI – Confidence interval

CNS – Central nervous system

Col1a1 – Collagen type I alpha 1

Col4a1 – Collagen type VI alpha 1

CS – Chondroitin sulfate

Cspg5 – Chondroitin sulfate proteoglycan 5

Dcn – Decorin

DS – Dermatan Sulfate

Dse – Dermatan sulfate epimerase

ECM – Extracellular matrix

EAE – Experimental autoimmune encephalomyelitis

EPI – Echo-planar imaging

Eu-VSOP – Europium-doped very small superparamagnetic iron oxide particles

Fe – Iron

– Fibronectin 1

GAG – Glycosaminoglycans

Gal – Galactose

GalNAc – N-acetylgalactosamine

GBCA – Gadolinium-based contrast agent

Gd – Gadolinium

Glc – Glucosamine

GlcA – Glucuronic acid

Glce – Glucuronic acid epimerase

GlcNAc – N-acetylglucosamine

Gpc1 – Glypican 1

Gpc5 – Glypican 5

Gusb – β -glucuronidase

HA – Hyaluronic acid

Has2 – Hyaluronic acid synthase 2

Hexa – Hexosaminidase α

Hexb – Hexosaminidase β

HS – Heparan sulfate

HPLC – High performance liquid chromatography

Hpse – Heparanase

Hz – Hertz

IduA – Iduronic acid

Idua – α -iduronidase

IMC – Imaging mass cytometry

kg – Kilogram

Lama4 – Laminin subunit alpha 4

Lama5 – Laminin subunit alpha 5

mm – Millimeter

mmol – Milimol

MRE – Magnetic resonance elastography

MRI – Magnetic resonance imaging

MS – Multiple sclerosis

PLP – Myelin proteolipid peptide

PG – Proteoglycan

ROS – Reactive oxygen species

RT-qPCR – Real time quantitative polymerase chain reaction

SI – Signal intensity

Sdn2 – Syndecan 2

VSOP – Very small superparamagnetic iron oxide particles

Abstract

Multiple sclerosis (MS) is a chronic neuroimmunological disease with growing incidence in which autoimmune-driven inflammation leads to damage to the central nervous system and demyelination. Although identification of demyelinating lesions by conventional magnetic resonance imaging (MRI) is paramount for diagnosis and prognosis of MS, the lack of consistent correlation with disease activity and progression motivates the search for complimentary imaging tools. Neuroinflammatory processes, antecedent demyelination and neurodegeneration, are known for exerting a significant effect on extracellular matrix (ECM) composition and can be imaged by MR elastography (MRE) and magnetic nanoparticle-based MRI. Hence, this thesis aimed at using these alternative imaging tools to investigate brain inflammation and the associated remodeling of its ECM. The studies compiled here examined the neuropathological processes behind alterations of the mechanical properties of the brain in association with accumulation of europium-doped very small superparamagnetic iron oxide particles (Eu-VSOP) and remodeling the ECM using the mouse model of MS, experimental autoimmune encephalomyelitis (EAE). Additionally, characterization of alterations in glycosaminoglycans (GAGs) associated with disease development and progression was investigated. The results demonstrated that focal neuroinflammation resulted in microstructural changes affecting the mechanical properties of the brain tissue. Intense perivascular infiltration of inflammatory cell as well as inflammation at the periventricular space visualized by Eu-VSOPs are characterized by marked tissue softening compared with areas of disseminated inflammation. Furthermore, a quantitative mapping of brain stiffness revealed that MRE is able to detect region-specific alterations in tissue microstructure, revealing reduced cortical stiffness at peak EAE. These changes were associated with overexpression of laminin 4 and 5 as well as collagen type VI and downregulation of fibronectin. Finally, changes in GAG composition and metabolism indicate that early alterations in gene expression are followed by modifications in chondroitin sulfate (CS) and hyaluronic acid (HA) GAG fractions. Upregulation of genes associated with GAG degradation and HA synthesis persisted in inflammatory stages but was reduced in the remission phase. In agreement, quantification of CS and HA disaccharides by high performance liquid chromatography showed a reduction of CS-4S, the most abundant CS GAG fraction, and an increase in HA during peak EAE. Taken together, the presented results indicate that *in vivo*

assessment of tissue microstructure using MRE may aid monitoring the pathological processes underlying disease development. Moreover, GAGs remodeling of within the ECM could be interesting targets for development of imaging probes or for interventional therapies able to hinder disease progression.

Zusammenfassung

Multiple Sklerose (MS) ist eine chronisch-neuroimmunologische Erkrankung, bei der autoimmunbedingte Entzündungen zu Demyelinisierung und Schäden im zentralen Nervensystem führen. Grundlage der MS-Diagnose ist die Identifizierung demyelinisierender Läsionen durch konventionelle Magnetresonanztomographie (MR). Diese korrelieren jedoch nicht mit der Krankheitsaktivität, was die Suche nach ergänzender Bildgebung motiviert. Neuroinflammatorische Prozesse, die Demyelinisierung und Degeneration begünstigen, wirken sich auf die Zusammensetzung der extrazellulären Matrix (ECM) aus und können mittels MR-Elastographie (MRE) und nanopartikelbasierter MRT abgebildet werden. Ziel dieser Arbeit war es, diese alternativen Verfahren zur Untersuchung von Inflammation und begleitendem ECM-Umbau im Gehirn einzusetzen. Die zusammengestellten Studien untersuchen anhand des Mausmodells der MS, der experimentellen Autoimmun-Enzephalomyelitis (EAE), neuropathologische Prozesse, die hinter den mechanischen Veränderungen des Gehirns in Verbindung mit der Akkumulation von Europium-dotierten sehr kleinen superparamagnetischen Partikeln (Eu-VSOP) und dem Umbau der EZM stehen. Zusätzlich wurden Glykosaminoglykan(GAG)-Veränderungen charakterisiert, die mit der Krankheitsentwicklung in Verbindung stehen. Die Ergebnisse zeigten, dass fokale Neuroinflammation zu Veränderungen der Mikrostruktur des Hirngewebes und der mechanischen Eigenschaften führt. Die mittels Eu-VSOPs sichtbar gemachte perivaskuläre Infiltration von Entzündungszellen sowie Entzündung im periventrikulären Raum zeichneten sich im Vergleich zu Arealen disseminierter Entzündung durch eine Gewebeerweichung aus. Eine quantitative Kartierung der Hirnsteifigkeit zeigte, dass MRE in der Lage ist, regionsspezifische Veränderungen in der Gewebemikrostruktur zu erkennen, wobei eine verringerte kortikale Steifigkeit während der EAE festgestellt wurde. Diese Veränderungen gingen mit einer Überexpression von Laminin 4 und 5 sowie von Kollagen Typ VI und einer Herabregulierung von Fibronectin einher. Weiterhin deuten Alterationen in der GAG-Zusammensetzung und im Stoffwechsel darauf hin, dass auf eine veränderte Genexpression Änderungen in den GAG-Fraktionen Chondroitinsulfat (CS) und Hyaluronsäure (HA) folgen. Die Hochregulierung von GAG-verwandten Genen hielt während der Entzündungsphasen an, nahm jedoch während der Remissionsphase ab. Die Quantifizierung von CS- und HA-Disacchariden mittels Hochleistungsflüssigkeitschromatographie ergab eine Verringerung von CS-4S und eine

Zunahme von HA zum Höhepunkt der EAE. Insgesamt deuten die Ergebnisse darauf hin, dass die In-vivo-Bewertung der Gewebemikrostruktur mittels MRE die Überwachung der Krankheitsentwicklung und zugrundeliegender pathologischer Prozesse unterstützt. Darüber hinaus sind GAGs, die in der ECM umgebaut werden, interessante Ziele für die Entwicklung von Bildgebungssonden oder für interventionelle Therapien zur Verhinderung der Progression von Krankheiten.

1 Introduction

1.1 Multiple Sclerosis

Affecting 2.8 million people worldwide, multiple sclerosis (MS) is a chronic inflammatory and demyelinating disease of the central nervous system (CNS), that incur a significant impact in the quality of life of young adults [1, 2]. Pathologically, MS is characterized by infiltration of myelin-reactive peripheral immune cells into the brain and spinal cord through disrupted brain barriers, consequently resulting in inflammation with reactive gliosis, demyelination, and neurodegeneration (Figure 1) [3]. Demyelination has been classically considered the key pathological event in MS. The myelin sheath, a lipid-rich material formed around neuronal axons by oligodendrocytes in the CNS, is responsible for insulation, regulation of action potential conduction and metabolic exchange [4]. Therefore, the localization of multifocal demyelinating lesions, which can be visualized by magnetic resonance imaging (MRI), together with other neuropathological processes, such as cortical demyelination, axonal damage and chronic inflammation are determinant for the emergence of cognitive, motor and/or sensory symptoms [5]. The most common MS manifestation among patients is the relapsing-remitting form, manifested in about 73% of patient as repeated intervals of increased neurological disability (relapse) followed by a recovery phase (remission) [6]. The progressive forms include the secondary progressive MS, which derives from an initial relapsing-remitting form that gradually worsens and is present in roughly 18% of patients, while in primary progressive MS, a continuous clinical worsening progresses without periods of remission affecting 8% of patients [6].

Combined with the development of clinical symptoms and laboratory findings, radiological assessment of lesion formation constitutes the basis of MS diagnosis [1, 7]. Existing MRI tools in clinical settings allow for the detection of established or ongoing demyelination (hyperintense regions in T2-weighted images) and assessment of inflammation-associated blood-brain barrier (BBB) breakdown is detected by gadolinium (Gd)-based contrast agents (GBCAs) in T1-weighted images [8]. However, a range of pathological features, especially inflammatory events, remains poorly examined. Furthermore, a dissonance between radiological findings and clinical events, called the clinical-

radiological paradox [9], remains a challenge in monitoring MS disease progression and at the same time fosters investigation of new imaging tools.

Neuropathological features of MS

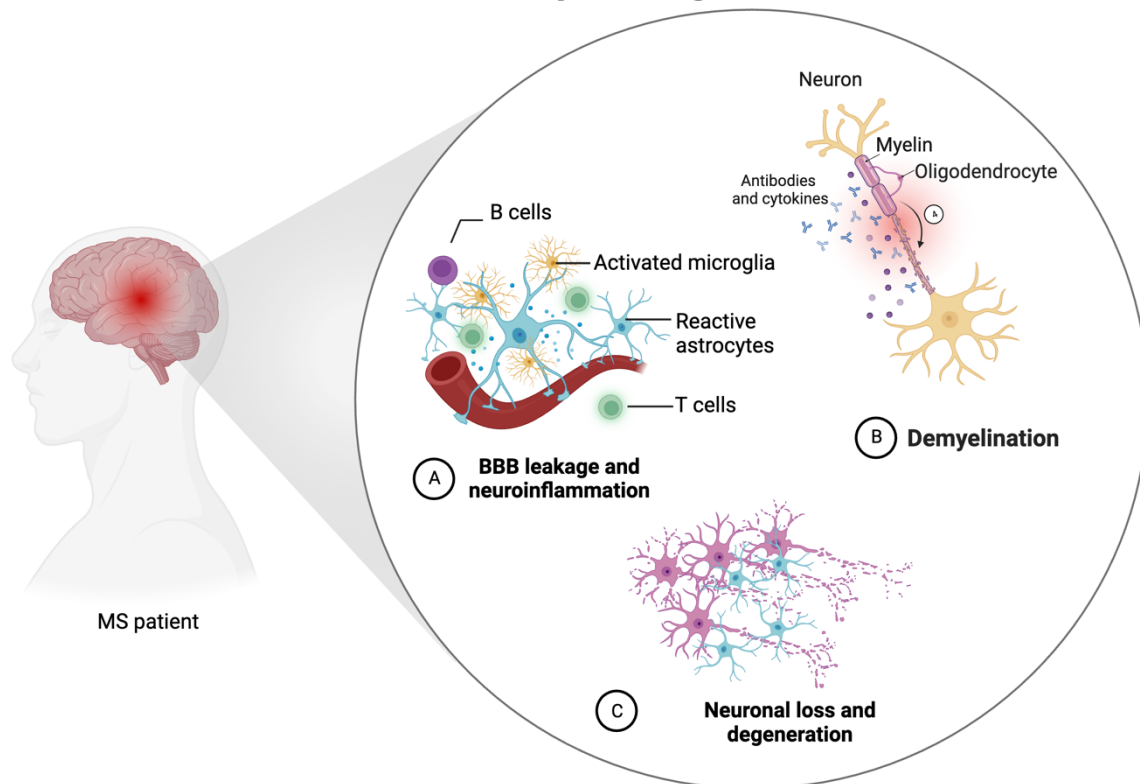


Figure 1: Overview of the neuropathological hallmarks of MS. Myelin reactive T cells as well as antibody producing B cells migrate from the periphery into the CNS via a disrupted BBB leading to inflammation (A) and demyelination (B). Following inflammation, demyelination mediated by autoantibodies and sustained production of inflammatory cytokines lead to myelin degradation and loss of oligodendrocytes (B), ultimately resulting in axon degeneration and neuronal cell loss (C). BBB- blood-brain barrier. (own representation: Rafaela Vieira da Silva, Adapted from “Histopathological Features of Parkinson’s Disease and Alzheimer’s Disease”, by BioRender.com (2022)).

1.1.1 Magnetic resonance elastography applied to MS research

To bridge the gap between radiological findings and the course of neuroinflammatory processes in the brain, magnetic resonance elastography (MRE) has emerged. MRE is a quantitative experimental MRI-based tool that uses vibrations to propagate shear waves into the brain. MRE examines the mechanical properties of the tissue, such as stiffness and fluidity, which can be deduced from shear wave speed (SWS or c) and loss angle (ϕ), respectively [10]. Accumulating evidence has consistently proven MRE as a useful imaging tool to detect pathological softening of the brain tissue under neuroinflammatory conditions such as the ones observed during MS [11-13], Alzheimer’s disease [14], and Parkinson [15]. Subsequent studies using the experimental autoimmune

encephalomyelitis (EAE) mouse model of MS have corroborated human findings and reaffirmed the translational value of the model [16-18]. Compared to imaging of GBCA enhancement, MRE does not require administration of contrast agents, posing as a safe noninvasive technique for detection of pathological damage to the tissue. Although mechanistic understanding of altered brain stiffness is elusive, studies in EAE suggested that brain softening is influenced by inflammatory processes. During EAE, brain stiffness correlated with the expression of CD3, a lineage marker of T cell, and F4/80, a macrophage marker [16, 17]. More recently, the extracellular matrix (ECM) component, fibronectin, was associated with brain softening during EAE [18], pointing at the relevance of non-cellular alterations in brain tissue microstructure during neuroinflammation.

1.1.2 ECM involvement in MS pathology

The ECM of the CNS is responsible for homeostasis and maintenance of vital brain functions, including cell-cell interaction, axonal growth, synaptic plasticity, and binding of growth factors [19-26], besides integrating the brain barriers, such as BBB and cerebrospinal fluid-barrier. The brain matrix is composed of glycosaminoglycans (GAGs), proteoglycans (PGs) and glycoproteins. GAGs are linear carbohydrate polymers made of repeating disaccharide subunits of a uronic acid (iduronic acid or glucuronic acid) and an N-sulfated or N-acetylated hexosamine and the main GAGs in the brain ECM are chondroitin sulfate (CS) and hyaluronic acid (HA) [27-29]. GAGs present highly sulfated structures and are found covalently linked to core proteins forming structurally diverse PGs, with the exception of HA. As a result of structural diversity as well as sulfation pattern, different GAGs and PGs structures exert distinct biological functions [27].

In MS, CSPGs and HA have been shown to be altered and to regulate inflammatory processes. Histological analysis of MS brains revealed the accumulation of CSPGs, including aggrecan, as well as dermatan sulfate (DS) PGs in sites of active demyelinating lesions [30], whereas HA was accumulated in chronic demyelinating lesions [31]. These changes in ECM composition seem to orchestrate key events in disease development and progression. Enhanced proinflammatory response and T cell trafficking was shown to be induced by accumulated HA in EAE [32]. Moreover, suppression of CSPGs synthesis mitigated the signs of EAE in mice and impaired remyelination *in vitro* [33]. Even though the acknowledgment of the ECM contribution to MS pathology is growing, the understanding of its complex compositional changes during disease progression is still lacking.

1.1.2 ECM and magnetic nanoparticle imaging

Moreover, in MS, to reach the brain parenchyma, myelin-reactive peripheral immune cells must not only cross the brain barrier but also overrun the associated ECM [34]. Previous studies showed that very small superparamagnetic iron oxide particles (VSOPs) can be used as contrast agent in MRI (hypointense areas in T2*-weighted images) to visualize inflammatory events beyond BBB disruption, which is generally detected by GBCA [18, 35-37]. During neuroinflammation, these particles were found distributed within perivascular cellular infiltrates, co-localized with endothelial cells and associated with the choroid plexus [36, 38]. Using brain derived endothelial cells, Berndt *et al.* demonstrated that VSOPs uptake under inflammatory conditions was abrogated in the presence of an inflammatory stimulus and sodium chlorate, a GAG sulfation inhibitor [38]. As inflammation-induced changes in GAGs may mediate particle binding and uptake, changes in the brain matrix could be potentially used to monitor EAE disease development as well as to be targeted to hinder disease progression. Characterizing the changes in GAG structures is of utmost importance for the comprehension of the temporal development of tissue remodeling associated with neuroinflammatory processes.

1.2 Motivation and objectives

The lack of imaging markers that reliably reflect the progression of neuroinflammation in MS motivated this thesis. With this purpose, the main goal was to apply MRI-based tools to investigate the course of neuroinflammation through brain tissue properties and ECM remodeling. Experimental MRI tools such as cerebral MR- elastography and/or magnetic nanoparticle imaging may provide valuable information about the neuroinflammatory processes governing disease development and progression. Within this context, the present thesis contemplates the complexity of MS pathophysiology and combines an interdisciplinary approach to study how the brain structure and its mechanical properties are influenced by neuroinflammation using the EAE model. In addition, the relationship between neuroinflammation-driven alterations of GAG metabolism as well as GAG structural modifications and disease progression is investigated. Hence, three studies are presented with the specific objectives to:

- (I) use experimental MRI tools such as MRE and magnetic nanoparticle-based MRI combined with Gd-based MRI to assess the contribution of

- specific neuroinflammatory processes to alterations of the mechanical properties of the brain during EAE (**Study I**);
- (II) quantitatively map neuroinflammation-induced alterations of brain stiffness in association with ECM composition (**Study II**);
 - (III) investigate alterations in GAGs metabolism and composition associated with the course of EAE (**Study III**).

2 Methods

This section will provide the rationale and a summary of the methods used in the publications encompassed in this thesis. For detailed material and methods, refer to the original publications [39-41].

2.1 Animals

All animal experimentation, conducted in the three studies described within the scope of this thesis, were approved by the Berlin State Office for Health and Social Affairs (LAGeSo) with the registration number G106/19 and adhered to both international and national guidelines regarding welfare and handling of laboratory animals.

2.2 Experimental autoimmune encephalomyelitis

In the present publications, the EAE model was used to investigate neuroinflammatory changes in the mouse brain. EAE is a versatile MS model that can be induced in a variety of species, including different types of rodents and monkeys. The successful employment of EAE in drug discovery and development translated to clinical settings owes to its ability to mimic the main cellular and molecular mechanisms present in the various forms of MS pathology [42, 43]. Different from the human disease, the pathogenesis of EAE is artificially induced by immunization with known CNS immunogens, a myelin peptide or CNS tissue homogenate, whereas in MS the etiology is unknown. The pathophysiology developed in EAE after immunization appears to coincide with the human form of the disease, which can be explained by the three-compartment hypothesis [42]. Briefly, self-reactive T cells are induced in the 'afferent compartment' (spleen and lymph nodes) by myelin antigens injected during immunization, migrate to the 'target compartment' (CNS), resulting in inflammation and demyelination after re-activation by local antigen presenting cells. Finally, drainage of debris generates new autoreactive T cells in a 'CNS draining

compartment'. Recent studies indicate a role of tertiary lymphoid organs and lymphatic vessels in the meninges in this process [44, 45].

Determinant factors to produce MS-like encephalomyelitis lie on the choice of auto antigen and the strain selected. SJL mice immunized with the myelin-derived proteolipid peptide 139-155 (PLP₁₃₉₋₁₅₅), the model of choice in studies presented in this thesis, develop a relapsing-remitting MS-like disease, which is characterized by periods of active inflammation and signs of disease disability followed by attenuated inflammation and recovery [46, 47]. Most importantly, EAE in the SJL mice mainly produces infiltration of T-cells, but also of macrophages and B cells, into the CNS. These cells invade both spinal cord and brain structures, affecting cerebellum, brainstem, perivascular areas and the cortex [42, 48]. Following the initial neuroinflammatory lesions, gliosis and axonal damage are common features of EAE [43]. Such as in the prototypical disease, with a prevalence ratio of 4 females to every male patient [2], EAE development in the SJL mice also displays a sexual preference with higher incidence in female mice [47]. Thus, this form of pathology makes the SJL model ideal for imaging studies of the brain during different neuroinflammatory phases of the disease and across sexes.

2.2.1 Active EAE

For Studies I, II and III active EAE was induced in SJL mice. Therefore, 9 - 12-week-old mice (Janvier, SAS, France) were subcutaneously immunized with an emulsion containing 250 µg of a PLP₁₃₉₋₁₅₁, 800 µg *M. tuberculosis* H37Ra (Difco, USA) and 100 µl of complete Freund's adjuvant (CFA; Thermo Fisher Scientific, USA) in addition to an intraperitoneal injection of 250 ng pertussis toxin (List Biological Laboratories, USA) on the same day and 2 days later. The number and sex of mice included in each study can be found in the section 2.7 *In vivo study design*. After induction, the mice were examined on a daily basis for detection of disease signs and scored based on a disability scale according to the following criteria: 0.5 (tail paresis), 1.0 (tail plegia or tail paresis + righting reflex weak), 2.0 (hind limb paresis), 3.0 (hind limb plegia), 4.0 (forelimb paresis or plegia), and 5 (moribund or dead). Observing the animal welfare guidelines and the humane endpoints established in our approved study protocol, mice presenting a score higher than 3 were immediately removed from the study and euthanized. The number of mice removed from each experiment is given in the original publications [39-41].

2.2.2 Adoptive transfer EAE

For **Study I**, the adoptive transfer EAE model was also induced, producing a more severe disease with a faster, synchronous onset [38, 47]. From a cohort of mice with active EAE (donors), induced as described above, PLP-reactive T cells were obtained from the axillary and inguinal lymph nodes collected on day 10 post-immunization. T cells from the donors were cultured for 4 days supplemented with RPMI medium (100 units/ml penicillin, 2 mM L-glutamine, 10% fetal bovine serum, and 100 µg/ml streptomycin) (Difco, USA) complemented with 12.5 µg/ml PLP, to restimulate the cells. After harvesting, 30 million cells were transferred intraperitoneally into healthy animals (recipients). Adoptive transfer EAE mice were scored as described in section 2.1.1.

2.3 *In vivo* imaging protocol

By exploiting the benefits of the MRI, this thesis employed MR-based tools to investigate *in vivo* the development of pathological alterations in the brains of EAE mice noninvasively. ¹H-nuclear magnetic resonance is the principle by which clinical MRI scanners operate, creating non-invasive images of soft tissues. MR signal is generated by manipulating the macroscopic magnetic moment of protons contained within a given tissue by a strong, external magnetic field (\mathbf{B}_0) [10]. Briefly, in the presence of \mathbf{B}_0 , the proton spins (generally randomly orientated) precess about the field direction (z plane) to align with it. By introducing a short radiofrequency pulse, matching the precession frequency, the direction of the magnetization of the protons changes its course away from the longitudinal (z) plane along \mathbf{B}_0 , pulling them towards the transverse (xy) plane. The MR signal results from the current induced during the precession by the transverse magnetization at the receive coil [49]. The return time of the spins to the original alignment to \mathbf{B}_0 after the pulse is switched off is of note. Named relaxation, this return time to the resting position can be divided in two types: a longitudinal (T1) relaxation time and a transverse (T2) relaxation time, unique for every type of body tissue [49]. Introducing paramagnetic ions into the imaged tissue, such as Gd^{3+} or $\text{Fe}^{2+,3+}$ changes the relaxation times of the protons and is applied for contrast imaging. Conventionally, the shortening in T1 relaxation time and consequent increase in signal intensity provoked by GBCAs is used to visualize Gd enhancement, while loss of signal induced by superparamagnetic iron oxide particles is detected with T2-weighted imaging [50].

All *in vivo* brain imaging was acquired through ParaVision 6.1 software coupled to a 7 Tesla BioSpec preclinical animal scanner (Brucker, Germany) using a 20-mm diameter 1H-RF quadrature volume coil (RAPID Biomedical, Rimpar, Germany). During *in vivo* imaging, the animals were placed in a customized animal holder, as described in Silva *et al.* [39], inserted in a 7 Tesla preclinical animal scanner (BioSpec, Brucker, Germany) using a 20-mm diameter 1H-RF quadrature volume coil (RAPID Biomedical, Rimpar, Germany). Anesthesia was induced using 1.5 - 2% isoflurane delivered in a mixture of 30% O₂ and 70% N₂O and maintained during the experimentation via a nose mask integrated to the animal holder. Body temperature was monitored via a rectal probe and maintained constant through a warm pad with temperature-regulated water circulating. Respiratory rate was constantly monitored using a pressure-sensitive pad positioned on the dorsal thorax.

2.3.1 MRE

MRE acquisition and parameter maps reconstruction

Shear waves were generated via a non-magnetic piezoceramic actuator built into the customized animal holder and transmitted to the head cradle, as described in the original publication [39]. Multifrequency MRE was acquired using the following frequencies: 1000 Hz, 1100 Hz, 1200 Hz, 1300 Hz, and 1400 Hz. Seven coronal slices were obtained by a single-shot EPI sequence with the imaging parameters described in the original publications. For **Studies I** and **II**, reconstruction of MRE wave images into the parameter maps of stiffness (shear wave speed or c) and fluidity (phase angle or φ) using tomoelastography post-processing was carried out as established by Bertalan *et al.* [51].

Atlas registration

MRE parameter maps acquired for **Study I** were registered to a T2-weighted RARE image previously transferred to the Allen Mouse Brain Atlas (Allen Institute for Brain Science, United States) space using ANTX, a custom-based MATLAB toolbox [52] as detailed in the original publication [39]. Briefly, MRE parameter maps were 3D-coregistered to T2-weighted images and 2D-slice wise registered, resulting in the interpolation of the 7 MRE slices to the 215 slices in the reference atlas space [53]. This process generated approximately 58 MRE slices in the atlas space. With this approach it was possible to quantify the mechanical properties of tissue in areas of Eu-VSOP accumulation and GBCA-enhancement. To determine MRE parameter values in areas of

Eu-VSOP accumulation, masks were drawn on post-contrast T2*-weighted images with the ANALYZE 10.0 software (Biomedical Imaging Resources Mayo Clinic) using the pre-contrast image as negative reference. For areas of GBCA-enhancement, an image with the percentage changes in signal intensity (SI) was created with the following calculation: $(SI_{T1pre} - SI_{T1post})/SI_{T1pre}$ on ImageJ v. 1.52e (National Institutes of Health, United States). All contrast agent masks were then registered to the reference mouse brain atlas. Intersecting areas between Eu-VSOP and GBCA masks were removed from each other to generate masks exclusively corresponding to a single contrast agent. Incidence maps were generated with ANTx based on contrast agent distribution masks to display the prevalence of Eu-VSOP or GBCA across the brain regions and averaged shear wave speed (c) and phase angle (ϕ) values were extracted for the corresponding masks using MATLAB v. 9.4 (MathWorks, USA).

In **Study II**, masks of regions of interest within the brain were manually and blindly delineated on reconstructed MRE parameter maps based on a reference anatomical image using MATLAB v. 9.4 (MathWorks, USA). Averaged shear wave speed (c) and phase angle (ϕ) values were extracted for areas corresponding to cerebral cortex, thalamus, hippocampus and whole brain masks by overlaying the corresponding masks onto the MRE parameter maps using MATLAB v. 9.4 (MathWorks, USA).

2.3.2 MRI

In **Study I**, a coronal T2-weighted 2D-RARE image was obtained as an anatomical reference for the elastography, in addition to a T1-weighted RARE sequence with matching geometry for GBCA-enhanced images. For visualization of Eu-VSOP accumulation, a T2*-weighted FLASH was acquired with the same geometry as the T2-weighted images. T2-weighted RARE and the pre-contrast images were registered to the reference atlas using the ELASTIX tool [54] and, using affine transformation, pre- and post-contrast images were co-registered, then resliced to the T2-weighted RARE. Further details about imaging can be found in the original publication [39].

2.4 Quantification of GAG disaccharides

Due to its complex arrangement and macromolecular composition, the study of the ECM presents numerous challenges, especially concerning isolation and quantification of glycoconjugates. Differently from proteins, structure of glycoconjugates, namely GAGs and PGs, is non-template driven and is dependent on complex synthetic as well as

metabolic reactions involving epimerases, *N*-acetyltransferases, sulfotransferases, and sulfatases [27]. To analyze GAGs in brain samples, a fluorescent labeled disaccharide analysis after enzymatic digestion with chondroitinase (Ch) ABC was applied [55]. In **Study III**, GAGs were extracted from cerebellum, midbrain and forebrain, as described in the original publication [41], and 200 µg of total proteins were then enzymatically digested with ChABC, cleaving CS, DS and HA GAGs into disaccharide subunits via β-elimination of glucuronic acid (GlcA) and iduronic acid (IduA) residues. In the resulting disaccharide mixture, an unsaturation is formed at carbon 5, removing the isomerism between IduA and GlcA and making CS and DS indistinguishable. However, DS disaccharides could not be detected after digestion with chondroitinase B, specific for DS GAGs. Therefore, given the low amounts of DS expected within the CS + DS disaccharide mixture, this thesis will address ChABC-derived disaccharides as CS.

Disaccharides were then labeled with 2-aminobenzamide and 2-picoline-borane and analyzed by high performance liquid chromatography (HPLC) coupled to a fluorescence detector using a Dionex system (Dionex, Idstein, Germany). In the chromatograms, disaccharides were designated to peaks based on the correspondence with a mixture of standard disaccharides (Dextra, UK) as represented on Table 1. Percentage of GAGs disaccharides was calculated with OpenChrom software Community Edition 1.3.0. (Lablicate, Germany).

Table 1: Structure of 9 standard disaccharides used for HPLC analysis of ChABC digested murine brain samples.

Standard Disaccharides	
HA-0S	ΔHexA(β1-3)GlcNAc
CS-0S	ΔHexA(β1-3)GalNAc
CS-2S	ΔHexA2S(β1-3)GalNAc
CS-4S	ΔHexA(β1-3)GalNAc4S
CS-6S	ΔHexA(β1-3)GalNAc6S
CS-2S6S	ΔHexA2S(β1-3)GalNAc6S
CS-2S4S	ΔHexA2S(β1-3)GalNAc4S
CS-4S6S	ΔHexA(β1-3)GalNAc4S6S
CS-2S4S6S	ΔHexA2S(β1-3)GalNAc4S6S

Δ represents the unsaturation formed between carbons 4 and 5 of glucuronic (or iduronic) acid. Modified from Silva *et al.* [41].

2.5 Gene expression analyses

2.5.1 Genome-wide Microarray

In **Study III**, to comprehensively characterize neuroinflammation-induced changes in the brain matrix occurring during EAE, expression analysis of GAG-related genes was combined to chromatographic quantification of GAG disaccharides. GAGs structures depend on the balanced effect of structural and stereochemical modifications. Thus, the combination of catabolic, anabolic as well as GAG modifying enzymes including the sulfation catalyzed by sulfotransferases, N-acetylation by N-acetyltransferases, and stereoisomers produced by epimerases dictates the architecture of GAGs [27].

Agilent murine genome-wide microarray containing 59448 target IDs (Agilent Technologies, USA) as a screening tool for a broad analysis of inflammation and ECM-related genes was performed on cerebellar samples from EAE and CFA control mice ($n = 6$ per group). This allowed for a comprehensive analysis of core proteins, GAGs metabolic enzymes, GAGs degrading enzymes and T cell activation pathway genes and provided information of the influence of neuroinflammation induced by EAE on these processes. Sample RNA extraction, amplification, hybridization, and data normalization based on ranked mean quantiles [56] was conducted by OakLabs (Hennigsdorf, Germany). Analysis of the normalized data detected an outlier EAE sample that was excluded from further analyses. The remaining samples were used for identification of differentially expressed (DE) genes as described in the original publication [39].

2.5.2 Real time quantitative polymerase chain reaction (RT-qPCR)

RT-qPCR was employed for quantification of the expression of ECM-related genes. In **Study II**, to uncover sex and neuroinflammatory differences in expression of basement membrane (BM)-associated genes underlying tissue mechanics in areas of relevance, relevant glycoproteins, collagens (*Col4a1*, *Col1a1*), fibronectin (*Fn1*), and laminins (*Lama4*, *Lama5*), were selected [57, 58]. Expression of BM components was quantified in the cerebral cortex and the hippocampus were isolated from the brain of naïve and EAE mice of female and male mice.

In **Study III**, PCR reaction was used for validation of selected genes of interest obtained from a genome-wide microarray conducted on cerebellar samples at peak EAE and the corresponding CFA controls. This analysis was expanded to other brain areas (cerebellum, midbrain, and forebrain) and disease timepoints. Using the ascending

paralysis scoring system, brain samples were collected at pre-onset (prior to signs of disease, day 5 post-immunization), onset (first signs of disease), and remission (reduced signs of disease for at least 2 days after peak).

In both **Studies II** and **III** polymerase chain reaction was performed as described in Batzdorf *et al.* [40] and the data was analyzed using the $2^{-\Delta Ct}$ method described in [59]. The list of primers used is described in each publication [39, 40].

2.6 Histological investigations

2.6.1 Imaging Mass Cytometry

Eu-doped VSOP accumulation and its inflammatory surroundings in **Study I** were visualized by Imaging Mass Cytometry™ (IMC) to indistinguishably identify the particles within the inflamed tissue. IMC detection system is based on integrative spatial cytometry analysis of tissues through detection of time-of-flight of lanthanide metals tagged to specific antibodies using laser ablation [60]. Unlike iron detection methods that reveal both endogenous and exogenous iron, such as the Prussian blue, IMC makes possible to selectively visualize Eu-VSOP not based on its iron content but on the exogenous europium incorporated into the particles core. Combined with spatial distribution of brain resident and peripheral inflammatory cells, the IMC provides information on the VSOPs accumulation sites and hints of the pathological processes associated with the visualization of the particles by MRI. For tissue investigation with IMC, paraffin sections with 4 μm thickness of brain areas where Eu-VSOPs were detected by MRI were used. Tissue processing and antibody tagging following Fluidigm's instructions as well as image processing are detailed in the original publication [39].

2.6.2 Immunofluorescence

Studies II and **III** made use of immunofluorescent labeling of cells and ECM markers to depict their distribution within the brain tissue during neuroinflammation. In **Study II**, collagen type IV and fibronectin staining distribution within the cortical tissue was used to visualize ECM architecture in health and its remodeling during EAE disease. In **Study III**, abundancy, and distribution of Iba-1⁺ cells, as a marker of activated microglia, indicated the inflammatory state of cerebellar tissue at different EAE phases, whereas CS-56 antibody was employed to evaluate the distribution of CS GAGs within the tissue and to support the quantification data derived from HPLC. Staining protocol, antibodies and concentrations used are given in each publication [40, 41].

2.7 *In vivo* study design

2.7.1 **Study I:** *Contribution of Tissue Inflammation and Blood-Brain Barrier Disruption to Brain Softening in a Mouse Model of Multiple Sclerosis*

To investigate the pathological processes affecting the mechanical properties of the brain, a protocol was designed pairing MRE with Eu-VSOP distribution and GBCA enhancement using the adoptive transfer EAE model (Figure 2a). This model was selected due to its increased severity and degree of brain inflammation [36, 47], allowing for a comprehensive investigation of inflammatory changes affecting various brain regions. Encephalitogenic T cells obtained from donor mice ($n = 22$) as described above were adoptively transferred to healthy recipient mice ($n = 21$) after baseline imaging. The scanning protocol comprised an MRE sequence (single shot echo-planar imaging - EPI) as well as an anatomical T2-weighted image. As the disease progressed and the EAE disease was established, a second scan was acquired for MRE, T2-, T2*-weighted images as well as pre and postT1-weighted images. After the T1-pre, the animals were injected with a GBCA, Magnevist, at 0.2 mmol/kg (Bayer-Schering AG, Germany) via the tail vein and then scanned again for GBCA detection in a T1-weighted image. At the end of the scans, the mice were intravenously injected with 0.2 mmol/kg Eu-VSOPs (batch RH030812 Eu-R; $c[\text{Fe}] = 0.134 \text{ mol/L}$, provided by Experimental Radiology group, Department of Radiology, Charité-Universitätsmedizin Berlin, Germany). Twenty-four hours later, a post-Eu-VSOP T2*-weighted image was acquired for detection of particle distribution and the animals were sacrificed for tissue collection. It is important to note that the doses applied as well as the imaging interval for Eu-VSOP detection have been established in previous studies and shown to be adequate for the visualization of the contrast agents in pre-clinical MRI [35-37, 61].

2.7.2 **Study II:** *Sexual Dimorphism in Extracellular Matrix Composition and Viscoelasticity of the Healthy and Inflamed Mouse Brain*

In the **Study II**, intrinsic sex- and disease-related differences in brain viscoelasticity were investigated. *In vivo* MRE measurements were conducted in female ($n = 23$) and male ($n = 19$) mice during active EAE as well as in healthy control mice ($n = 14$ female, 14 male) (Figure 2b). The imaging protocol included an MRE image (EPI), and an anatomical T2-weighted image obtained at the expected peak phase of EAE. At the end of the scans, the animals were sacrificed, and the brain tissue was collected.

2.7.3 Study III: Brain inflammation induces alterations in glycosaminoglycan metabolism and subsequent changes in CS-4S and hyaluronic acid

Investigation of disease activity-related modification of brain GAG disaccharides and screening of GAGs metabolic pathways was carried out in female EAE mice ($n = 24$) and age-matched CFA controls ($n = 24$) (Figure 2c). Sham-immunized mice (CFA) receive only an injection of phosphate-buffered saline emulsified in adjuvants. Brain tissue collected at different timepoints corresponding (pre-onset, onset, peak, and remission) based on individual disability score was used to investigate neuroinflammation-associated gene expression of GAG metabolic enzymes and the sulfation pattern of CS and HA GAGs.

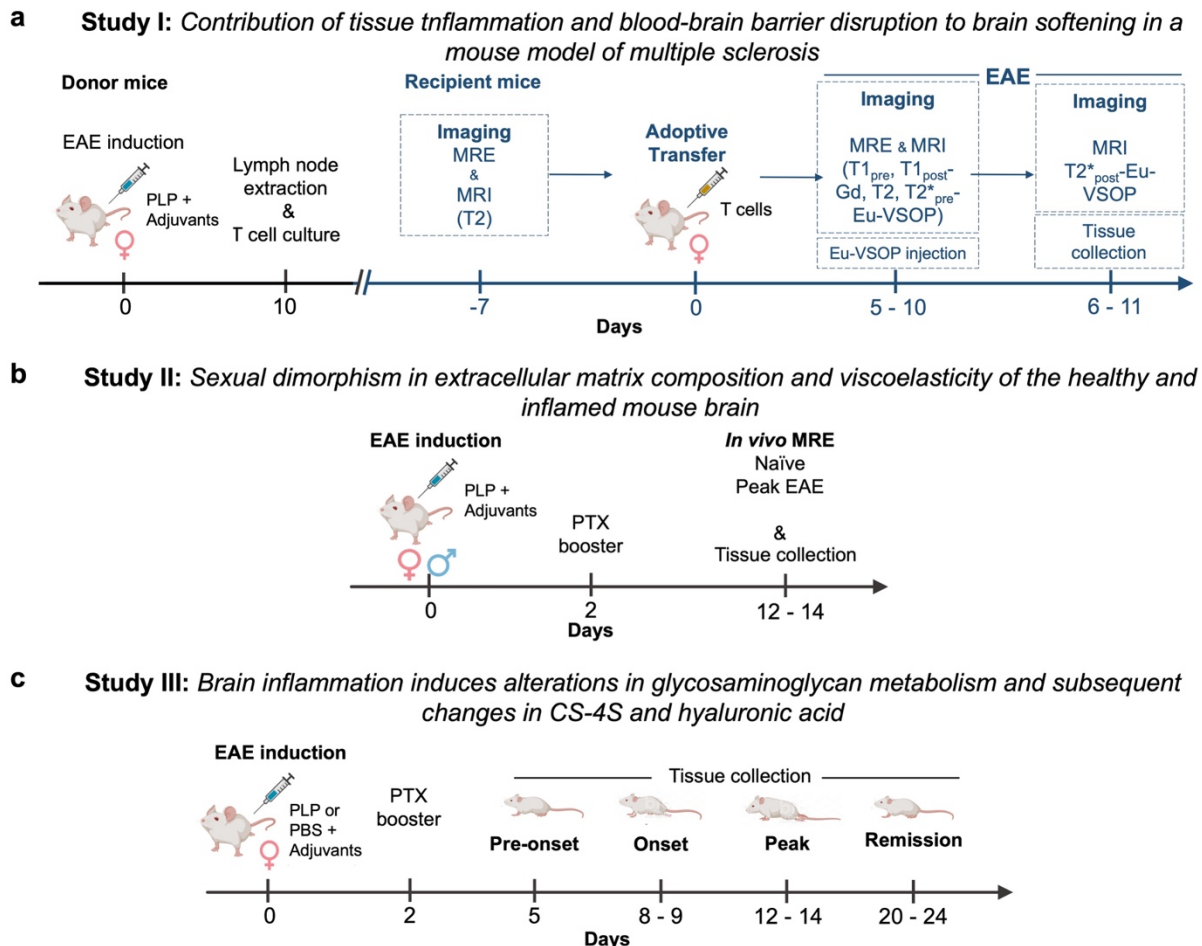


Figure 2: Experimental design of *in vivo* studies. (a) Design of **Study I**. A group of recipient EAE mice were scanned prior to receiving encephalitogenic T cells produced by donor mice actively immunized with the myelin proteolipid (PLP) and adjuvants. After passive EAE induction, MRE and pre-contrast images were acquired, as well as post-T1-weighted image following GBCA administration. Intravenous injection of Eu-VSOPs took place after the scans and particles were visualized 24h later with a T2*-weighted image. (b) Schematic of MRE acquisition in **Study II**. Female and male SJL mice were scanned at peak EAE after active immunization with PLP for investigation of cerebral viscoelastic alterations and basement membrane (BM) remodeling. (c) Illustration of the progression of EAE after induction in **Study III**. For investigation of neuroinflammatory-induced alterations in GAG structure and metabolism in female mice during the course of EAE, tissue was at different timepoints (pre-onset, onset, peak, remission) sampled from a cohort of

mice immunized with PLP or received only phosphate-buffered saline (PBS) and adjuvants (CFA controls). (own representation: Rafaela Vieira da Silva, Created with BioRender.com).

2.8 Statistical assessment and reproducibility

Statistical analysis of the data presented in the studies was conducted with the software GraphPad Prism 9 (GraphPad software, USA). Normality was tested for data groups using the D'Agostino & Pearson or Shapiro-Wilk test [62], and the appropriate parametric or non-parametric statistical test was applied accordingly. Statistical significance was considered for $p < 0.05$. Data is graphically represented by mean \pm standard deviation or mean \pm min and max (**Studies I & III**) and mean \pm 95% confidence interval CI (**Study II**). Statistical text, significance and sample size are described in the corresponding figure legends.

3 Results

3.1 MRE reveals neuroinflammatory processes beyond BBB-disruption associated with Eu-VSOPs accumulation and tissue remodeling

In **Study I** [39], by pairing MRE with Eu-VSOP and GBCA-enhanced MRI of the mouse brain, we set out to investigate the pathological alterations behind cerebral tissue softening during neuroinflammation using the adoptive transfer EAE model. All EAE mice displayed signs of established disease with an average score of 1.97 ± 0.76 on the first day of scan and 2.83 ± 0.39 on the second day and showed Eu-VSOP accumulation and GBCA enhancement. Incidence maps of Eu-VSOP accumulation and GBCA enhancement depicted the differences in the pattern of contrast imaging, with the particles focally distributed in small areas while GBCA enhancement comprised large diffuse areas (see Figure 3 and Table 1 in Silva *et al.* [39]). To determine the contribution of BBB disruption (visualized by GBCA-enhancement on T1-weighted images) and the inflammatory processes behind VSOP accumulation (visualized on T2*-weighted images) to the biomechanical properties of the brain tissue, masks of areas evidenced by a single contrast agent individually, i.e. without overlapping, were generated. The MRE parameters stiffness, deduced from the shear wave speed or c , and fluidity, derived from the loss angle (φ), were then investigated in these areas.

Confirming previous studies, the whole brain was softer after EAE establishment. Only changes in brain tissue stiffness were detectable by multifrequency MRE (baseline 3.15 ± 0.11 m/s vs. EAE 2.89 ± 0.20 m/s, $p < 0.0001$), as tissue fluidity remained unaltered (baseline 0.69 ± 0.03 m/s vs. EAE 0.70 ± 0.06 m/s, $p = 0.61$). Areas comprising GBCA- or Eu-VSOP masks also revealed brain tissue softening during EAE compared to baseline measurements, prior to disease induction, (GBCA baseline 3.28 ± 0.38 m/s vs. GBCA EAE 2.99 ± 0.51 m/s, $p = 0.0183$; Eu-VSOP baseline 3.03 ± 0.39 m/s vs. Eu-VSOP EAE 2.55 ± 0.47 m/s, $p = 0.0235$) (Figure 3a).

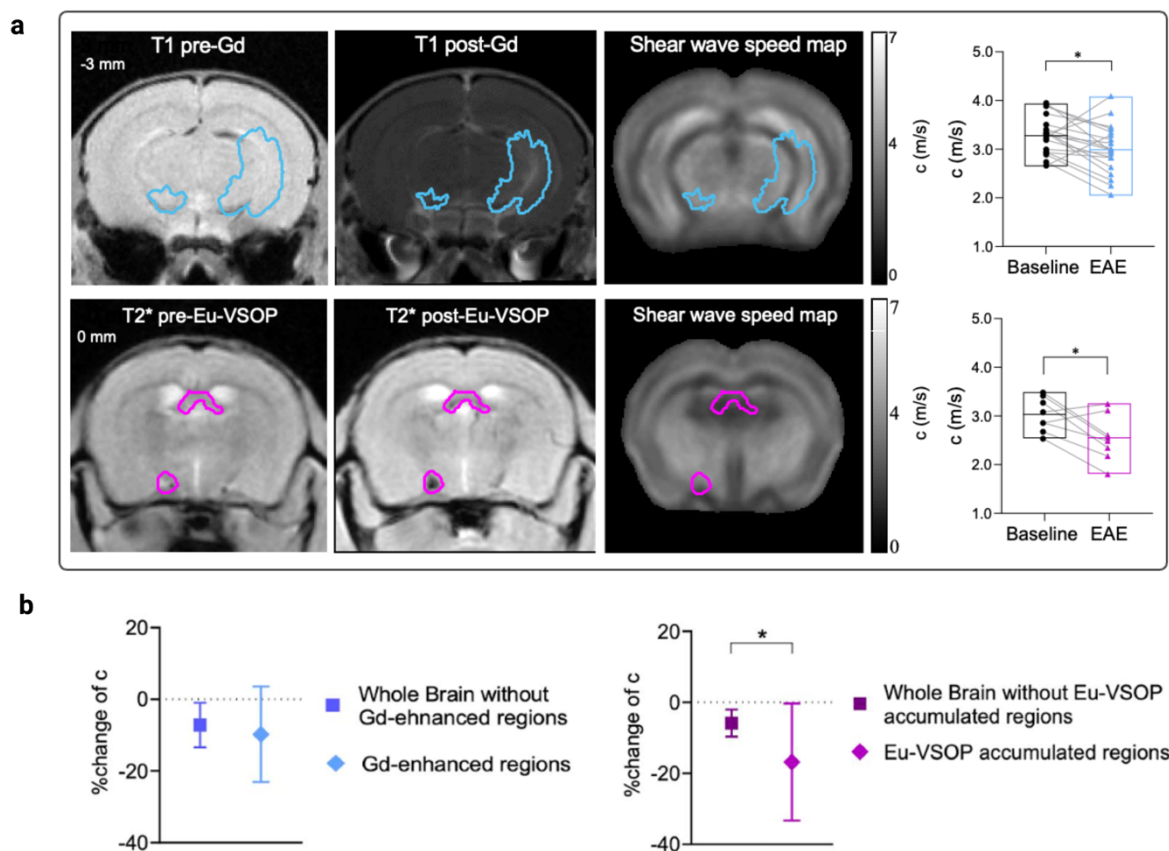


Figure 3: Stiffness changes in areas of contrast agent visualization during EAE. (a) Upper panel shows representative T1-weighted images of the mouse brain before (top left) and after (top center) GBCA administration depicting the area covered by Gd-enhancement during EAE. The respective stiffness map given by the shear wave speed (top right) and a plot with the averaged stiffness measurements in areas of Gd-enhancement at baseline and EAE are also shown; $n = 19$; mean, min/max; $*p < 0.05$. In the lower panel, representative T2*-weighted images before (bottom left) and after (bottom center) Eu-VSOP administration show the areas of particle accumulation during EAE. Additionally, the respective stiffness map (bottom right) and averaged stiffness values in areas of Eu-VSOP at baseline and EAE are provided; $n = 8$, mean, min/max; $*p < 0.05$. (b) Comparison between percentage stiffness change in areas visualized by GBCA (left) or Eu-VSOP (right) and the respective non-enhancing areas. Mean \pm SD, paired t-test, $n_{\text{Gd}} = 19$, $n_{\text{Eu-VSOP}} = 8$, $*p < 0.05$. (modified from Silva et al. [39]).

To determine whether MRE could distinguish reduction in tissue stiffness within the pathological processes behind the areas delimited by the contrast agents or a global

effect, we compared the percent effect in areas with and without contrast agents. Surprisingly, GBCA-enhanced compared to non-enhance areas were similarly affected (GBCA-enhanced areas $-9.76 \pm 13.32\%$ vs. non-enhanced areas $-7.18 \pm 6.21\%$, $p = 0.3321$), while areas circumscribed by Eu-VSOP hypointensity were significantly softer than the rest of the brain (areas with Eu-VSOP accumulation $-16.81 \pm 16.49\%$ vs. areas without accumulation $-5.85 \pm 3.81\%$, $p = 0.0483$) (Figure 3b).

Since the effect on areas delimited by Eu-VSOP accumulation was more pronounced than in areas of GBCA-enhancement, we examined the environment surrounding particle accumulation visualized by MRI within the brain tissue using IMC. Upon inflammation, infiltration of leukocytes, intense astrogliosis as well as microgliosis were observed in the tissue of EAE mice compared with healthy control (Figure 4a). Analysis of areas where Eu-VSOP were detected by MRI emphasized particle accumulation surrounding the ventricles and in the perivascular space (Figure 4b-c). In the perivascular space, Eu-VSOPs co-localized with infiltrating leukocytes (CD45⁺ cells, cyan), activated microglia (Iba1⁺ cells, white) and endothelial cells (CD31, yellow), (Figure 4b). A similar pattern of co-localization with inflammatory cells was observed in the periventricular space in association with particles distributed in the choroid plexus, (Figure 4c). We did not detect particles inside NeuN⁺ neurons (magenta).

In summary, our data obtained by comparing Eu-VSOP imaging and GBCA-enhancement with stiffness changes calculated by multifrequency MRE shows that stiffness is more affected by the focal inflammation and tissue remodeling identified by particle accumulation, than by diffuse inflammation and BBB disruption detected with GBCA.

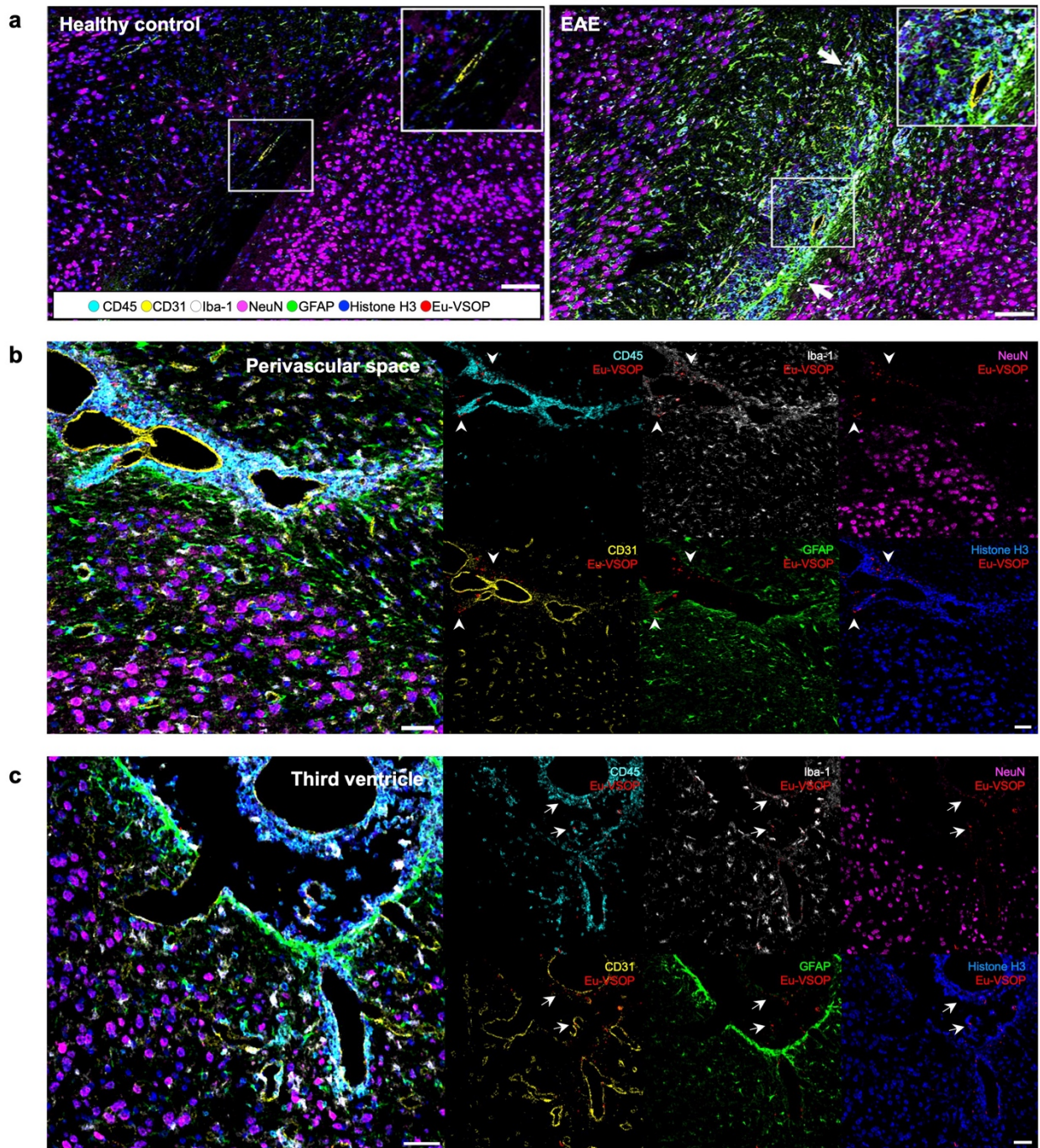


Figure 4: Histological visualization of Eu-VSOPs and the surrounding inflammatory environment by IMC during EAE. (a) Healthy brain section imaged by IMC shows a vessel (CD31, yellow) with surrounding astrocyte (GFAP, green) and neuronal cells bodies (NeuN, magenta) located the brain stem and hippocampal formation (left). In EAE, a similar region (right) presents intense leukocyte infiltration (CD45, cyan), as well as astrogliosis and microgliosis (Iba1, white). Scalebar: 100 μ m. Environment of Eu-VSOP accumulation visualized by MRI in perivascular cuffs (b, white arrowheads), inflamed choroid plexus and periventricular area (c, white arrows) depicts co-localization of particles (Eu-VSOP, red) with infiltrating leukocytes and endothelial cells (yellow). Scalebar: 50 μ m. (modified from Silva et al. [39]).

3.2 Basement membrane matrix composition contributes to regional alterations in brain stiffness

In the work of Batzdorf *et al.* [40], which I supervised as senior co-author, disease-associated regional tissue viscoelasticity as well as associated changes in ECM components of the BM were assessed in a sex-dependent manner (Figure 5a). While intrinsic and disease-associated sex-differences are explored in depth in the paper and are the main subject of Clara Batzdorf's MD PhD Thesis, here a special focus will be given here to neuroinflammation-induced changes in females.

Intrinsic differences of tissue stiffness between females and males were detected only in the cortical tissue (see Figure 2 in Batzdorf *et al.* [40]). However, during EAE, both male and female mice presented reduced cortical stiffness. In females, the cortex, but not other brain areas, was softer in EAE mice compared to naïve mice (female naïve = 2.90 ± 0.33 m/s, female EAE = 2.70 ± 0.16 m/s, $p = 0.013$) (Figure 5b). Assessment of BM components indicated differential expression associated with EAE. The analyzed genes coded for the glycoproteins laminin $\alpha 4$ (*Lama4*), laminin $\alpha 5$ (*Lama5*), collagen type I (*Col1a1*), collagen type IV (*Col4a1*) and fibronectin (*Fn1*). Cortical expression of *Lama4* (female: 3.1-fold, $p < 0.001$), *Lama5* (female: 2.9-fold, $p < 0.01$) and *Col4a1* (female: 3.0-fold, $p < 0.001$) was increased in female EAE mice compared with healthy controls (Figure 5c). However, *Col1a1* and *Fn1* were not significantly different when comparing naïve and EAE females (-1.3-fold and 1.1-fold, all $p > 0.05$, respectively) (Figure 5c). Cortical distribution of collagen type IV and fibronectin, in vessel-like shape, confirmed the increase of these proteins in the BM, (see Figure 6 in Batzdorf *et al.* [40]). Interestingly, these changes took place in the absence of leukocyte infiltration assessed with HE.

Ultimately, these results demonstrate that brain stiffness can be sex-dependent but is above all regionally defined, with a prominent softening of the cortical tissue during EAE. The analysis of (glyco)proteins constituting the BM indicates remodeling of the brain matrix with an upregulation of *Lama4*, *Lama5* and *Col4a1* in females in response to neuroinflammation.

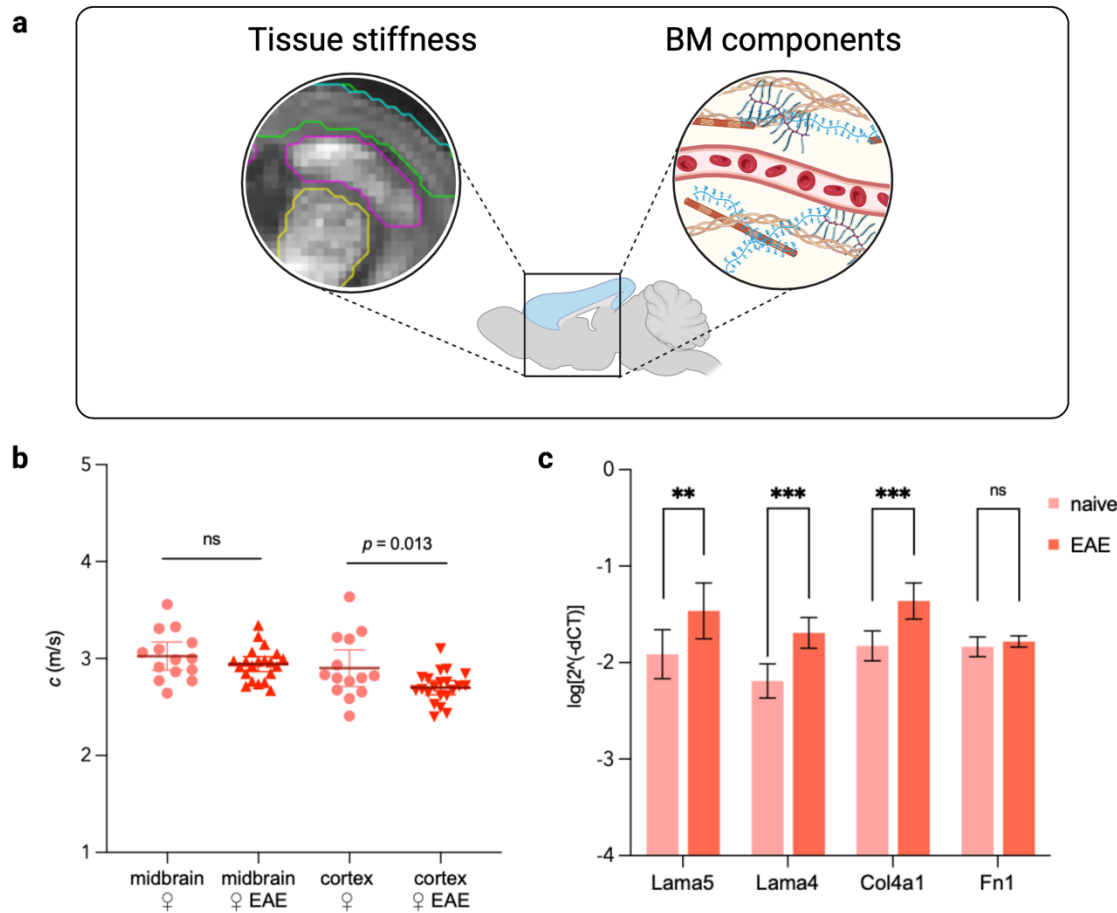


Figure 5: Analysis of cortical stiffness changes associated with BM remodeling. (a) Illustration of the segmentation of stiffness maps measured by multifrequency MRE, applied to determine cortical (green outline on left panel) changes of stiffness. Gene expression analysis to determine the expression levels of BM (glyco)proteins in the cortex (blue mask) was performed in the same region. (b) Stiffness given by shear wave speed (c in m/s) in the whole midbrain section and cortex of naïve (circle) and EAE mice at peak (triangle). Mean \pm 95%CI; n naïve = 14, n EAE = 21. (c) Cortical expression of BM-associated genes in naïve and EAE mice. Mean \pm 95% CI. n female naïve = 6, n male naïve = 6, n female EAE = 6, n male EAE = 7, ** p <0.01, *** p <0.001. (modified from Batzdorf *et al.* [40], Created with BioRender.com).

3.3 Genetic signature of CS degradation followed by altered sulfation profile denote matrix involvement in EAE disease development and progression

In **Study III**, changes in GAGs disaccharides and the expression levels of the enzymatic machinery regulating GAG homeostasis were investigated in the different phases of EAE. To determine the involvement of GAG metabolism during inflammation in the brain, we performed a genome-wide microarray with cerebellum, a region known to be highly affected in EAE [63]. Samples were collected at the expected peak phase of EAE (mean score = 1.83 ± 1.033). Analysis of the expression of genes encoding GAGs anabolic and catabolic enzymes as well as for PGs core proteins was carried out. Sixteen genes

involved in GAG degradation were identified as upregulated genes, including heparanase (*Hpse*), α -iduronidase (*Idua*), hexosaminidase α (*Hexa*) and β (*Hexb*), and β -glucuronidase (*Gusb*), hyaluronic acid synthase 2 (*Has2*) and decorin (*Dcn*). Meanwhile the expression of the core protein genes syndecan 2 (*Sdn2*), glypican 1 (*Gpc1*), glypican 5 (*Gpc5*), brevican (*Bcan*), and chondroitin sulfate PG 5 (*Cspg5*) as well as of chondroitin 4-O-sulfotransferase 2 (*Chst12*), glucuronic acid epimerase (*Glce*), and DS epimerase (*Dse*) were downregulated (Figure 2 in Silva *et al.* [41]).

From these differentially expressed genes found in the microarray data, expression of selected genes was then quantified by RT-qPCR in other brain regions and disease phases. The function of the enzymes encoded by the genes selected are described in Figure 6a. Compared to the fore- and midbrain, transcriptional changes were prominently found in the cerebellum. In the cerebellar tissue, upregulation of *Hpse* (13.0-fold, $p = 0.012$), *Has2* (3.7-fold, $p = 0.004$), *Hexb* (3.0-fold, $p < 0.0001$), *Gusb* (3.2-fold, $p = 0.0008$), *Dcn* (2.1-fold, $p = 0.032$), *Dse* (1.8 fold, $p = 0.0008$) in EAE were confirmed, while downregulation of *Chst12* was not significant (-2.0-fold, $p = 0.41$) (Figure 6b and Figure 3a in Silva *et al.* [41]). In the midbrain, the genes involved in GAG degradation were significantly elevated *Hpse* (4.9-fold, $p = 0.004$), *Hexb* (2.6-fold, $p = 0.016$), *Gusb* (2.5-fold, $p = 0.019$), and *Has2* (2.2-fold, $p = 0.028$) and no effect on *Chst12* (1.3-fold, $p = 0.41$) and *Dse* (1.5-fold, $p = 0.027$) was encountered. No expression differences were found in the forebrain. Thus, the cerebellar tissue was chosen for a comprehensive temporal analysis of the transcriptional changes in GAG metabolism.

Based on the EAE score of the disability, brain tissue was collected at different stages of inflammation (mean score: onset = 0.58 ± 0.204 , peak = 1.75 ± 1.037 , remission = 0.71 ± 0.534). The degree of tissue inflammation in each EAE phase, confirming disease severity, is represented by increased number of activated microglia and monocytes (*Iba1*⁺ cells), knowingly upregulated in MS and EAE [64], as shown in Figure S5 in Silva *et al.* [41]. Control mice did not display any signs of disability neither upregulation of *Iba1*. Transcriptional analysis of the targeted genes identified an early upregulation of *Has2* (1.7-fold, $p = 0.006$), *Hexb* (1.4-fold, $p = 0.024$), *Dse* (1.3-fold, $p = 0.006$) and *Gusb* (1.5-fold, $p = 0.009$) 5 days post-immunization (pre-onset) in EAE mice compared to CFA controls (Figure 6c). Upon manifestation of disease signs, the overexpression of these genes increased to 13.7-fold for *Hpse* ($p = 0.009$), 2.6-fold for *Hexb* ($p = 0.023$) and 3.4-fold for *Gusb* ($p = 0.016$) at onset and to 13.0-fold for *Hpse* ($p = 0.012$), 3.0-fold, for *Hexb*

($p < 0.0001$) and 3.2-fold for *Gusb* ($p = 0.0008$) during peak, with a reduction during remission (*Hpse* 4.3-fold, *Hexb* 2.0-fold, and *Gusb* 1.6-fold, all $p < 0.01$). *Dse* remained steadily overexpressed at all phases (1.3-fold at pre-onset, $p = 0.006$; 1.7-fold at onset, $p = 0.006$; 1.8-fold at peak, $p = 0.0008$; and 1.4-fold at remission, $p = 0.002$) while *Has2* reached the highest fold change from control in the peak phase (1.7-fold at pre-onset, $p = 0.006$; 5.4-fold at onset, $p = 0.099$; 3.7-fold at peak, $p = 0.004$; and 2.0-fold at remission, $p = 0.004$), and *Dcn* expression was highly induced at onset phase decreasing towards remission (3.5-fold at onset, $p = 0.003$; 2.1-fold at peak, $p = 0.032$; and 1.7-fold at remission, $p = 0.008$) (Figure 6c).

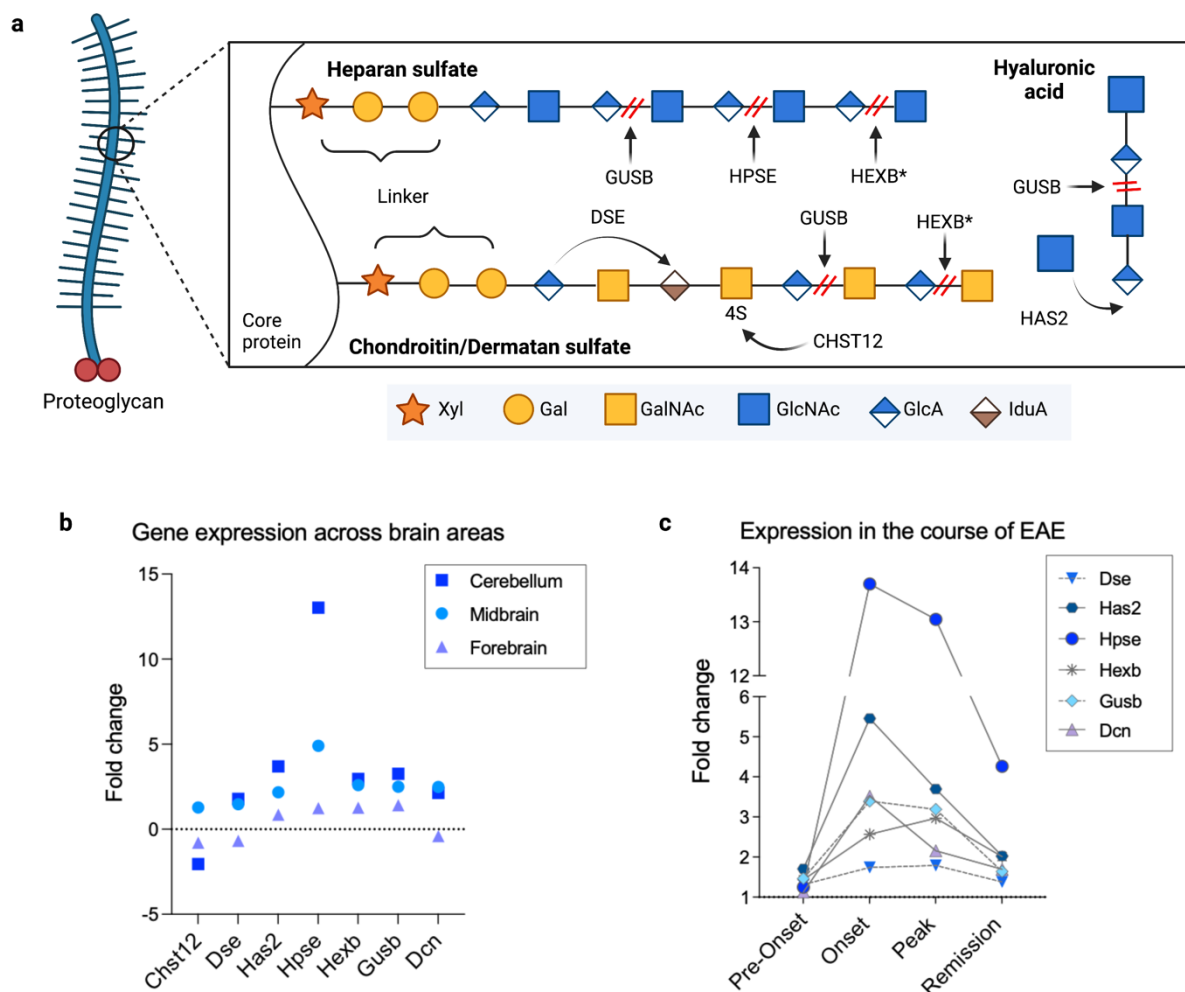


Figure 6: Transcriptional analysis of GAG-associated genes in the course of EAE. (a) Representation of targets involved in GAGs metabolism selected from the microarray screening include the GAG-degrading enzymes β -glucuronidase (GUSB), hexosaminidase β (HEXB), and the secreted heparanase (HPSE). While GUSB and HEXB cleaves all GAG families, HPSE specifically acts on HS chains. Synthetic enzymes include hyaluronic acid synthase 2 (HAS2), chondroitin 4-O-sulfotransferase 2 (CHST12), that adds a sulfate to carbon 4, and the dermatan sulfate epimerase (DSE), responsible for the conversion of glucuronic acid into iduronic acid. (b) Fold change from CFA control of target genes across different brain segments at peak EAE. n cerebellum = 6 CFA, 4 EAE; n midbrain = 6 CFA, 5 EAE; n forebrain = 5 CFA. Statistics were applied to $2^{-\Delta\Delta CT}$ values and can be found in Figure 3a-c in Silva et al. [41]. (c) Analysis of cerebellar expression of GAG-related genes given by fold change from control at pre-onset, onset, peak and remission

phases of EAE. *n* pre-onset = 5 CFA, 4 EAE; *n* onset = 4 CFA, 6 EAE; *n* peak = 6 CFA, 4 EAE; *n* remission = 4 CFA, 6 EAE. Statistics were applied to $2^{-\Delta\text{CT}}$ values which can be found in Figure 3a-d in Silva *et al.* [41]. Xyl – D-xylose, Gal – galactose, GlcA – D-glucuronic acid, IduA – L-iduronic acid, GalNAc – N-acetyl-D-galactosamine, GlcNAc – N-acetyl-D-glucosamine. (modified from Silva *et al.* [41], Created with BioRender.com).

Considering the significant changes in transcripts involved in GAGs metabolism, we investigated structural alterations in GAGs disaccharides profile quantified by HPLC. Brain samples divided into forebrain, midbrain and cerebellum were digested with ChABC, as the main GAG types present in the brain were expected to be CS and HA (Figure 7a). The resulting chromatogram with 8 disaccharide peaks identified non-sulfated (HA-0S, CS-0S), monosulfated (CS-2S, CS-4S, CS-6S) and disulfated (CS-2S6S, CS-2S4S, CS-4S6S) disaccharides subunits (Figure 7b). No trisulfated disaccharide was detectable. Integration of the peak areas and calculation of a relative percentage revealed HA-0S as the major GAG disaccharide fraction in the cerebellum representing 41% and around 25% in the forebrain and midbrain of control mice (see Figure 5 in Silva *et al.* [41]). CS-4S was the most abundant among the CS fractions, amounting from 85 to 89% across all brain regions. Monosulfated GAG disaccharides represented less than 8% each and disulfated GAG disaccharides, less than 2% (see Supplementary Figure 6 in Silva *et al.* [41]).

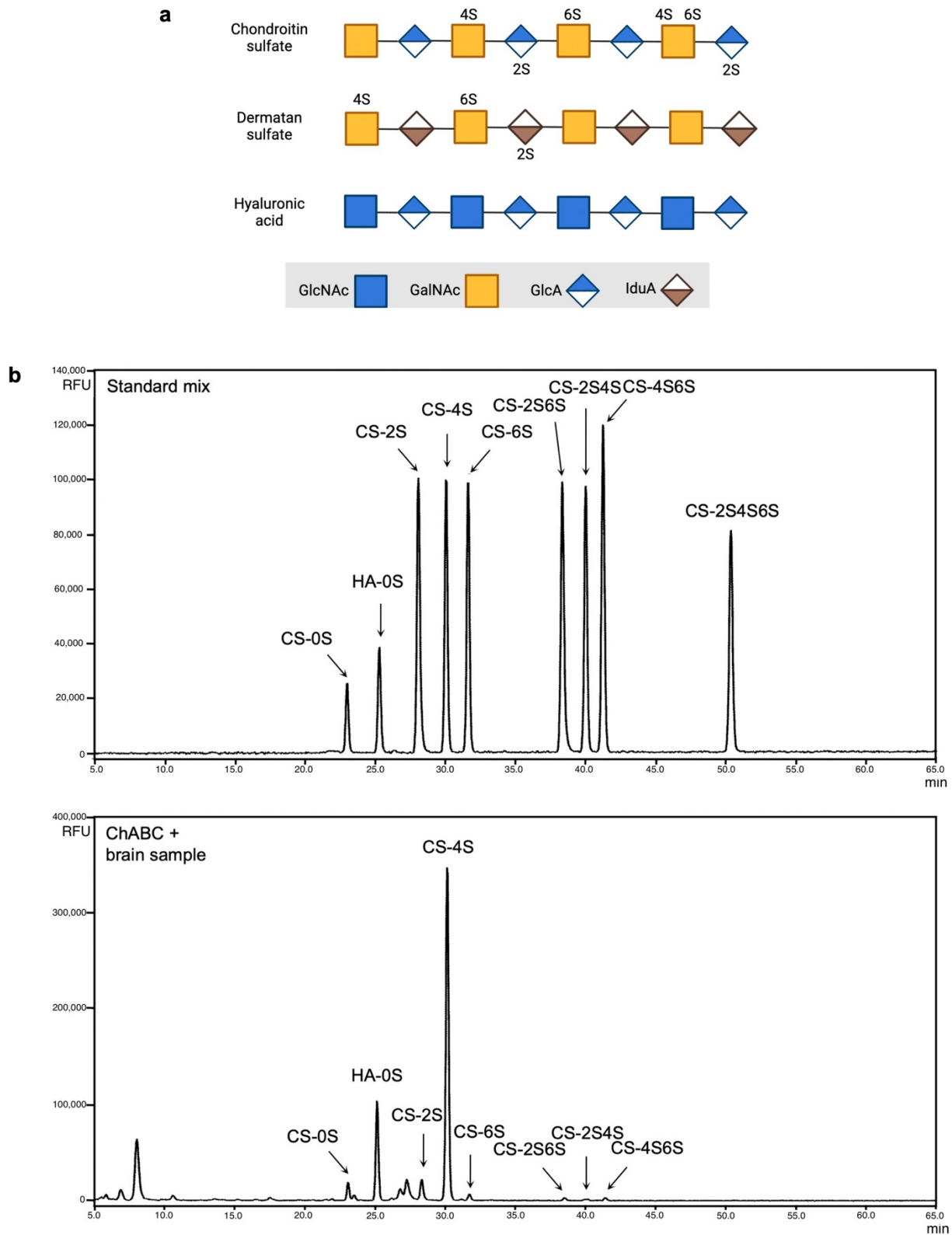


Figure 7: GAG disaccharides detection by HPLC. (a) Illustration of CS, DS and HA GAG chains prior to digestion with ChABC. CS and DS GAG chains, formed by GalNAc and a uronic acid (GlcA or IduA), present different degrees of sulfation at the positions 2 (2S) of the uronic acid and 4 (4S) or 6 (6S) of GalNAc, while HA GAG subunits are solely composed of GlcNAc and GlcA. (b) Representative

chromatograms of 2-AB labeled disaccharides detected by HPLC using a standard mix of disaccharides (top) and brain tissue (200 µg of total protein, bottom) digested with 50 mU ChABC. Eight peaks found in the brain were assigned to CS-0S, HA,CS-2S, CS-4S, CS-6S, CS-2S6S, CS-2S4S, CS-4S6S, and CS-2S4S6S. After ChABC cleavage of CS and DS GAGs, the isomers GlcA and IduA can no longer be distinguished and disaccharides are represented as CS may contain originally DS subunits. GlcA – D-glucuronic acid, IduA – L-iduronic acid, GalNAc – N-acetyl-D-galactosamine, GlcNAc – N-acetyl-D-glucosamine. (modified from Silva *et al.* [41], Created with BioRender.com).

From the three brain segments analyzed, only the cerebellum showed significant changes in CS and HA GAGs profile. Interestingly, in agreement with the overexpression of *Has2* in the course of the disease, an increase in HA-0S was found in the cerebellum of EAE mice compared to control mean (CFA = 41.15% ± 1.634; EAE = 51.89% ± 2.758, $p = 0.016$). A 3.68% reduction in CS-4S (CFA = 85.67% ± 1.328; EAE = 82.63% ± 2.204, $p = 0.047$) was also found in the cerebellum while a 2.02% decrease occurred in the midbrain (CFA = 88.77% ± 1.153; EAE = 86.97% ± 1.033, $p = 0.065$). When GAGs disaccharides were quantified during disease progression, elevation of HA-0S observed at peak EAE persisted in the remission phase (CFA = 43.26.% ± 1.171, EAE = 50.86% ± 2.219, $p = 0.029$), but was not changed at onset (Figure 8a). Contrarily, CS-4S was significantly decreased at peak and remained unchanged during onset and remission (Figure 8b). Additionally, quantification of GAG disaccharides using a standard curve, showed a total reduction of disaccharides in EAE compared with CFA and confirmed the previously described increase in HA-0S (CFA = 328.9 pg/ng ± 81.96, EAE = 430.0 pg/ng ± 16.49, $p = 0.016$) and reduction of CS-4S (CFA = 564.2 pg/ng ± 82.06, EAE = 450.9 pg/ng ± 11.59, $p = 0.012$) (Figure 8c). Despite the increased expression of *Dse* and *Hpse* would indicate the presence of DS and HS GAGs, both types of disaccharides were undetectable in the brain samples after digestion with ChB and heparanases I, I and II, respectively.

Altogether, these findings show that neuroinflammation induced major ECM-related transcriptional changes in the cerebellum and that these changes manifested in early disease stages. Genes related to GAGs degradation and HA synthesis, *Hexb* and *Has2*, respectively, were upregulated before animals exhibited signs of disease or even before structural changes in GAG disaccharides could be quantified. These changes preceded structural alterations in GAG sulfation profile, revealed by an increase in HA and decrease in CS-4S. Overall, gene expression and GAG composition are associated with the disease progression and the major changes are found during inflammatory phases.

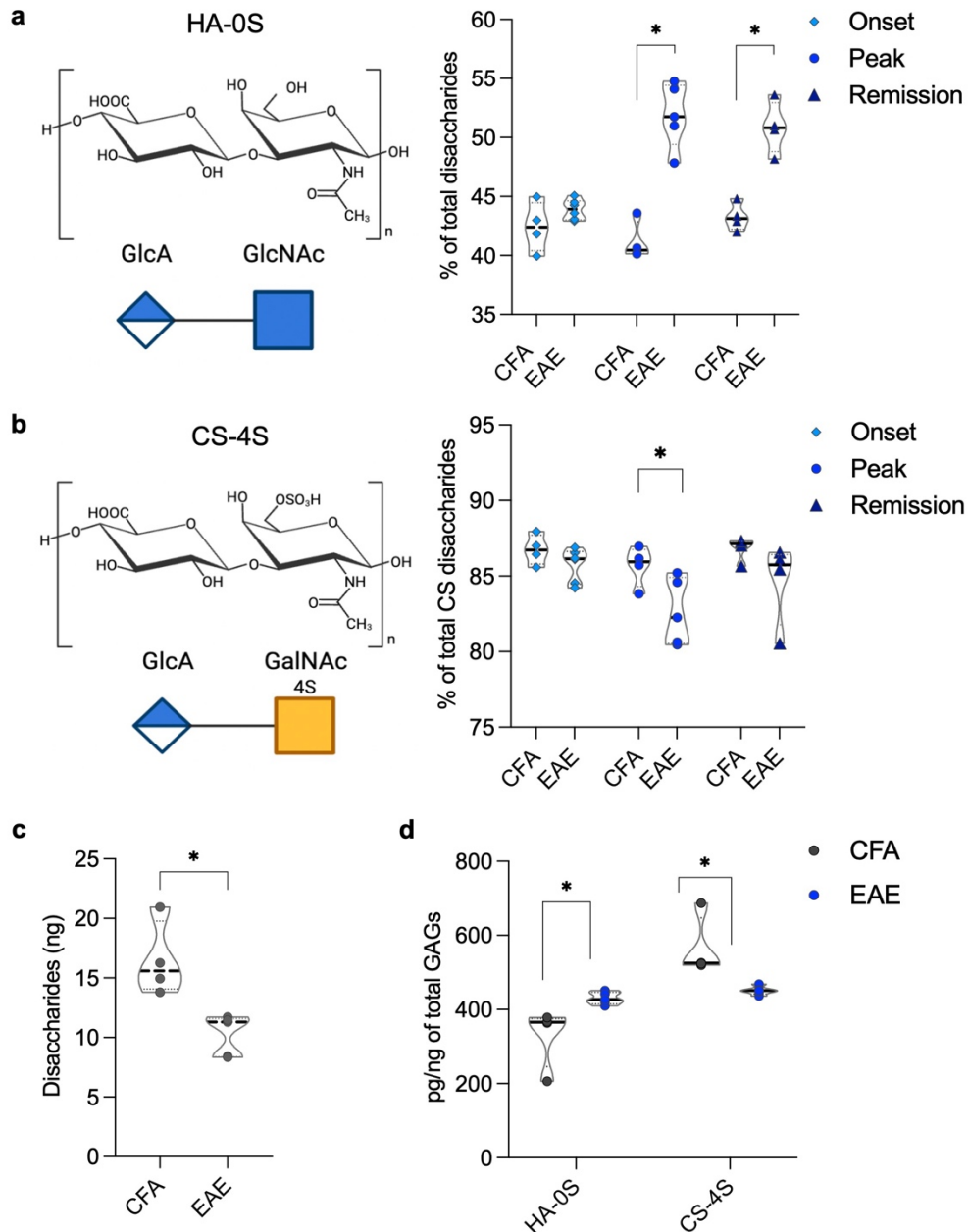


Figure 8: Quantification of the main GAG disaccharide fractions obtained from ChABC digestion of cerebellar samples in the course of EAE. (a) HA-0S disaccharide structure and relative percentage from total GAG disaccharides at onset (diamond), peak (circle) and remission (triangle) phases of EAE compared with matching CFA controls. (b) CS-4S structure and relative percentage within the total CS disaccharide fractions at different phases of EAE. n onset = 4 CFA, 6 EAE; n peak = 4 CFA, 5 EAE; n remission = 4 CFA, 4 EAE; $*p < 0.05$ (c) Standard curve-based quantification of total disaccharides in CFA and EAE cerebellar samples at peak. (d) HA-0S and CS-4S fractions in pg/ng of total GAG disaccharides at peak EAE compared with CFA controls. $n = 4$ CFA, 5 EAE, $*p < 0.05$. (modified from Silva et al. [41], Created with BioRender.com).

4 Discussion

The studies presented in this thesis investigated EAE-induced alterations in the brain ECM and viscoelastic properties as markers of disease activity and development (Figure 9). The results identified matrix alterations in the course of EAE and demonstrated the

influence of neuroinflammatory processes on mechanical properties of the brain, suggesting that ECM remodeling and tissue softening can be used for *in vivo* detection of disease development. By combining experimental MRI-based tools (Eu-VSOP-based imaging and MRE) with classical GBCA enhancement, the contribution of focal and disseminated inflammation to tissue stiffness was assessed. As shown in **Study I**, tissue remodeling characterized by intense focal inflammation induced a greater effect on brain stiffness than BBB disruption or disseminated inflammation. Besides disseminated inflammation in the brain, the findings of **Study II** revealed that regional tissue mechanical properties can also be mapped and quantified by MRE. The cortex, most affected region, was on average 7% softer during neuroinflammation in female EAE mice. Additionally, matrix remodeling in the course of EAE was investigated. While **Study II** indicated alterations in glycoproteins of the BM, **Study III** indicated an association between development and progression of neuroinflammation and transcriptional and structural changes of GAGs. Early upregulation of gene related to GAGs metabolism were followed by an increase in HA-0S and decrease in CS-4S disaccharides.

Effect of inflammation on brain structure and ECM

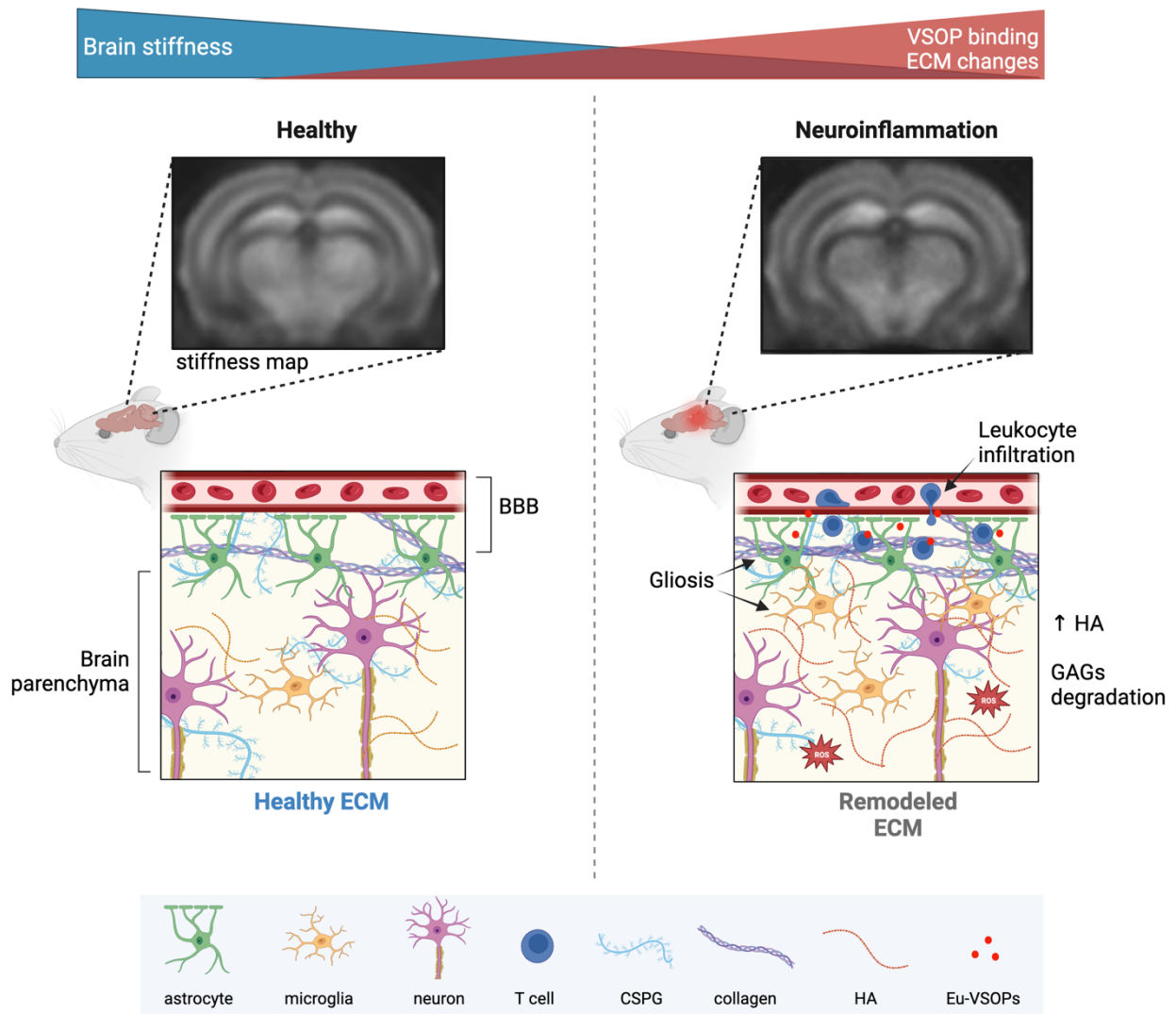


Figure 9: Neuroinflammation-induced remodeling of brain tissue structure and ECM. In physiological states, the homeostatic balance of ECM components and cellular composition of the brain tissue determines tissue integrity. Upon inflammation, tissue integrity is altered as both the cellular and ECM composition of the brain changes. Leukocytes migrate into the brain via a disrupted BBB and accumulate in the perivascular cuffs, leading to alterations of the BM composition. Among these alterations, an increased expression of BM components, such as collagen and laminin and gliosis seem to remodel the perivascular environment, leading to uptake of Eu-VSOPs. In the brain parenchyma, inflammation-mediated degradation of GAGs significantly impacting CS-4S disaccharides is accompanied by an elevation in HA, influencing tissue integrity. Thus, both local cellular environment and ECM remodeling affect the mechanical properties of the tissue visualized in stiffness maps measured by MRE. Local and disseminated softening can be used to determine the degree of brain inflammation. (own representation: Rafaela Vieira da Silva, Created with BioRender.com).

4.1 *In vivo* MRE to assess EAE pathophysiology

MRE has been previously applied for the investigation of the mechanical properties of the brain during neurological conditions in both humans [12-14, 65] and animal models [16, 17, 61]. All reports pointed to tissue softening during neuroinflammation. Similarly, our

results corroborated the previous findings on the global reduction of viscoelasticity [16-18] in addition to further resolve local stiffness changes in areas of Eu-VSOP accumulation or GBCA enhancement. While technical limitations only allowed for analysis of a single brain slice in earlier mouse studies [16, 17, 61], here we applied the recently developed MRE with tomoelastography post-processing [53, 66, 67] to examine tissue mechanics across multiple slices. With this progress, in **Study I**, we were able to show that the stiffness in areas of GBCA enhancement, associated with BBB leakage, was reduced in EAE compared to baseline visualized by GBCA, but it did not differ from areas without enhancement.

Compared to Eu-VSOPs, the pattern of GBCA distribution during EAE displayed larger and more diffuse areas of contrast enhancement, likely reflecting disseminated inflammation. GBCAs are clinically used as the standard marker of BBB leakage on T1-weighted images, decreasing the T1 relaxation time, which have been observed to predict formation of demyelinating lesions in MS and becoming a marker of inflammatory activity [3, 68]. However, parenchymal dissemination of GBCA is dependent of factors other than BBB disruption, such as GBCAs' tissue distribution and diffusion. The specific GBCA molecule biodistribution [69], the extent of vascular permeability [70] and the reduction of extracellular space caused by inflammation [71] may play a role in GBCA distribution. Thus, stiffness changes in areas of GBCA enhancement may indicate disseminated inflammatory events rather than focal neuropathological processes.

On the contrary, tissue stiffness in areas of Eu-VSOP accumulation was reduced during EAE and appeared significantly lower compared to areas without particle accumulation. In the incidence maps, we observed focal accumulation of Eu-VSOPs concentrated in proximity to the ventricles and major vessels using T2*-weighted images (see Figure 3 and Supplementary Figure 3, in Silva *et al.* [39]). Histological assessment of the microenvironment of particle accumulation using IMC revealed that Eu-VSOP were associated with infiltrating leukocytes, activated microglia and the endothelium.

Previously, VSOPs were also shown to accumulate in areas of immune cell infiltration [35, 38, 72]. At peak EAE, Eu-VSOPs accumulation, visualized by its strong susceptibility effect on T2*-weighted images, mostly coincided with GBCA enhancement, but also

revealed areas of cellular infiltrate undetected by GBCA [35, 36]. Millward *et al.* also described early detection of VSOPs, prior to disease onset, in the choroid plexus and ventricles during EAE [36]. Furthermore, inflammation-induced binding of VSOPs to brain endothelial cells *in vitro* was shown to be mediated by GAGs as enzymatic degradation with hyaluronidase, heparinase III and chondroitinase ABC diminished the uptake of particles [38]. In addition, inhibition of GAG sulfation also reduced VSOPs uptake by endothelial cells, indicating a role of the sulfation pattern of GAGs present in the glycocalyx [38]. Thus, a part of VSOPs detected in the brain accumulated in areas of tissue remodeling promoted by inflammation-induced alterations in GAG composition and sulfation pattern.

Other factors that may explain the distribution and accumulation of VSOPs in the inflamed brain besides binding to endothelial cells [36, 38, 72] include entry of leukocytes (macrophages and T cells), that phagocytosed the particles in the peripheral circulation [35, 73-74] as well as direct diffusion through the damaged BBB. In our study, superimposed contrast was excluded and Eu-VSOP accumulation was investigated separately from GBCA enhancement and 24 hours after their administration, ensuring blood clearance. Eu-VSOPs were also found dispersed in the tissue farther from areas of hypointensity depicted in the T2*-weighted images, possibly as a result of passive diffusion through the damaged BBB. Based on this, we expect that Eu-VSOP accumulation in the brain during EAE primarily derives from uptake by infiltrating leukocytes or local reactive microglia, and/or alterations in the glycocalyx of endothelial cells, rather than immediate diffusion from local BBB disruption. Thus, investigation of stiffness changes in areas of Eu-VSOP accumulation identifies local tissue remodeling induced by neuroinflammation.

In **Study II**, Batzdorf *et al.* [40] set to map the viscoelasticity of different brain regions. No hippocampal, thalamic or global differences in tissue stiffness were detected during EAE. The lack of global stiffness changes may result from the analysis confined to a single slice in the native space, in contrast to the analysis within the bregma coordinate -2.84 to 0.23 mm in the elastograms evaluated in **Study I**. Despite this limitation, the cortex was the main brain region affected, displaying reduced stiffness at peak EAE.

The identification of cortical softening poses a potential marker for disease activity and development. Cortical pathology in MS has gained increasing attention due to the correlation with cognitive impairment and its detection in early stages of disease development, unlike white matter demyelination [75]. Contrasting with white matter demyelinating lesions, cortical lesions are often devoid of leukocyte infiltrate, but are often associated with meningeal inflammation and diffusion of soluble inflammatory factors [76, 77]. In agreement with previous reports in EAE and MS [78, 79], we did not identify cortical leukocyte infiltrates in EAE mice. However, the composition of the cortical BM glycoproteins intrinsically differed in mice at peak EAE compared to naïve mice. In this line, laminins and collagen type IV were upregulated during EAE. The composition of the BM may affect the stiffness of the tissue as BM glycoproteins have been shown to have relevant elastic properties [57, 80-82]. Moreover, remodeling of the BM matrix depends on the effect of neuroinflammation in BM-producing cells, including endothelial cells, astrocytes and oligodendrocytes precursor cells and may affect the interstitial matrix compartment via diffusion into the parenchymal space [83]. For instance, overexpression of collagen or laminin could leak into the parenchymal space and interact with the interstitial matrix and cells, altering the microstructure of the cortical tissue and consequently its mechanical properties. Thus, disease-specific changes of the BM components, the activation state of BM-producing cells or the interaction between the two matrix compartments could contribute to softening in female mice.

Collectively, these findings showed that MRE is sensitive to local alterations in tissue microstructure, as indicated by the investigation of the mechanical properties in areas to Eu-VSOP accumulation and in the cortical tissue. In EAE, during the active phase of the disease (peak), tissue softening was associated with cellular composition and matrix remodeling induced by neuroinflammation. These alterations may prove relevant for assessment of inflammatory activity, which can be additionally integrated in the development phase of pharmacological treatments targeting inflammation as well as for longitudinal monitoring of treatment response. Additionally, the application of experimental MRI tools, such as MRE and Eu-VSOP, may help monitor disease development from a different standpoint, other than classical demyelination. Importantly, these tools have a high translational value as they have been already employed in clinical

studies [12, 13, 15, 84, 85]. In special, MRE is a noninvasive tool shown to be sensitive and applicable to a range of neuroinflammatory conditions [65].

4.2 Neuroinflammation-induced matrix remodeling for disease development

As the results from **Studies I** and **II** indicated, MRE can be used to detect MS-like disease development associated with inflammatory processes using the EAE animal model. This can be explained by the influence of inflammation in ECM remodeling, thus altering the mechanical properties of the brain.

While perivascular lesions revealed by Eu-VSOPs in **Study I** are characterized by intense leukocyte infiltration, cortical tissue damage as detected by MRE in **Study II** was not associated with parenchymal or perivascular infiltrates. As previously discussed, cortical pathology is often linked to meningeal inflammation and microgliosis [77]. In **Study I**, the presence of activated microglia in sites of inflammation and Eu-VSOP accumulation additionally suggests ECM remodeling. Microgliosis is frequently accompanying neuroinflammation in EAE [86, 87] and MS [88]. Together with astrocytes [89] and neurons [90], activated microglia contribute to the release of matrix metalloproteinases (MMP) and, consequently, ECM remodeling [91, 92]. This indicates that gliosis observed in areas of Eu-VSOP may play a role in ECM integrity. A dynamic indentation study demonstrated reduced elasticity in myelin-phagocytosing microglial cells [93]. Therefore, local tissue softening in areas of Eu-VSOP accumulation stems from a combination of inflammatory events mediating particle accumulation that involve reactive gliosis, leukocyte infiltration and remodeling of the ECM.

In **Study II**, elevated expression of the BM (glyco)proteins *Lama4*, *Lama5*, *Col4a1* in the cortex of female EAE mice compared to healthy mice demonstrated inflammation-induced remodeling of the ECM. This finding is in accordance with investigation of ECM composition in MS patients, in which both laminin α 4 and collagen type IV were accumulated in active lesions associated with microglia and infiltrating leukocytes [94, 95]. Although a protective role of elevated BM (glyco)proteins has been speculated, limiting the extent of damage and leukocyte migration, BM remodeling could have an

additional effect on remyelination [96]. For instance, while collagen type IV accumulation is thought to inhibit oligodendrocyte precursor cells (OPC) [96], laminin $\alpha 4$ was shown to have a positive effect on OPCs, promoting migration and increasing survival [97]. Our data indicate ECM remodeling in the BM at the peak phase of EAE, but the exact role of the BM components may depend on the extent of accumulation or evolution and/or chronicity of the lesions. It is possible that BM remodeling precedes BBB leakage and leukocyte infiltration. Thus, exacerbated upregulation of BM components at peak EAE may influence leukocyte migration in later phases.

Other important structural and functional components of the ECM are GAGs, which have been shown to be relevant in neuroinflammation [98]. In **Study III**, investigation of the expression of enzymes involved in GAG metabolism and quantification of GAG disaccharides showed that early transcription of enzymes involved in GAG metabolism are followed by changes in HA and CS-4S disaccharides fractions. Genes involved in degradation of GAGs were upregulated at the pre-onset phase, namely *Hpse*, *Hexb* and *Gusb*, indicating GAG breakdown at the beginning of neuroinflammation. Indeed, when total GAG disaccharides resulting from ChABC digestion were quantified, a reduction of about 40% was found in the cerebellum of EAE mice compared to CFA controls. Hexosaminidase β (*Hexb*) and β -glucuronidase (*Gusb*) are lysosomal enzymes that degrade all types of GAGs [99]. Given the compartmentalization of these enzymes, we would expect that an early oxidative depolymerization of GAGs would precede lysosomal degradation. In fact, it is for a long time known that reactive oxygen species (ROS) participate in the depolymerization of GAGs and ROS-producing neutrophils induce degradation of HA, DS and CS GAGs [100, 101]. In the context of EAE, as well as of MS, oxidative stress induced by ROS is produced by infiltrating leukocytes and microglia and contributes to neuroaxonal damage [102-104]. Among the CS disaccharides found in the brain, our data showed that CS-4S was the predominant fraction and was reduced in the cerebellum during peak and remission phases of EAE. Other reports also indicate CS-4S as the most abundant fraction in the brain [28].

The reduction of CS GAGs in the brain ECM may further amplify and sustain the inflammatory response as GAGs play an important role in the homeostasis of ions and

soluble factors acting as reservoir [98]. Upon degradation, it can be expected that the diffusivity of cytokines, chemokines, growth and other soluble factors in the extracellular space is increased, allowing for an enhanced interaction with their respective receptors. In this regard, the reduction of CS GAGs in the brain ECM may translate in further amplification and maintenance of the inflammatory response. Hence, production of ROS during neuroinflammation induces overall CS GAGs breakdown, which in turn modify the structural organization of the tissue, possibly influencing tissue mechanics, and contributing to the diffusivity of inflammatory soluble factors and, ultimately, disease development.

Previously, histological assessment of EAE cerebellum showed an accumulation of CS-4S, CS-6S, and CSPGs within perivascular lesions, which were associated with enhanced leukocyte migration [105]. In our study, CS-4S GAGs histologically detected in the cerebellar tissue revealed a heterogenous distribution, with accumulation in some perivascular infiltrates and absence in others. One hypothesis to explain this heterogeneity lays on the chronological development of these lesions. Possibly, CS GAGs accumulate in recently formed lesion attracting peripheral leucocytes, while lesions devoid of CS GAGs may represent resolving lesions. Nonetheless, alterations in CS GAGs may represent a marker of ongoing inflammation during EAE.

Another role mediated by GAGs include direct ECM-cell interaction. HA for instance can directly activate transmembrane proteins and mediate a range of physiological and inflammatory processes. Under physiological conditions, HA binding to CD44 is involved in regulation of cellular migration, differentiation, and proliferation [106]. We found a sustained upregulation of *Has2* during EAE followed by an increase in HA disaccharides at peak. Such as CS, HA is subjected to ROS-mediated breakdown during inflammation [107]. However, the increase in HA disaccharides can be explained by a HAS2-mediated synthesis of new HA chains. HA fragments have been proposed to interact with Toll-like receptors [108] and bind to CD44 leading to the activation of downstream inflammatory cascades [109]. CD44 expression has been reported to be induced in astrocytes in chronic MS lesions and in T cells from relapsing patients [31, 110]. In MS, increased levels of HA are thought to be initially produced by CD4⁺ T cells and microglia and at a

later stage by astrocytes [31]. HA derived from astrocytes has been also found to accumulate in the borders of MS lesions and inhibit oligodendrocyte precursor cell maturation *in vitro* [31]. Furthermore, HA accumulation in EAE lesions facilitates leukocyte trafficking [111], suggesting a pro-inflammatory role. Using 4-methylumbelliferone, a HAS2 and HAS3 inhibitor, to suppress HA synthesis led to delayed EAE development and attenuated disease severity accompanied by a reduction of T cell trafficking and astrogliosis [32]. Altogether, these findings point to a role of HA synthesis and homeostasis in the development and progression of EAE. It can be hypothesized that, in a first moment, accumulating HA may derive from astrocytes and T cells via *Has2* induction, which would promote inflammation at peak EAE. Afterwards, in the remission phase, it is possible that production of HA is undertaken by astrocytes leading to a sustained mild inflammation, and possibly playing a role in T cell infiltration in upcoming relapses.

Altogether, ECM remodeling was found to occur at different degrees in different brain areas during neuroinflammation. Differential expression of cortical BM components and GAG composition in the cerebellum of EAE mice point to an extensive remodeling of the brain ECM. Besides the pathophysiological role of CS and HA GAGs, it is noteworthy to highlight their implications to brain tissue mechanics. An example is that HA is often found cross-linked by CSPGs and other link proteins such as tenascin [112] and its chemical cross-linking *in vitro* is associated with altered mechanical properties of HA-containing gels [113, 114]. Therefore, the effect of ECM modifications on brain tissue structure and mechanical properties may be targeted for monitoring of neuroinflammation using *in vivo* MRE.

4.3 Limitations of the studies

Investigation of the mechanical properties of the brain tissue, as employed in **Studies I** and **II**, presents valuable information regarding the microstructural alterations induced by neuroinflammation in the EAE model, which are readily translatable to the human MS pathology as already demonstrated in clinical studies [12, 13]. However, although the cerebellum is a highly susceptible region in animal model [17, 61, 63], due to technical

constraints, it could not be included in **Studies I** and **II**. Given the significant remodeling reported in the cerebellar tissue in **Study III**, information on the mechanical behavior of this area is indispensable to confirm the direct contribution of ECM remodeling to tissue mechanics.

The heterogeneity in GAGs chains still imposes a challenge for their quantification and biological function. To overcome this limitation, we employed a quantitative analysis of GAG disaccharides after enzymatic digestion with chondroitinase lyase. Although we were successfully able to quantify the main fraction of CS GAGs as well as HA, our analytical method could not determine the amounts of HS and DS present in the brain matrix. As gene expression data suggested, there are possibly important modifications in these two GAG families during EAE. On the one hand, overexpression of transcript of DS epimerase, which converts of GlcA into IduA forming DS GAGs, and decorin, a major DS/CSPG, would indicate a possible increase in DS GAGs. On the other hand, a strong induction of *Hpse* would suggest degradation of HS chains. Given limitations in the loading capacity as well as detection of the analytical system used for GAG disaccharide quantification, none of these GAG families were found in detectible or quantifiable amounts in our samples (see Supplementary Fig. 2 and 8 in Silva *et al.* [41]). For this purpose, larger amounts of starting material and a different analytical system are likely needed. Moreover, although gene expression data indicated disease-induced modulation of various GAG- and PG-associated genes, information on protein levels of these genes should still be investigated as well as their cellular source. Information on protein levels and enzyme activity of such genes in future work is determinant to evaluate their potential as targets for the development of imaging probes or their implication in therapeutic interventions.

4.4 Clinical implications and future directions

The translational potential of the quantification of mechanical properties of the brain represents a considerable strength of MRE studies. MRE is successfully employed for clinical detection and staging of liver fibrosis [115] but it has been also applied to brain pathologies [116]. The influence of the ECM on tissue mechanics is widely acknowledged.

In the liver, collagen, the main ECM component, accumulates during fibrosis and its content correlates with liver stiffening [117].

Naturally, in the context of the CNS, the ECM presents a more complex architecture and varies in different microenvironments, being subdivided into compartments: BM, perineuronal nets and interstitial matrix [118]. The summed alterations in each compartment may produce the observed disseminated softening. Moreover, MS is a complex neuroinflammatory and neurodegenerative disease. Pathological processes such as white matter demyelination, cortical demyelination, and chronic inflammation may contribute distinctively to the different clinical manifestations. However, insufficient imaging markers available in clinical practice often leads to imprecise distinction among the various types of MS during the diagnostic phase. Consequently, therapeutical interventions are often based on the pattern of demyelination and clinical manifestation. Patients with similar symptoms may be classified with the same phenotype but may present distinct underlying pathology. In this regard, it seems crucial to map regional tissue mechanics and understand how glycoproteins, PGs and GAGs are affected across the brain in the course of inflammation. This may prove useful as imaging marker for assessment of MS pathology, improve diagnostics as well as monitor treatment response. For this to happen, the causal relationship between regionally resolved ECM changes and tissue stiffness needs to be assessed.

A second application emerging from the study of the brain ECM, in particular GAGs, is the identification of neuroinflammatory biomarkers for development of molecular imaging probes. For instance, targeting fibrin deposition using the peptide-conjugated GBCA-based molecular MRI probe, EP2104-R, effectively detected fibrin accumulation in the perivascular and subarachnoid space, which correlated with disease disability [119]. Such approach could be similarly applied, for instance, for identification of CS-4S or HA cross-linking proteins to investigate longitudinally *in vivo* and chronological emergence of cerebral ECM remodeling in the course of neuroinflammation. Furthermore, since the ECM affects cellular activity, differentiation, and migration, tracing ECM remodeling with molecular probes would be important for *in vivo* investigation of the effect of the ECM changes in processes of de- and remyelination.

5 Conclusions

Together, the studies compiled in this thesis used the murine EAE model to investigate inflammation-induced alterations in brain tissue and ECM. The results revealed an extensive tissue remodeling in the inflamed brain that could be sensed using MRI-based tools during EAE.

Loss of tissue stiffness, as measured by MRE, is influenced by leukocyte infiltrate, gliosis and an altered brain matrix. These findings evidenced the applicability of MRE as an imaging tool for longitudinal *in vivo* investigation of neuroinflammation. Furthermore, the altered composition of GAGs, particularly affecting HA-0S and CS-4S fractions, and ECM-related transcriptional changes observed in early disease phases, indicates a potential point of intervention to hamper progression of inflammation.

Altogether, this thesis demonstrates that matrix remodeling during neuroinflammation leads to alteration of tissue mechanics that can be visualized non-invasively by MRE.

6 Reference list

1. Thompson AJ, Baranzini SE, Geurts J, Hemmer B, Ciccarelli O. Multiple sclerosis. *Lancet*. 2018;391(10130):1622-36.
2. Walton C, King R, Rechtman L, Kaye W, Leray E, Marrie RA, Robertson N, La Rocca N, Uitdehaag B, van der Mei I, Wallin M, Helme A, Angood Napier C, Rijke N, Baneke P. Rising prevalence of multiple sclerosis worldwide: Insights from the Atlas of MS, third edition. *Mult Scler*. 2020;26(14):1816-21.
3. Zéphir H. Progress in understanding the pathophysiology of multiple sclerosis. *Rev Neurol (Paris)*. 2018;174(6):358-63.
4. Salzer JL, Zalc B. Myelination. *Curr Biol*. 2016;26(20):R971-r5.
5. Pitt D, Lo CH, Gauthier SA, Hickman RA, Longbrake E, Airas LM, Mao-Draayer Y, Riley C, De Jager PL, Wesley S, Boster A, Topalli I, Bagnato F, Mansoor M, Stuve O, Kister I, Pelletier D, Stathopoulos P, Dutta R, Lincoln MR. Toward Precision Phenotyping of Multiple Sclerosis. *Neurol Neuroimmunol Neuroinflamm*. 2022;9(6).
6. Engelhard J, Oleske DM, Schmitting S, Wells KE, Talapala S, Barbato LM. Multiple sclerosis by phenotype in Germany. *Mult Scler Relat Disord*. 2022;57:103326.
7. Polman CH, Reingold SC, Banwell B, Clanet M, Cohen JA, Filippi M, Fujihara K, Havrdova E, Hutchinson M, Kappos L, Lublin FD, Montalban X, O'Connor P, Sandberg-Wollheim M, Thompson AJ, Waubant E, Weinshenker B, Wolinsky JS. Diagnostic criteria for multiple sclerosis: 2010 revisions to the McDonald criteria. *Ann Neurol*. 2011;69(2):292-302.
8. Thompson AJ, Banwell BL, Barkhof F, Carroll WM, Coetzee T, Comi G, Correale J, Fazekas F, Filippi M, Freedman MS. Diagnosis of multiple sclerosis: 2017 revisions of the McDonald criteria. *The Lancet Neurology*. 2018;17(2):162-73.
9. Barkhof F. The clinico-radiological paradox in multiple sclerosis revisited. *Curr Opin Neurol*. 2002;15(3):239-45.
10. Hirsch S, Braun J, Sack I. *Magnetic resonance elastography: physical background and medical applications*: John Wiley & Sons; 2017.
11. Fehlner A, Behrens JR, Streitberger KJ, Papazoglou S, Braun J, Bellmann-Strobl J, Ruprecht K, Paul F, Würfel J, Sack I. Higher-resolution MR elastography reveals early mechanical signatures of neuroinflammation in patients with clinically isolated syndrome. *J Magn Reson Imaging*. 2016;44(1):51-8.
12. Streitberger K-J, Sack I, Krefting D, Pfüller C, Braun J, Paul F, Wuerfel J. Brain viscoelasticity alteration in chronic-progressive multiple sclerosis. *PloS one*. 2012;7(1):e29888.
13. Wuerfel J, Paul F, Beierbach B, Hamhaber U, Klatt D, Papazoglou S, Zipp F, Martus P, Braun J, Sack I. MR-elastography reveals degradation of tissue integrity in multiple sclerosis. *Neuroimage*. 2010;49(3):2520-5.
14. Hiscox LV, Johnson CL, McGarry MD, Marshall H, Ritchie CW, Van Beek EJ, Roberts N, Starr JM. Mechanical property alterations across the cerebral cortex due to Alzheimer's disease. *Brain communications*. 2020;2(1):fcz049.

15. Lipp A, Trbojevic R, Paul F, Fehlner A, Hirsch S, Scheel M, Noack C, Braun J, Sack I. Cerebral magnetic resonance elastography in supranuclear palsy and idiopathic Parkinson's disease. *NeuroImage: Clinical*. 2013;3:381-7.
 16. Riek K, Millward JM, Hamann I, Mueller S, Pfueller CF, Paul F, Braun J, Infante-Duarte C, Sack I. Magnetic resonance elastography reveals altered brain viscoelasticity in experimental autoimmune encephalomyelitis. *Neuroimage Clin*. 2012;1(1):81-90.
 17. Millward JM, Guo J, Berndt D, Braun J, Sack I, Infante-Duarte C. Tissue structure and inflammatory processes shape viscoelastic properties of the mouse brain. *NMR Biomed*. 2015;28(7):831-9.
 18. Wang S, Millward JM, Hanke-Vela L, Malla B, Pilch K, Gil-Infante A, Waiczies S, Mueller S, Boehm-Sturm P, Guo J, Sack I, Infante-Duarte C. MR Elastography-Based Assessment of Matrix Remodeling at Lesion Sites Associated With Clinical Severity in a Model of Multiple Sclerosis. *Front Neurol*. 2019;10:1382.
 19. Bandtlow CE, Zimmermann DR. Proteoglycans in the developing brain: new conceptual insights for old proteins. *Physiol Rev*. 2000;80(4):1267-90.
 20. Sonntag M, Blosa M, Schmidt S, Reimann K, Blum K, Eckrich T, Seeger G, Hecker D, Schick B, Arendt T, Engel J, Morawski M. Synaptic coupling of inner ear sensory cells is controlled by brevican-based extracellular matrix baskets resembling perineuronal nets. *BMC Biol*. 2018;16(1):99.
 21. Kantor DB, Chivatakarn O, Peer KL, Oster SF, Inatani M, Hansen MJ, Flanagan JG, Yamaguchi Y, Sretavan DW, Giger RJ, Kolodkin AL. Semaphorin 5A is a bifunctional axon guidance cue regulated by heparan and chondroitin sulfate proteoglycans. *Neuron*. 2004;44(6):961-75.
 22. Matsumoto Y, Irie F, Inatani M, Tessier-Lavigne M, Yamaguchi Y. Netrin-1/DCC signaling in commissural axon guidance requires cell-autonomous expression of heparan sulfate. *J Neurosci*. 2007;27(16):4342-50.
 23. Yamaguchi Y. Lecticans: organizers of the brain extracellular matrix. *Cell Mol Life Sci*. 2000;57(2):276-89.
 24. Nicholson C, Rice ME. The migration of substances in the neuronal microenvironment. *Ann N Y Acad Sci*. 1986;481:55-71.
 25. Novak U, Kaye AH. Extracellular matrix and the brain: components and function. *J Clin Neurosci*. 2000;7(4):280-90.
 26. Carulli D, Pizzorusso T, Kwok JC, Putignano E, Poli A, Forostyak S, Andrews MR, Deepa SS, Glant TT, Fawcett JW. Animals lacking link protein have attenuated perineuronal nets and persistent plasticity. *Brain*. 2010;133(Pt 8):2331-47.
 27. Lindahl U, Couchman J, Kimata K, Esko JD. Proteoglycans and Sulfated Glycosaminoglycans. In: Varki A, Cummings RD, Esko JD, Stanley P, Hart GW, Aebi M, et al., editors. *Essentials of Glycobiology*. Cold Spring Harbor (NY): Cold Spring Harbor Laboratory Press
- Copyright 2015-2017 by The Consortium of Glycobiology Editors, La Jolla, California. All rights reserved.; 2015. p. 207-21.
28. Alonge KM, Logsdon AF, Murphree TA, Banks WA, Keene CD, Edgar JS, Whittington D, Schwartz MW, Guttman M. Quantitative analysis of chondroitin

- sulfate disaccharides from human and rodent fixed brain tissue by electrospray ionization-tandem mass spectrometry. *Glycobiology*. 2019;29(12):847-60.
29. Gilbert RJ, McKeon RJ, Darr A, Calabro A, Hascall VC, Bellamkonda RV. CS-4,6 is differentially upregulated in glial scar and is a potent inhibitor of neurite extension. *Mol Cell Neurosci*. 2005;29(4):545-58.
 30. Sobel RA, Ahmed AS. White matter extracellular matrix chondroitin sulfate/dermatan sulfate proteoglycans in multiple sclerosis. *J Neuropathol Exp Neurol*. 2001;60(12):1198-207.
 31. Back SA, Tuohy TM, Chen H, Wallingford N, Craig A, Struve J, Luo NL, Banine F, Liu Y, Chang A, Trapp BD, Bebo BF, Jr., Rao MS, Sherman LS. Hyaluronan accumulates in demyelinated lesions and inhibits oligodendrocyte progenitor maturation. *Nat Med*. 2005;11(9):966-72.
 32. Kuipers HF, Rieck M, Gurevich I, Nagy N, Butte MJ, Negrin RS, Wight TN, Steinman L, Bollyky PL. Hyaluronan synthesis is necessary for autoreactive T-cell trafficking, activation, and Th1 polarization. *Proc Natl Acad Sci U S A*. 2016;113(5):1339-44.
 33. Keough MB, Rogers JA, Zhang P, Jensen SK, Stephenson EL, Chen T, Hurlbert MG, Lau LW, Rawji KS, Plemel JR, Koch M, Ling CC, Yong VW. An inhibitor of chondroitin sulfate proteoglycan synthesis promotes central nervous system remyelination. *Nat Commun*. 2016;7:11312.
 34. Gerwien H, Hermann S, Zhang X, Korpos E, Song J, Kopka K, Faust A, Wenning C, Gross CC, Honold L, Melzer N, Opdenakker G, Wiendl H, Schäfers M, Sorokin L. Imaging matrix metalloproteinase activity in multiple sclerosis as a specific marker of leukocyte penetration of the blood-brain barrier. *Sci Transl Med*. 2016;8(364):364ra152.
 35. Tysiak E, Asbach P, Aktas O, Waiczies H, Smyth M, Schnorr J, Taupitz M, Wuerfel J. Beyond blood brain barrier breakdown—in vivo detection of occult neuroinflammatory foci by magnetic nanoparticles in high field MRI. *Journal of Neuroinflammation*. 2009;6(1):1-8.
 36. Millward JM, Schnorr J, Taupitz M, Wagner S, Wuerfel JT, Infante-Duarte C. Iron oxide magnetic nanoparticles highlight early involvement of the choroid plexus in central nervous system inflammation. *ASN Neuro*. 2013;5(1):e00110.
 37. Wuerfel J, Tysiak E, Prozorovski T, Smyth M, Mueller S, Schnorr J, Taupitz M, Zipp F. Mouse model mimics multiple sclerosis in the clinico-radiological paradox. *European Journal of Neuroscience*. 2007;26(1):190-8.
 38. Berndt D, Millward JM, Schnorr J, Taupitz M, Stangl V, Paul F, Wagner S, Wuerfel JT, Sack I, Ludwig A, Infante-Duarte C. Inflammation-induced brain endothelial activation leads to uptake of electrostatically stabilized iron oxide nanoparticles via sulfated glycosaminoglycans. *Nanomedicine*. 2017;13(4):1411-21.
 39. Silva RV, Morr AS, Mueller S, Koch SP, Boehm-Sturm P, Rodriguez-Sillke Y, Kunkel D, Tzschätzsch H, Kühl AA, Schnorr J, Taupitz M, Sack I, Infante-Duarte C. Contribution of Tissue Inflammation and Blood-Brain Barrier Disruption to Brain Softening in a Mouse Model of Multiple Sclerosis. *Front Neurosci*. 2021;15:701308.

40. Batzdorf CS, Morr AS, Bertalan G, Sack I, Silva RV, Infante-Duarte C. Sexual Dimorphism in Extracellular Matrix Composition and Viscoelasticity of the Healthy and Inflamed Mouse Brain. *Biology (Basel)*. 2022;11(2).
41. Silva RV, Biskup K, Zabala-Jouvin JK, Batzdorf CS, Stellmach C, Morr AS, Sack I, Ludwig A, Blanchard V, Infante-Duarte C. Brain inflammation induces alterations in glycosaminoglycan metabolism and subsequent changes in CS-4S and hyaluronic acid. *Int J Biol Macromol*. 2023;230:123214.
42. Constantinescu CS, Farooqi N, O'Brien K, Gran B. Experimental autoimmune encephalomyelitis (EAE) as a model for multiple sclerosis (MS). *Br J Pharmacol*. 2011;164(4):1079-106.
43. Kipp M, Nyamoya S, Hochstrasser T, Amor S. Multiple sclerosis animal models: a clinical and histopathological perspective. *Brain Pathol*. 2017;27(2):123-37.
44. Louveau A, Herz J, Alme MN, Salvador AF, Dong MQ, Viar KE, Herod SG, Knopp J, Setliff JC, Lupi AL, Da Mesquita S, Frost EL, Gaultier A, Harris TH, Cao R, Hu S, Lukens JR, Smirnov I, Overall CC, Oliver G, Kipnis J. CNS lymphatic drainage and neuroinflammation are regulated by meningeal lymphatic vasculature. *Nat Neurosci*. 2018;21(10):1380-91.
45. Schropp V, Rohde J, Rovituso DM, Jabari S, Bharti R, Kuerten S. Contribution of LTi and T(H)17 cells to B cell aggregate formation in the central nervous system in a mouse model of multiple sclerosis. *J Neuroinflammation*. 2019;16(1):111.
46. Tuohy VK, Lu Z, Sobel RA, Laursen RA, Lees MB. Identification of an encephalitogenic determinant of myelin proteolipid protein for SJL mice. *J Immunol*. 1989;142(5):1523-7.
47. Miller SD, Karpus WJ, Davidson TS. Experimental autoimmune encephalomyelitis in the mouse. *Curr Protoc Immunol*. 2010;Chapter 15:Unit 15.1.
48. Procaccini C, De Rosa V, Pucino V, Formisano L, Matarese G. Animal models of Multiple Sclerosis. *Eur J Pharmacol*. 2015;759:182-91.
49. Minhas AS, Oliver R. Magnetic Resonance Imaging Basics. In: Sadleir R, Minhas AS, editors. *Electrical Properties of Tissues: Quantitative Magnetic Resonance Mapping*. Cham: Springer International Publishing; 2022. p. 47-82.
50. Hao D, Ai T, Goerner F, Hu X, Runge VM, Tweedle M. MRI contrast agents: basic chemistry and safety. *J Magn Reson Imaging*. 2012;36(5):1060-71.
51. Bertalan G, Guo J, Tzschätzsch H, Klein C, Barnhill E, Sack I, Braun J. Fast tomoelastography of the mouse brain by multifrequency single-shot MR elastography. *Magn Reson Med*. 2019;81(4):2676-87.
52. Koch S, Mueller S, Foddiss M, Bienert T, von Elverfeldt D, Knab F, Farr TD, Bernard R, Dopatka M, Rex A. Atlas registration for edema-corrected MRI lesion volume in mouse stroke models. *Journal of Cerebral Blood Flow & Metabolism*. 2019;39(2):313-23.
53. Guo J, Bertalan G, Meierhofer D, Klein C, Schreyer S, Steiner B, Wang S, da Silva RV, Infante-Duarte C, Koch S. Brain maturation is associated with increasing tissue stiffness and decreasing tissue fluidity. *Acta biomaterialia*. 2019;99:433-42.

54. Klein S, Staring M, Murphy K, Viergever MA, Pluim JP. Elastix: a toolbox for intensity-based medical image registration. *IEEE transactions on medical imaging*. 2009;29(1):196-205.
55. Volpi N, Galeotti F, Yang B, Linhardt RJ. Analysis of glycosaminoglycan-derived, precolumn, 2-aminoacridone-labeled disaccharides with LC-fluorescence and LC-MS detection. *Nat Protoc*. 2014;9(3):541-58.
56. Bolstad BM, Irizarry RA, Astrand M, Speed TP. A comparison of normalization methods for high density oligonucleotide array data based on variance and bias. *Bioinformatics*. 2003;19(2):185-93.
57. Miller RT. Mechanical properties of basement membrane in health and disease. *Matrix Biol*. 2017;57-58:366-73.
58. Leclech C, Natale CF, Barakat AI. The basement membrane as a structured surface - role in vascular health and disease. *J Cell Sci*. 2020;133(18).
59. Schmittgen TD, Livak KJ. Analyzing real-time PCR data by the comparative C(T) method. *Nat Protoc*. 2008;3(6):1101-8.
60. Giesen C, Wang HA, Schapiro D, Zivanovic N, Jacobs A, Hattendorf B, Schüffler PJ, Grolimund D, Buhmann JM, Brandt S, Varga Z, Wild PJ, Günther D, Bodenmiller B. Highly multiplexed imaging of tumor tissues with subcellular resolution by mass cytometry. *Nat Methods*. 2014;11(4):417-22.
61. Wang S, Millward JM, Hanke-Vela L, Malla B, Pilch K, Gil-Infante A, Waiczies S, Mueller S, Boehm-Sturm P, Guo J. MR elastography-based assessment of matrix remodeling at lesion sites associated with clinical severity in a model of multiple sclerosis. *Frontiers in neurology*. 2020;10:1382.
62. Royston P. Remark AS R94: A Remark on Algorithm AS 181: The W-test for Normality. *Journal of the Royal Statistical Society*. 1995;44:547-51.
63. Tonra JR. Cerebellar susceptibility to experimental autoimmune encephalomyelitis in SJL/J mice: potential interaction of immunology with vascular anatomy. *Cerebellum*. 2002;1(1):57-68.
64. Voet S, Prinz M, van Loo G. Microglia in Central Nervous System Inflammation and Multiple Sclerosis Pathology. *Trends Mol Med*. 2019;25(2):112-23.
65. Murphy MC, Huston J, 3rd, Ehman RL. MR elastography of the brain and its application in neurological diseases. *Neuroimage*. 2019;187:176-83.
66. Bertalan G, Guo J, Tzschätzsch H, Klein C, Barnhill E, Sack I, Braun J. Fast tomoelastography of the mouse brain by multifrequency single-shot MR elastography. *Magnetic Resonance in Medicine*. 2019;81(4):2676-87.
67. Bertalan G, Klein C, Schreyer S, Steiner B, Kreft B, Tzschätzsch H, de Schellenberger AA, Nieminen-Kelhä M, Braun J, Guo J, Sack I. Biomechanical properties of the hypoxic and dying brain quantified by magnetic resonance elastography. *Acta Biomater*. 2020;101:395-402.
68. Lassmann H. The pathologic substrate of magnetic resonance alterations in multiple sclerosis. *Neuroimaging clinics of North America*. 2008;18(4):563-76.
69. Aime S, Caravan P. Biodistribution of gadolinium-based contrast agents, including gadolinium deposition. *Journal of Magnetic Resonance Imaging: An Official*

- Journal of the International Society for Magnetic Resonance in Medicine. 2009;30(6):1259-67.
70. Layne KA, Dargan PI, Archer JRH, Wood DM. Gadolinium deposition and the potential for toxicological sequelae - A literature review of issues surrounding gadolinium-based contrast agents. *Br J Clin Pharmacol*. 2018;84(11):2522-34.
 71. Nessler S, Boretius S, Stadelmann C, Bittner A, Merkler D, Hartung HP, Michaelis T, Brück W, Frahm J, Sommer N, Hemmer B. Early MRI changes in a mouse model of multiple sclerosis are predictive of severe inflammatory tissue damage. *Brain*. 2007;130(Pt 8):2186-98.
 72. Millward JM, Ariza de Schellenberger A, Berndt D, Hanke-Vela L, Schellenberger E, Waiczies S, Taupitz M, Kobayashi Y, Wagner S, Infante-Duarte C. Application of Europium-Doped Very Small Iron Oxide Nanoparticles to Visualize Neuroinflammation with MRI and Fluorescence Microscopy. *Neuroscience*. 2019;403:136-44.
 73. Wuerfel E, Smyth M, Millward JM, Schellenberger E, Glumm J, Prozorovski T, Aktas O, Schulze-Topphoff U, Schnorr J, Wagner S, Taupitz M, Infante-Duarte C, Wuerfel J. Electrostatically Stabilized Magnetic Nanoparticles - An Optimized Protocol to Label Murine T Cells for in vivo MRI. *Front Neurol*. 2011;2:72.
 74. Oude Engberink RD, Blezer EL, Dijkstra CD, van der Pol SM, van der Toorn A, de Vries HE. Dynamics and fate of USPIO in the central nervous system in experimental autoimmune encephalomyelitis. *NMR Biomed*. 2010;23(9):1087-96.
 75. Calabrese M, Filippi M, Gallo P. Cortical lesions in multiple sclerosis. *Nat Rev Neurol*. 2010;6(8):438-44.
 76. Stadelmann C, Albert M, Wegner C, Brück W. Cortical pathology in multiple sclerosis. *Curr Opin Neurol*. 2008;21(3):229-34.
 77. Junker A, Wozniak J, Voigt D, Scheidt U, Antel J, Wegner C, Brück W, Stadelmann C. Extensive subpial cortical demyelination is specific to multiple sclerosis. *Brain Pathol*. 2020;30(3):641-52.
 78. Potter LE, Paylor JW, Suh JS, Tenorio G, Caliaperumal J, Colbourne F, Baker G, Winship I, Kerr BJ. Altered excitatory-inhibitory balance within somatosensory cortex is associated with enhanced plasticity and pain sensitivity in a mouse model of multiple sclerosis. *Journal of neuroinflammation*. 2016;13(1):1-20.
 79. Popescu BF, Lucchinetti CF. Meningeal and cortical grey matter pathology in multiple sclerosis. *BMC Neurol*. 2012;12:11.
 80. Bhave G, Colon S, Ferrell N. The sulfilimine cross-link of collagen IV contributes to kidney tubular basement membrane stiffness. *American Journal of Physiology-Renal Physiology*. 2017;313(3):F596-F602.
 81. Candiello J, Balasubramani M, Schreiber EM, Cole GJ, Mayer U, Halfter W, Lin H. Biomechanical properties of native basement membranes. *The FEBS Journal*. 2007;274(11):2897-908.
 82. Storm C, Pastore JJ, MacKintosh FC, Lubensky TC, Janmey PA. Nonlinear elasticity in biological gels. *Nature*. 2005;435(7039):191-4.

83. Ulbrich P, Khoshneviszadeh M, Jandke S, Schreiber S, Dityatev A. Interplay between perivascular and perineuronal extracellular matrix remodelling in neurological and psychiatric diseases. *Eur J Neurosci.* 2021;53(12):3811-30.
84. Murphy MC, Jones DT, Jack Jr CR, Glaser KJ, Senjem ML, Manduca A, Felmlee JP, Carter RE, Ehman RL, Huston III J. Regional brain stiffness changes across the Alzheimer's disease spectrum. *NeuroImage: Clinical.* 2016;10:283-90.
85. Solamen LM, McGarry MDJ, Fried J, Weaver JB, Lollis SS, Paulsen KD. Poroelastic Mechanical Properties of the Brain Tissue of Normal Pressure Hydrocephalus Patients During Lumbar Drain Treatment Using Intrinsic Actuation MR Elastography. *Academic Radiology.* 2021;28(4):457-66.
86. Chanaday N, Roth G. Microglia and astrocyte activation in the frontal cortex of rats with experimental autoimmune encephalomyelitis. *Neuroscience.* 2016;314:160-9.
87. Ponomarev ED, Shriver LP, Maresz K, Dittel BN. Microglial cell activation and proliferation precedes the onset of CNS autoimmunity. *J Neurosci Res.* 2005;81(3):374-89.
88. Melief J, Schuurman KG, van de Garde MD, Smolders J, van Eijk M, Hamann J, Huitinga I. Microglia in normal appearing white matter of multiple sclerosis are alerted but immunosuppressed. *Glia.* 2013;61(11):1848-61.
89. Ogier C, Bernard A, Chollet AM, T LED, Hanessian S, Charton G, Khrestchatsky M, Rivera S. Matrix metalloproteinase-2 (MMP-2) regulates astrocyte motility in connection with the actin cytoskeleton and integrins. *Glia.* 2006;54(4):272-84.
90. Gray E, Thomas TL, Betmouni S, Scolding N, Love S. Elevated matrix metalloproteinase-9 and degradation of perineuronal nets in cerebrocortical multiple sclerosis plaques. *J Neuropathol Exp Neurol.* 2008;67(9):888-99.
91. Könnecke H, Bechmann I. The role of microglia and matrix metalloproteinases involvement in neuroinflammation and gliomas. *Clin Dev Immunol.* 2013;2013:914104.
92. Lindberg RL, De Groot CJ, Montagne L, Freitag P, van der Valk P, Kappos L, Leppert D. The expression profile of matrix metalloproteinases (MMPs) and their inhibitors (TIMPs) in lesions and normal appearing white matter of multiple sclerosis. *Brain.* 2001;124(Pt 9):1743-53.
93. van Wageningen TA, Antonovaite N, Paardekam E, Brevé JJP, Iannuzzi D, van Dam AM. Viscoelastic properties of white and gray matter-derived microglia differentiate upon treatment with lipopolysaccharide but not upon treatment with myelin. *J Neuroinflammation.* 2021;18(1):83.
94. van Horssen J, Bö L, Dijkstra CD, de Vries HE. Extensive extracellular matrix depositions in active multiple sclerosis lesions. *Neurobiol Dis.* 2006;24(3):484-91.
95. Mohan H, Krumbholz M, Sharma R, Eisele S, Junker A, Sixt M, Newcombe J, Wekerle H, Hohlfeld R, Lassmann H, Meinl E. Extracellular matrix in multiple sclerosis lesions: Fibrillar collagens, biglycan and decorin are upregulated and associated with infiltrating immune cells. *Brain Pathol.* 2010;20(5):966-75.
96. Ghorbani S, Yong VW. The extracellular matrix as modifier of neuroinflammation and remyelination in multiple sclerosis. *Brain.* 2021;144(7):1958-73.

97. Suzuki N, Hyodo M, Hayashi C, Mabuchi Y, Sekimoto K, Onchi C, Sekiguchi K, Akazawa C. Laminin $\alpha 2$, $\alpha 4$, and $\alpha 5$ Chains Positively Regulate Migration and Survival of Oligodendrocyte Precursor Cells. *Sci Rep*. 2019;9(1):19882.
98. Smith PD, Coulson-Thomas VJ, Foscari S, Kwok JC, Fawcett JW. "GAG-ing with the neuron": The role of glycosaminoglycan patterning in the central nervous system. *Exp Neurol*. 2015;274(Pt B):100-14.
99. Ernst S, Langer R, Cooney CL, Sasisekharan R. Enzymatic degradation of glycosaminoglycans. *Crit Rev Biochem Mol Biol*. 1995;30(5):387-444.
100. Moseley R, Waddington RJ, Embery G. Degradation of glycosaminoglycans by reactive oxygen species derived from stimulated polymorphonuclear leukocytes. *Biochim Biophys Acta*. 1997;1362(2-3):221-31.
101. Duan J, Kasper DL. Oxidative depolymerization of polysaccharides by reactive oxygen/nitrogen species. *Glycobiology*. 2011;21(4):401-9.
102. Mossakowski AA, Pohlan J, Bremer D, Lindquist R, Millward JM, Bock M, Pollok K, Mothes R, Viohl L, Radbruch M, Gerhard J, Bellmann-Strobl J, Behrens J, Infante-Duarte C, Mähler A, Boschmann M, Rinnenthal JL, Füchtemeier M, Herz J, Pache FC, Bardua M, Priller J, Hauser AE, Paul F, Niesner R, Radbruch H. Tracking CNS and systemic sources of oxidative stress during the course of chronic neuroinflammation. *Acta Neuropathol*. 2015;130(6):799-814.
103. Radbruch H, Bremer D, Guenther R, Cseresnyes Z, Lindquist R, Hauser AE, Niesner R. Ongoing Oxidative Stress Causes Subclinical Neuronal Dysfunction in the Recovery Phase of EAE. *Front Immunol*. 2016;7:92.
104. Ohl K, Tenbrock K, Kipp M. Oxidative stress in multiple sclerosis: Central and peripheral mode of action. *Exp Neurol*. 2016;277:58-67.
105. Stephenson EL, Mishra MK, Moussienko D, Laflamme N, Rivest S, Ling CC, Yong VW. Chondroitin sulfate proteoglycans as novel drivers of leucocyte infiltration in multiple sclerosis. *Brain*. 2018;141(4):1094-110.
106. Ponta H, Sherman L, Herrlich PA. CD44: from adhesion molecules to signalling regulators. *Nat Rev Mol Cell Biol*. 2003;4(1):33-45.
107. Noble PW. Hyaluronan and its catabolic products in tissue injury and repair. *Matrix Biol*. 2002;21(1):25-9.
108. Scheibner KA, Lutz MA, Boodoo S, Fenton MJ, Powell JD, Horton MR. Hyaluronan fragments act as an endogenous danger signal by engaging TLR2. *J Immunol*. 2006;177(2):1272-81.
109. Collins SL, Black KE, Chan-Li Y, Ahn YH, Cole PA, Powell JD, Horton MR. Hyaluronan fragments promote inflammation by down-regulating the anti-inflammatory A2a receptor. *Am J Respir Cell Mol Biol*. 2011;45(4):675-83.
110. Soilu-Hänninen M, Laaksonen M, Hänninen A. Hyaluronate receptor (CD44) and integrin $\alpha 4$ (CD49d) are up-regulated on T cells during MS relapses. *J Neuroimmunol*. 2005;166(1-2):189-92.
111. Winkler CW, Foster SC, Matsumoto SG, Preston MA, Xing R, Bebo BF, Banine F, Berny-Lang MA, Itakura A, McCarty OJ, Sherman LS. Hyaluronan anchored to activated CD44 on central nervous system vascular endothelial cells promotes

- lymphocyte extravasation in experimental autoimmune encephalomyelitis. *J Biol Chem.* 2012;287(40):33237-51.
112. Rauch U. Extracellular matrix components associated with remodeling processes in brain. *Cell Mol Life Sci.* 2004;61(16):2031-45.
 113. Choi SC, Yoo MA, Lee SY, Lee HJ, Son DH, Jung J, Noh I, Kim CW. Modulation of biomechanical properties of hyaluronic acid hydrogels by crosslinking agents. *J Biomed Mater Res A.* 2015;103(9):3072-80.
 114. Yang YL, Sun C, Wilhelm ME, Fox LJ, Zhu J, Kaufman LJ. Influence of chondroitin sulfate and hyaluronic acid on structure, mechanical properties, and glioma invasion of collagen I gels. *Biomaterials.* 2011;32(31):7932-40.
 115. Tapper EB, Loomba R. Noninvasive imaging biomarker assessment of liver fibrosis by elastography in NAFLD. *Nat Rev Gastroenterol Hepatol.* 2018;15(5):274-82.
 116. Hiscox LV, Johnson CL, Barnhill E, McGarry MD, Huston J, van Beek EJ, Starr JM, Roberts N. Magnetic resonance elastography (MRE) of the human brain: technique, findings and clinical applications. *Phys Med Biol.* 2016;61(24):R401-r37.
 117. Wells RG. Tissue mechanics and fibrosis. *Biochim Biophys Acta.* 2013;1832(7):884-90.
 118. Lau LW, Cua R, Keough MB, Haylock-Jacobs S, Yong VW. Pathophysiology of the brain extracellular matrix: a new target for remyelination. *Nat Rev Neurosci.* 2013;14(10):722-9.
 119. Lohmeier J, Silva RV, Tietze A, Taupitz M, Kaneko T, Prüss H, Paul F, Infante-Duarte C, Hamm B, Caravan P, Makowski MR. Fibrin-targeting molecular MRI in inflammatory CNS disorders. *Eur J Nucl Med Mol Imaging.* 2022;49(11):3692-704.

Statutory Declaration

“I, Rafaela Vieira da Silva, by personally signing this document in lieu of an oath, hereby affirm that I prepared the submitted dissertation on the topic “Investigation of brain extracellular matrix and application of experimental MRI to understand disease development in a murine model of multiple sclerosis” (Untersuchung der extrazellulären Matrix des Gehirns und Anwendung experimenteller MRT zum Verständnis der Krankheitsentwicklung in einem Mausmodell der Multiplen Sklerose), independently and without the support of third parties, and that I used no other sources and aids than those stated.

All parts which are based on the publications or presentations of other authors, either in letter or in spirit, are specified as such in accordance with the citing guidelines. The sections on methodology (in particular regarding practical work, laboratory regulations, statistical processing) and results (in particular regarding figures, charts and tables) are exclusively my responsibility.

Furthermore, I declare that I have correctly marked all of the data, the analyses, and the conclusions generated from data obtained in collaboration with other persons, and that I have correctly marked my own contribution and the contributions of other persons (cf. declaration of contribution). I have correctly marked all texts or parts of texts that were generated in collaboration with other persons.

My contributions to any publications to this dissertation correspond to those stated in the below joint declaration made together with the supervisor. All publications created within the scope of the dissertation comply with the guidelines of the ICMJE (International Committee of Medical Journal Editors; <http://www.icmje.org>) on authorship. In addition, I declare that I shall comply with the regulations of Charité – Universitätsmedizin Berlin on ensuring good scientific practice.

I declare that I have not yet submitted this dissertation in identical or similar form to another Faculty.

The significance of this statutory declaration and the consequences of a false statutory declaration under criminal law (Sections 156, 161 of the German Criminal Code) are known to me.”

Date

Signature

Declaration of your own contribution to the publications

Rafaela Vieira da Silva contributed the following to the below listed publications:

Publication 1: Silva, R. V., Morr, A. S., Mueller, S., Koch, S. P., Boehm-Sturm, P., Rodriguez-Sillke, Y., Kunkel, D., Tzschätzsch, H., Kühn, A. A., Schnorr, J., Taupitz, M., Sack, I., & Infante-Duarte, C., Contribution of Tissue Inflammation and Blood-Brain Barrier Disruption to Brain Softening in a Mouse Model of Multiple Sclerosis, *Frontiers in neuroscience*, 2021.

Contribution: I contributed to the study design together with Anna Morr and Carmen Infante Duarte. For *in vivo* experiments, I conducted the induction of the EAE model. For MRE, Eu-VSOP, and Gadolinium data, I performed all *in vivo* imaging experiments, analyzed the imaging data and applied statistical analysis together with Anna Morr. Tissue processing and preparation for IMC, including antibody tagging, were conducted by Anna Morr and I. Manuscript writing with the exception of the methodological description of the IMC, preparation of all figures, as well as the peer-review process were conducted by me and Anna Morr with the supervision of Carmen Infante Duarte and Ingolf Sack.

Publication 2: Batzdorf, C. S., Morr, A. S., Bertalan, G., Sack, I., Silva, R. V., & Infante-Duarte, C., Sexual Dimorphism in Extracellular Matrix Composition and Viscoelasticity of the Healthy and Inflamed Mouse Brain, *Biology*, 2022.

Contribution: I designed and supervised the study together with Carmen Infante Duarte as co-senior author. I conducted the induction of the EAE model. *In vivo* MRE and tissue collection and preparation were conducted by Clara Batzdorf, Anna Morr and me. I assisted Clara Batzdorf with manuscript writing, me and Carmen Infante Duarte revised and approved the final version, and, together with Clara Batzdorf and Carmen Infante Duarte, I mediated the correspondence in the peer-review process.

Publication 3: Silva, R. V., Biskup, K., Zabala-Jouvin, J. K.; Batzdorf, C. S., Stellmach, C., Morr, A. S., Sack, I., Ludwig, A., Blanchard, V., & Infante-Duarte, C., Brain inflammation induces alterations in glycosaminoglycan metabolism and subsequent changes in CS-4S and hyaluronic acid, *International journal of biological macromolecules*, 2023.

Contribution: I conceptualized and designed the study together with Carmen Infante Duarte. I induced the EAE model and performed tissue collection, qPCR analysis, and histological staining. Together with Karina Biskup, Jessica F. Jouvin-Zabala and Caroline Stellmach, I performed the isolation and labeling of GAGs. I analyzed and applied statistical tests to gene expression and GAGs data. The manuscript and its figures

were prepared by me. I corresponded with the editor and reviewers during the peer-review processed with the supervision of Carmen Infante Duarte, Karina Biskup and Véronique Blanchard.

Signature, date and stamp of first supervising university professor / lecturer

Signature of doctoral candidate

Publication 1: Contribution of Tissue Inflammation and Blood-Brain Barrier Disruption to Brain Softening in a Mouse Model of Multiple Sclerosis

Journal Data Filtered By: **Selected JCR Year: 2019** Selected Editions: SCIE,SSCI
 Selected Categories: **"NEUROSCIENCES"** Selected Category Scheme: WoS
Gesamtanzahl: 271 Journale

Rank	Full Journal Title	Total Cites	Journal Impact Factor	Eigenfactor Score
1	NATURE REVIEWS NEUROSCIENCE	42,809	33.654	0.055400
2	NATURE NEUROSCIENCE	62,933	20.071	0.144390
3	BEHAVIORAL AND BRAIN SCIENCES	9,395	17.333	0.008170
4	TRENDS IN COGNITIVE SCIENCES	27,705	15.218	0.036050
5	JOURNAL OF PINEAL RESEARCH	10,537	14.528	0.009430
6	NEURON	95,056	14.415	0.199640
7	ACTA NEUROPATHOLOGICA	21,908	14.251	0.040740
8	TRENDS IN NEUROSCIENCES	20,011	12.891	0.021220
9	Annual Review of Neuroscience	13,215	12.547	0.012740
10	MOLECULAR PSYCHIATRY	22,227	12.384	0.054730
11	Nature Human Behaviour	2,457	12.282	0.014190
12	BIOLOGICAL PSYCHIATRY	44,016	12.095	0.053910
13	BRAIN	53,282	11.337	0.067050
14	SLEEP MEDICINE REVIEWS	8,077	9.613	0.013000
15	Molecular Neurodegeneration	4,933	9.599	0.011840
16	PROGRESS IN NEUROBIOLOGY	12,791	9.371	0.011250
17	FRONTIERS IN NEUROENDOCRINOLOGY	4,491	9.059	0.007050
18	ANNALS OF NEUROLOGY	37,304	9.037	0.044120
19	NEUROSCIENCE AND BIOBEHAVIORAL REVIEWS	28,873	8.330	0.051900
20	Neurology-Neuroimmunology & Neuroinflammation	2,232	7.724	0.008400
21	NEUROPATHOLOGY AND APPLIED NEUROBIOLOGY	3,992	7.500	0.005960

Rank	Full Journal Title	Total Cites	Journal Impact Factor	Eigenfactor Score
22	Neurobiology of Stress	1,055	7.197	0.003840
23	NEUROPSYCHOPHARMACOLOGY	26,281	6.751	0.040680
24	npj Parkinsons Disease	662	6.750	0.002500
25	BRAIN BEHAVIOR AND IMMUNITY	16,285	6.633	0.028560
26	Brain Stimulation	6,537	6.565	0.015580
27	NEUROSCIENTIST	5,188	6.500	0.007220
28	Acta Neuropathologica Communications	4,070	6.270	0.014730
29	CURRENT OPINION IN NEUROBIOLOGY	14,959	6.267	0.028730
30	Alzheimers Research & Therapy	3,876	6.116	0.011650
31	Neurotherapeutics	4,998	6.035	0.009520
32	GLIA	14,220	5.984	0.017250
33	NEUROIMAGE	102,632	5.902	0.125360
34	Annual Review of Vision Science	601	5.897	0.003700
35	Molecular Autism	2,510	5.869	0.007450
36	Journal of Neuroinflammation	13,709	5.793	0.025870
37	Translational Stroke Research	2,274	5.780	0.004520
38	JOURNAL OF CEREBRAL BLOOD FLOW AND METABOLISM	19,492	5.681	0.024230
39	JOURNAL OF NEUROSCIENCE	167,114	5.673	0.181170
40	BRAIN PATHOLOGY	5,308	5.568	0.007020
41	Translational Neurodegeneration	1,030	5.551	0.002790
42	NEURAL NETWORKS	14,065	5.535	0.018910
43	PAIN	37,753	5.483	0.035730

Rank	Full Journal Title	Total Cites	Journal Impact Factor	Eigenfactor Score
44	Multiple Sclerosis Journal	11,792	5.412	0.019460
45	BIPOLAR DISORDERS	4,838	5.410	0.006610
46	Dialogues in Clinical Neuroscience	3,842	5.397	0.005280
47	Biological Psychiatry-Cognitive Neuroscience and Neuroimaging	1,361	5.335	0.005880
48	NEUROBIOLOGY OF DISEASE	17,200	5.332	0.023770
49	Brain Connectivity	2,431	5.263	0.005180
50	Journal of Parkinsons Disease	2,244	5.178	0.005810
51	CEREBRAL CORTEX	30,815	5.043	0.056030
52	Developmental Cognitive Neuroscience	3,177	4.966	0.010180
53	CEPHALALGIA	11,053	4.868	0.011970
54	NEUROPSYCHOLOGY REVIEW	3,114	4.840	0.004050
55	SLEEP	22,296	4.805	0.024610
56	JOURNAL OF HEADACHE AND PAIN	3,898	4.797	0.007600
57	PSYCHONEUROENDOCRINOLOGY	19,287	4.732	0.027100
58	JOURNAL OF NEUROSCIENCE RESEARCH	13,098	4.699	0.010490
59	EXPERIMENTAL NEUROLOGY	20,154	4.691	0.020070
60	Molecular Brain	2,785	4.686	0.006510
61	Current Neuropharmacology	4,178	4.668	0.006280
62	JOURNAL OF PAIN	10,887	4.621	0.015040
63	JOURNAL OF PHYSIOLOGY-LONDON	50,045	4.547	0.037090
64	EUROPEAN JOURNAL OF NEUROLOGY	11,015	4.516	0.017330
65	MOLECULAR NEUROBIOLOGY	15,297	4.500	0.031350

Rank	Full Journal Title	Total Cites	Journal Impact Factor	Eigenfactor Score
66	ACS Chemical Neuroscience	6,881	4.486	0.015300
67	Fluids and Barriers of the CNS	1,331	4.470	0.002240
68	NEUROPHARMACOLOGY	21,682	4.431	0.033110
69	HUMAN BRAIN MAPPING	23,094	4.421	0.042760
70	JOURNAL OF PSYCHIATRY & NEUROSCIENCE	3,297	4.382	0.004290
71	Current Neurology and Neuroscience Reports	3,429	4.376	0.006810
72	Nature and Science of Sleep	728	4.375	0.001970
73	Frontiers in Aging Neuroscience	9,063	4.362	0.026120
74	PROGRESS IN NEURO-PSYCHOPHARMACOLOGY & BIOLOGICAL PSYCHIATRY	11,179	4.361	0.013670
75	NEUROBIOLOGY OF AGING	23,002	4.347	0.032570
76	INTERNATIONAL JOURNAL OF NEUROPSYCHOPHARMACOLOGY	6,749	4.333	0.011150
77	Neuroscience Bulletin	2,338	4.326	0.004870
78	NEUROENDOCRINOLOGY	4,958	4.271	0.004820
79	CURRENT OPINION IN NEUROLOGY	5,437	4.207	0.008280
80	ASN Neuro	984	4.167	0.001580
81	Journal of Neural Engineering	7,240	4.141	0.011940
82	Journal of Neuroimmune Pharmacology	2,809	4.113	0.003520
83	CNS Neuroscience & Therapeutics	3,598	4.074	0.005870
84	JOURNAL OF NEUROCHEMISTRY	34,378	4.066	0.021840
85	Frontiers in Molecular Neuroscience	6,721	4.057	0.020190
86	NUTRITIONAL NEUROSCIENCE	2,110	4.028	0.002640
87	CORTEX	10,979	4.009	0.022870

Rank	Full Journal Title	Total Cites	Journal Impact Factor	Eigenfactor Score
88	Current Opinion in Behavioral Sciences	2,507	3.990	0.012580
89	Developmental Neurobiology	3,049	3.935	0.006120
90	Cognitive Neurodynamics	988	3.925	0.001690
91	Frontiers in Cellular Neuroscience	11,389	3.921	0.034000
92	JOURNAL OF ALZHEIMERS DISEASE	23,214	3.909	0.048080
93	NEUROCHEMISTRY INTERNATIONAL	8,928	3.881	0.008010
94	EUROPEAN NEUROPSYCHOPHARMACOLOGY	7,597	3.853	0.013120
95	JOURNAL OF NEUROTRAUMA	15,388	3.793	0.021530
96	Frontiers in Neuroscience	17,395	3.707	0.049650
97	HEARING RESEARCH	11,072	3.693	0.012480
98	PSYCHOPHYSIOLOGY	14,586	3.692	0.012670
99	Annals of Clinical and Translational Neurology	2,571	3.660	0.011170
100	JOURNAL OF SLEEP RESEARCH	5,945	3.623	0.007370
101	CELLULAR AND MOLECULAR NEUROBIOLOGY	4,732	3.606	0.006190
102	Social Cognitive and Affective Neuroscience	7,347	3.571	0.019570
103	eNeuro	3,237	3.544	0.015940
104	Journal of NeuroEngineering and Rehabilitation	5,164	3.519	0.008430
105	JOURNAL OF NEURAL TRANSMISSION	7,111	3.505	0.007930
106	EUROPEAN JOURNAL OF PAIN	7,579	3.492	0.009730
107	Journal of Neurodevelopmental Disorders	1,342	3.487	0.003300
108	HIPPOCAMPUS	8,587	3.404	0.010830
109	GENES BRAIN AND BEHAVIOR	3,639	3.397	0.005080



Contribution of Tissue Inflammation and Blood-Brain Barrier Disruption to Brain Softening in a Mouse Model of Multiple Sclerosis

Rafaela Vieira Silva^{1,2†}, Anna S. Morr^{3†}, Susanne Mueller^{4,5}, Stefan Paul Koch^{4,5}, Philipp Boehm-Sturm^{4,5}, Yasmina Rodriguez-Silke⁶, Désirée Kunkel⁶, Heiko Tzschätzsch³, Anja A. Kühl⁷, Jörg Schnorr³, Matthias Taupitz³, Ingolf Sack^{3†} and Carmen Infante-Duarte^{1,2,8*†}

OPEN ACCESS

Edited by:

Nathalie Just,
INRA Centre Val de Loire, France

Reviewed by:

Emmanuelle Canet Soulas,
Université Claude Bernard Lyon 1,
France
Max Masthoff,
University Hospital Münster, Germany

*Correspondence:

Carmen Infante-Duarte
carmen.infante@charite.de

[†]These authors have contributed
equally to this work and share first
authorship

[‡]These authors have contributed
equally to this work and share senior
authorship

Specialty section:

This article was submitted to
Brain Imaging Methods,
a section of the journal
Frontiers in Neuroscience

Received: 27 April 2021

Accepted: 19 July 2021

Published: 23 August 2021

Citation:

Silva RV, Morr AS, Mueller S,
Koch SP, Boehm-Sturm P,
Rodriguez-Silke Y, Kunkel D,
Tzschätzsch H, Kühl AA, Schnorr J,
Taupitz M, Sack I and
Infante-Duarte C (2021) Contribution
of Tissue Inflammation
and Blood-Brain Barrier Disruption
to Brain Softening in a Mouse Model
of Multiple Sclerosis.
Front. Neurosci. 15:701308.
doi: 10.3389/fnins.2021.701308

¹ Charité - Universitätsmedizin Berlin, Corporate Member of Freie Universität Berlin and Humboldt-Universität zu Berlin, Institute of Medical Immunology, Berlin, Germany, ² Charité - Universitätsmedizin Berlin, Einstein Center for Neurosciences Berlin, Berlin, Germany, ³ Charité - Universitätsmedizin Berlin, Corporate Member of Freie Universität Berlin and Humboldt-Universität zu Berlin, Department of Radiology, Berlin, Germany, ⁴ Charité - Universitätsmedizin Berlin, Corporate Member of Freie Universität Berlin and Humboldt-Universität zu Berlin, Department of Experimental Neurology and Center for Stroke Research, Berlin, Germany, ⁵ Charité - Universitätsmedizin Berlin, NeuroCure Cluster of Excellence and Charité Core Facility 7T Experimental MRIs, Berlin, Germany, ⁶ Berlin Institute of Health at Charité - Universitätsmedizin Berlin, Flow & Mass Cytometry Core Facility, Berlin, Germany, ⁷ Charité - Universitätsmedizin Berlin, Corporate Member of Freie Universität Berlin and Humboldt-Universität zu Berlin, Berlin, Germany, ⁸ Charité - Universitätsmedizin Berlin, Corporate Member of Freie Universität Berlin and Humboldt-Universität zu Berlin, ECRC Experimental and Clinical Research Center, Berlin, Germany

Neuroinflammatory processes occurring during multiple sclerosis cause disseminated softening of brain tissue, as quantified by *in vivo* magnetic resonance elastography (MRE). However, inflammation-mediated tissue alterations underlying the mechanical integrity of the brain remain unclear. We previously showed that blood-brain barrier (BBB) disruption visualized by MRI using gadolinium-based contrast agent (GBCA) does not correlate with tissue softening in active experimental autoimmune encephalomyelitis (EAE). However, it is unknown how confined BBB changes and other inflammatory processes may determine local elasticity changes. Therefore, we aim to elucidate which inflammatory hallmarks are determinant for local viscoelastic changes observed in EAE brains. Hence, novel multifrequency MRE was applied in combination with GBCA-based MRI or very small superparamagnetic iron oxide particles (VSOPs) in female SJL mice with induced adoptive transfer EAE ($n = 21$). VSOPs were doped with europium (Eu-VSOPs) to facilitate the *post-mortem* analysis. Accumulation of Eu-VSOPs, which was previously demonstrated to be sensitive to immune cell infiltration and ECM remodeling, was also found to be independent of GBCA enhancement. Following registration to a reference brain atlas, viscoelastic properties of the whole brain and areas visualized by either Gd or VSOP were quantified. MRE revealed marked disseminated softening across the whole brain in mice with established EAE (baseline: 3.1 ± 0.1 m/s vs. EAE: 2.9 ± 0.2 m/s, $p < 0.0001$). A similar degree of softening was observed in sites of GBCA enhancement i.e., mainly within cerebral cortex and brain stem (baseline: 3.3 ± 0.4 m/s vs. EAE: 3.0 ± 0.5 m/s, $p = 0.018$).

However, locations in which only Eu-VSOP accumulated, mainly in fiber tracts (baseline: 3.0 ± 0.4 m/s vs. EAE: 2.6 ± 0.5 m/s, $p = 0.023$), softening was more pronounced when compared to non-hypointense areas (percent change of stiffness for Eu-VSOP accumulation: $-16.81 \pm 16.49\%$ vs. for non-hypointense regions: $-5.85 \pm 3.81\%$, $p = 0.048$). Our findings suggest that multifrequency MRE is sensitive to differentiate between local inflammatory processes with a strong immune cell infiltrate that lead to VSOP accumulation, from disseminated inflammation and BBB leakage visualized by GBCA. These pathological events visualized by Eu-VSOP MRI and MRE may include gliosis, macrophage infiltration, alterations of endothelial matrix components, and/or extracellular matrix remodeling. MRE may therefore represent a promising imaging tool for non-invasive clinical assessment of different pathological aspects of neuroinflammation.

Keywords: magnetic resonance elastography, Eu-VSOP, gadolinium, neuroinflammation, experimental autoimmune encephalomyelitis, BBB disruption, multiple sclerosis

INTRODUCTION

Multiple sclerosis (MS) is a chronic autoimmune disease in which myelin-autoreactive immune cells gain access to the central nervous system (CNS) *via* the blood-brain barrier (BBB) and the blood-cerebrospinal fluid barrier (Alvarez et al., 2011). This infiltration results in the formation of multiple focal lesions that involve both white and gray matter and contribute to demyelination and neurodegeneration. Demyelinating plaques are seen as hyperintense areas by T2-weighted magnetic resonance imaging (MRI), whereas inflammation-associated BBB leakage is revealed by hyperintensity in contrast agent-based T1-weighted images (Thompson et al., 2018).

Due to their intrinsic magnetic properties, gadolinium-based contrast agents (GBCAs) have long been used as contrast agents for MRI. GBCAs induce signal changes in T2, T2* and T1-weighted MRI by affecting the relaxation time of water protons in biological tissues. The appearance of hyperintense widespread Gd-enhanced areas has become the standard MRI marker of loss of BBB integrity on T1-weighted MRI. Because BBB leakage was found to predict the formation of new non-focal white matter lesions, GBCA enhancement reflecting inflammatory activity is widely used in MS diagnosis (Lassmann, 2008; Zéphir, 2018). However, studies on the potential accumulation of Gd into the tissue, including the CNS, after repeated administration of GBCAs, in particular linear GBCAs, raised concerns about their safety (Layne et al., 2018). Furthermore, a discrepancy between the presence of Gd-enhancing lesions and clinical manifestations in both, MS and its animal model, the experimental autoimmune encephalomyelitis (EAE), has been reported (Lassmann, 2008) (Wuerfel et al., 2007, 2010; Tysiak et al., 2009; Wang et al., 2019). This discrepancy, referred to as a clinical-radiological paradox, motivates the quest for reliable imaging tools in neuroinflammation.

An evolving imaging strategy for visualizing neuroinflammation is based on the application of very small iron oxide particles (VSOPs) (Tysiak et al., 2009; Millward et al., 2013). VSOPs have a hydrodynamic diameter of only 7 nm and

are stabilized with a citrate coating (Taupitz et al., 2000; Wagner et al., 2002). The iron causes strong susceptibility changes, which give rise to hypointense areas in T1-, T2- and T2*-weighted MR images, but appears to be best visualized by T2*-weighted MRI (Tysiak et al., 2009; Millward et al., 2013, 2019). Previous work in EAE has demonstrated that VSOPs administered *in vivo* intravenously can be phagocytosed locally or transported within cells to areas of inflammation and/or appear freely diffused in the brain parenchyma or bound to endothelial cells (Tysiak et al., 2009; Millward et al., 2013, 2019; Berndt et al., 2017). Therefore, VSOPs do not only visualize BBB breakdown in areas of Gd-enhancement but additionally detect other inflammatory mechanisms that were not detected by conventional GBCA-enhanced MRI, such as myeloid cell infiltrates, changes in the extracellular matrix (ECM) or alteration of the endothelial glycocalyx (Tysiak et al., 2009; Millward et al., 2013, 2019; Berndt et al., 2017).

At the same time, magnetic resonance elastography (MRE) (Muthupillai et al., 1995) has evolved as a non-invasive tool for detecting inflammation-associated pathologies (Muthupillai et al., 1995; Plewes et al., 1995; Schregel et al., 2012; Hiscox et al., 2016). It is already well documented that neuroinflammation modifies the viscoelastic properties of neuronal tissue, reducing stiffness throughout larger brain areas (Wuerfel et al., 2010; Streitberger et al., 2012) (Riek et al., 2012; Millward et al., 2015; Fehlner et al., 2016; Wang et al., 2020). MRE uses harmonic vibrations to transmit shear waves into the tissue of interest (Manduca et al., 2021). Wave propagation is detected using motion-sensitive MRI, from which viscoelastic parameters such as stiffness (magnitude shear modulus or shear wave speed) and fluidity (viscosity, dispersion angle or loss angle of the shear modulus) are derived (Hirsch et al., 2017). We previously demonstrated in the active EAE model that MRE does not appear to correlate with GBCA enhancement in MRI. However, in this study, we could not provide an accurate regional analysis due to the limitation of the MRE tools (Wang et al., 2020). The recent development of multifrequency MRE with tomoelastography postprocessing in small animal models fosters high-resolution

MRE of the mouse brain with multiple imaging slices that reveal deeper anatomical details (Bertalan et al., 2019), enabling a more accurate investigation of the mechanisms underlying brain softening in inflamed areas.

Therefore, in this study, we aimed at uncovering how neuroinflammatory processes such as blood-brain barrier leakage and focal inflammation are associated with changes in the mechanical properties detected by multifrequency MRE. To optimize the study, here we use a model of adoptive transfer EAE, which contrary to the active EAE used in Wang et al., 2020 (Wang et al., 2020) develops numerous and large brain lesions. We hypothesize that novel tomoelastography sensitively detects mechanical changes in sites of intense neuroinflammation that are revealed by VSOP-deposits. Those sites are known to be characterized by enhanced myeloid cell activity (Millward et al., 2013), alterations of the glycocalyx on barrier cells (Berndt et al., 2017) and ECM remodeling (Wang et al., 2020). To test our hypothesis, we combined *in vivo* viscoelasticity measured by multifrequency MRE with both, GBCA- and VSOP- MRI, in the adoptive transfer EAE model. We used VSOPs doped with europium (Eu) in order to improve histological detection of the particles in biological tissues, without the interference of endogenous iron (de Schellenberger et al., 2017).

MATERIALS AND METHODS

Animals and Adoptive Transfer EAE Induction

All animal experiments were conducted in accordance with national and institutional guidelines for the care and use of laboratory animals and with directive 2010/63/EU of the European Parliament and of the Council of 22 September 2010 and were approved by the Berlin State Office for Health and Social Affairs (LAGeSo, registration number G106/19).

Adoptive transfer EAE was induced by transfer of myelin proteolipid protein (PLP)-reactive lymphocytes into two cohorts of adult female SJL mice, 9–12 weeks old ($n = 21$ mice in total; Janvier, SAS, France). EAE is more effectively induced in females than in male animals (Miller and Karpus, 2007), therefore in all our previous studies and also in this study we included only female mice in the experiments. To obtain PLP-reactive lymphocytes, a donor group of mice ($n = 22$) was actively immunized with 200 μg of the myelin peptide PLP139-151 emulsified with 200 μl complete Freund's adjuvant (Thermo Fischer Scientific, United States) and 800 μg Mycobacterium tuberculosis H37Ra (Difco, United States) as previously described (Millward et al., 2013). Additionally, 250 ng pertussis toxin (List Biological Laboratories, United States) was injected intraperitoneally on days 0 and 2. On day 10 post-immunization, animals were sacrificed, inguinal and axillary lymph nodes were collected, and the cells were cultured as previously described (Pleues et al., 1995). After 4 days in culture with RPMI 1640 medium (supplemented with 2 mM L-glutamine, 100 units/ml penicillin, 100 $\mu\text{g}/\text{ml}$ streptomycin and 10% fetal bovine serum) (Gibco, Thermo Fischer Scientific) containing 12.5 $\mu\text{g}/\text{ml}$ PLP, lymph node cells were harvested, and 30 million cells were

injected intraperitoneally into each recipient mouse. After immunization, mice were monitored daily for signs of disease, which were scored as follows: 0—no sign, 0.5—tail paresis, 1—tail paresis and/or plegia and righting reflex weakness; 2—hind limb paresis; 3—paraplegia; 4—paraplegia with forelimb weakness or paralysis; 5—moribund or dead animal. To comply with animal welfare guidelines, all mice with a score greater than 3 or with atypical signs of EAE were euthanized and removed from the study before the second T2*-weighted MRI ($n = 8$).

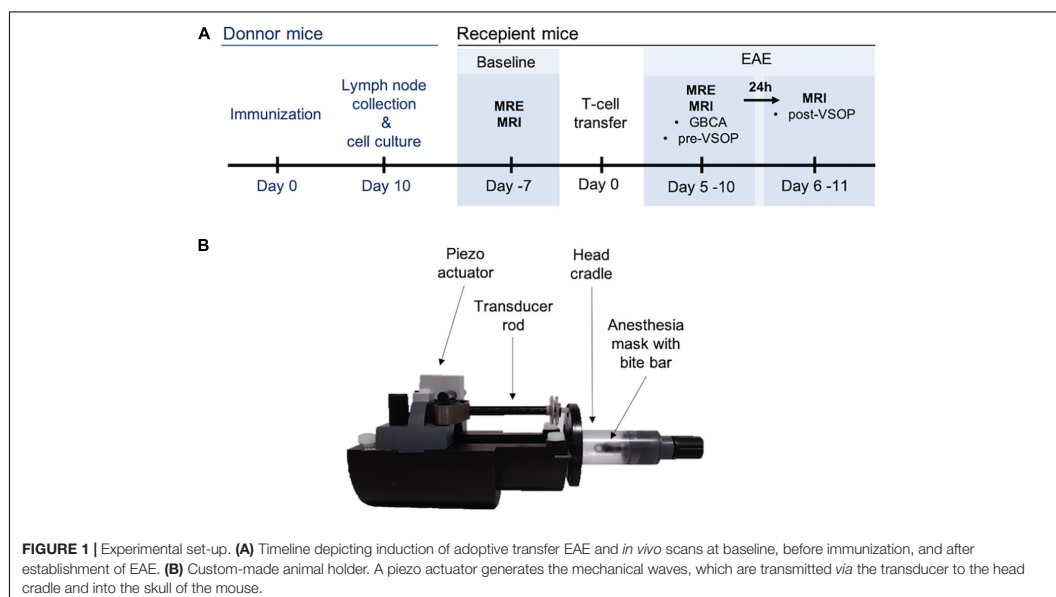
In vivo Scans and Experimental Set-Up

In vivo scans were performed at two timepoints, prior to EAE induction (baseline control) and after EAE signs were established, i.e., animals showed at least partial hind limb paresis (score 1.75) (Figure 1A). For each single animal, EAE scan was compared to the corresponding baseline scan, while imaging post-contrast was compared to the corresponding pre-contrast image. In EAE animals, MRE was first performed followed by pre-contrast MRI with a T1-weighted imaging, a T2-weighted sequence to acquire an anatomical image, and a pre-contrast T2*-weighted sequence. Thereafter, GBCA (0.2 mmol/kg, Magnevist, Bayer-Schering AG) was administered *via* the tail vein, and post-contrast T1-weighted images were acquired. At the end of the scans, 0.2 mmol/kg Eu-VSOPs [batch RH030812 Eu-R; $c(\text{Fe}) = 0.134 \text{ mol/L}$] were intravenously injected into the tail vein, and 24 h later, a T2*-weighted sequence was acquired to visualize particle accumulation. The applied Eu-VSOP and Magnevist doses as well as the time between injections and scans were defined based on our previous studies (Wuerfel et al., 2007; Tysiak et al., 2009; Millward et al., 2013, 2019; Wang et al., 2020). No GBCA or Eu-VSOPs were administered at baseline. Eu-VSOPs were produced and provided by the Experimental Radiology working group of the Department of Radiology, Charité - Universitätsmedizin Berlin as described previously (de Schellenberger et al., 2017).

MRI and MRE examinations were performed in a preclinical 7 Tesla MRI scanner (BioSpec, Bruker, Ettlingen, Germany) running with ParaVision 6.1 software. All scans were acquired with a 20-mm diameter 1H-RF quadrature volume coil (RAPID Biomedical, Würzburg, Germany). For acquisitions, mice were placed on a custom-built animal holder (Figure 1B) and anesthetized with 1.5–2.0% isoflurane in 30% O₂ and 70% N₂O administered *via* an anesthesia mask during continuous respiratory monitoring using a pressure-sensitive pad placed on the thorax (Small Animal Instruments Inc., Stony Brook, NY, United States). Body temperature was kept constant by circulating water through warming pads integrated into the animal holder, and body temperature was monitored using a rectal probe.

MRI

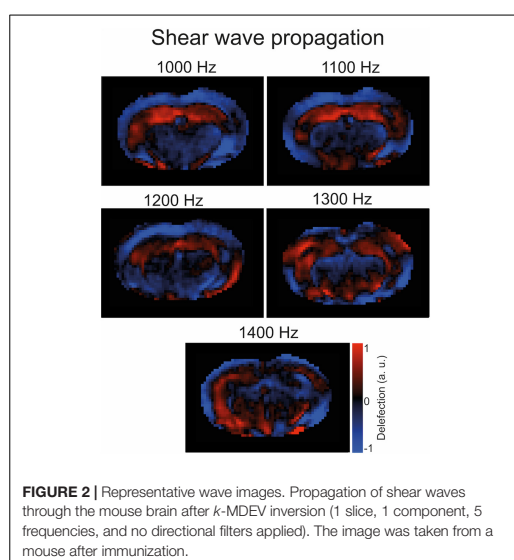
Coronal anatomical images were acquired using a T2-weighted 2D-RARE sequence with repetition time (TR) = 3,500 ms, effective echo time (TE) = 33 ms, echo spacing (DTE) = 11 ms, RARE factor = 8, 4 averages, 32 contiguous slices with a slice thickness of 0.5 mm, field of view (FOV) = 18 mm × 18 mm, matrix size MTX = 180 × 180, in-plane resolution



0.1 mm × 0.1 mm × 0.5 mm, bandwidth BW = 34,722 Hz, and total acquisition time TA = 5:08 min). GBCA-enhanced images were acquired using a T1-weighted RARE sequence with TR = 800 ms, TE = 6.5 ms, (DTE) = 6.5 ms, RARE factor = 2, 6 averages, BW = 75,000 Hz, and the same geometry as for the T2w scan resulting in a total acquisition time of TA = 7:12 min. To visualize Eu-VSOP accumulation, a T2*-weighted FLASH sequence was used with TR = 400 ms, TE = 2.5 ms, flip angle = 30 deg, 3 averages, BW = 29,762 Hz, and the same geometry as for the T2w scan with a total acquisition time of TA = 2:24 min.

MRE

To induce shear waves in the mouse brain, vibrations were generated with a custom-made driver system using a non-magnetic piezoceramic actuator. Vibrations were transmitted via a transducer rod to the head cradle and into the skull of the anesthetized and fixated mouse (**Figure 1B**). The MRE technique used in this study has been described in more detail elsewhere (Bertalan et al., 2019). In short, multifrequency MRE was performed, and wave images (**Figure 2**) were acquired using 5 frequencies (1,000, 1,100, 1,200, 1,300, and 1,400 Hz). In the bregma areas -2.84 mm to 0.23 mm, 7 coronal slices with a slice thickness of 0.8 mm and a 0.18 mm × 0.18 mm in-plane resolution were acquired. We limited our analysis to this area for consistency with previous studies using tomoelastography (Bertalan et al., 2019, 2020; Guo et al., 2019), as well as to reduce scan time while focusing on multifrequency studies. Further imaging parameters were: TA = 9 min, TE = 53 ms, TR = 4,000 ms, FOV = 16.2 mm × 10.8 mm, and matrix size = 90 × 60.



For analysis, tomoelastography postprocessing (Tzschätzsch et al., 2016) based on multifrequency wave-number analysis was used to derive shear wave speed (*c* in m/s) as a surrogate marker of stiffness. In addition, Laplacian-based direct multifrequency inversion (Hirsch et al., 2017) was used to recover the phase angle of the complex shear modulus (ϕ in rad, also known as

loss angle) as a measure of the solid-fluid behavior of biological tissues. Averaged c - and ϕ -maps showing the brain area covered by MRE (from bregma -2.84 to 0.23 mm) are provided in **Supplementary Figure 1**.

Data Analysis

Registration to the Allen Brain Atlas

ANTx, a customized MATLAB toolbox (latest version available under ¹), was used for MRI and MRE image registration, as described elsewhere (Koch et al., 2019). In short, for MRI, T2-weighted RARE images, pre- and postcontrast T1-weighted RARE, and T2*-weighted FLASH images were transferred into the Allen mouse brain atlas space (Allen Institute for Brain Science, United States) using ELASTIX ²(Klein et al., 2009). Next, the pre- and postcontrast T1-weighted RARE and the pre- and postcontrast T2*-weighted FLASH images were co-registered and resliced to the T2-weighted RARE image using affine transformation.

For image registration of the MRE parameter maps to the brain atlas, the individual magnitude images and the parameter maps, c and ϕ , were first 3D-coregistered and 2D-slice wise registered to the T2-weighted TurboRARE images using affine non-linear b-spline transformation. Finally, the image transformation found for MRI was used to transform MRE images into the Allen mouse brain atlas space (Guo et al., 2019). All acquired 7 MRE slices were interpolated to 215 slices of the reference atlas, generating approx. 58 corresponding MRE slices. Consequently, all acquired scans were aligned to the Allen mouse brain atlas, making it possible to locate and compare identified areas of Gd-enhancement and Eu-VSOP accumulation between the different imaging modalities.

Generation of Masks

Masks corresponding to areas of Gd-enhancement and Eu-VSOP accumulation were manually drawn on registered postcontrast T1-weighted and T2*-weighted images by two experienced researchers using the ANALYZE 10.0 program (Biomedical Imaging Resources Mayo Clinic). For masks depicting Gd-enhancement, maps showing percentage changes in signal intensity (SI) were calculated by subtracting the postcontrast from the precontrast T1-weighted image using Image J 1.52e (³National Institutes of Health, United States). Eu-VSOP masks were drawn on the postcontrast T2*-weighted images. Then, all masks were registered to the Allen mouse brain atlas using ELASTIX.

As the sites of particle accumulation appear as focal hypointense areas, and the current MRE resolution is 0.18 mm \times 0.18 mm, it was necessary to dilate the Eu-VSOP masks by two pixels using Matlab to reduce effects of single-pixel artifacts [Version 9.7 (R2019b); Natick, Massachusetts: The MathWorks Inc.]. Eu-VSOP areas were excluded from GBCA masks and vice versa in order to obtain masks corresponding

solely to areas with either Gd-enhancement or Eu-VSOP accumulation. Individual ventricle masks, manually drawn on registered MRE magnitude images, were excluded from the GBCA and Eu-VSOP masks to eliminate the ventricles from the maps, as mechanical wave propagation is not ensured in liquid-filled spaces. In order to establish MRE parameter maps of areas with alterations detected exclusively by one of the MRI modalities (either by GBCA or Eu-VSOP), areas marked in both, GBCA-based and Eu-VSOP-based MRI, were disregarded. Mean values for stiffness and fluidity were obtained by overlaying the masks on the MRE parameter maps (c -map and ϕ -map).

Gadolinium-based contrast agent masks generated from percentage change T1-weighted images and Eu-VSOP masks drawn on (unregistered) T2*-weighted images were used to create incidence maps using the ANTx toolbox in order to illustrate the prevalence of inflammation detected by either GBCA or Eu-VSOPs.

Statistical Analysis

Paired t -tests were applied to shear wave speed (c) and phase angle (ϕ) mean values of mask obtained from the MRE parameter maps using GraphPad Prism 9.0 (GraphPad software, La Jolla, CA, United States). Normality was tested using the D'Agostino-Pearson test. If one of the two compared groups did not pass the normality test, the Wilcoxon matched-pairs signed rank test was used. Differences were considered to be statistically significant for p -values < 0.05 .

Histology and Imaging Mass Cytometry

Imaging Mass CytometryTM (IMC) was used to identify the surroundings of the particles within the inflamed tissue by using lanthanide-tagged antibodies and the Eu incorporated into the nanoparticle cores to label VSOPs. Therefore, after the last MRI scan, animals were sacrificed with an overdose of ketamine/xylazine and immediately transcardially perfused with 4% paraformaldehyde (PFA) (Carl Roth®, Germany). In addition, a healthy mouse without Eu-VSOP administration was used as control. The brains were removed and immersed in 4% PFA for 24 h at 4°C prior to paraffin embedding (ROTI® Plast, Germany). Sequential 4- μ m sections of samples, corresponding to areas with Eu-VSOP accumulation identified by MRI, were cut, heated at 60°C for at least 1 h, and deparaffinized in *m*-xylene overnight (Sigma-Aldrich, Germany) for IMC. Following deparaffinization, the sections were re-hydrated in descending ethanol series (Carl Roth®, Germany). Then, samples were processed according to the IMC staining protocol for FFPE sections [PN 400322 A3, Fluidigm San Francisco, CA, United States(RSY1)]. The antigen retrieval was performed with a citrate buffer (10 mM sodium citrate, 0.05% Tween 20, pH 6) for 20 min at 96°C. After incubation with isotope-tagged antibodies overnight at 4°C, the sections were stained with the CELL-ID Intercalator-Ir (Fluidigm, United States) for 30 min at room temperature, then washed, air-dried and kept at RT until imaging with the Hyperion Imaging System (Fluidigm, United States).

¹<https://github.com/ChariteExpMri/antx2>

²<http://elastix.isi.uu.nl/>

³<https://imagej.nih.gov/ij/>

All antibodies were tagged with a metal isotope using the Maxpar labeling kit according to the manufacturer's instructions (Fluidigm, United States). A complete list of the panel with a description of the antibodies, isotope tags, and dilutions is available in **Supplementary Table 1**. Imaging mass cytometry was performed on a CyTOF2/upgraded to Helios specifications coupled to a Hyperion Tissue Imager (Fluidigm), using CyTOF software version 7.0. Prior to ablation, the instrument was tuned according to the manufacturer's instructions, using the 3-Element Full Coverage Tuning Slide (Fluidigm). The dried slide was loaded into the imaging module and regions of interest were selected for each sample on a preview (panorama). Optimal laser power was determined for each sample to ensure complete ablation of the tissue. Laser ablation was performed at a resolution of 1 μm and a frequency of 200 Hz. Data was stored as MCD files as well as txt files. Original files were opened with MCD viewer (v1.0.560.6), and images were extracted as TIFF files. For visualization, threshold correction was applied to reduce noise followed by post-acquisition processing with ImageJ software (ImageJ 1.48v, United States) using the despeckle and sharpen tools and Gaussian blur filter (kernel width, 0.50 pixels).

RESULTS

GBCA and Eu-VSOP Incidence Maps in Adoptive Transfer EAE

Following transfer of myelin-reactive lymphocytes, all animals showed signs of disease reflecting ascending paralysis. On the first day of imaging after EAE establishment, the mean score was 1.97 (± 0.76 SD) versus 2.83 (± 0.39 SD) on the second day, 24 h after Eu-VSOP injection. According to the animal protocols, 8 animals with atypical signs of EAE or with a score greater than 3 were removed from the study before the second T2*-weighted acquisition.

Incidence maps, as percentage of mice affected, were created to visualize the extent and frequency of inflammatory lesions visualized by each of the two contrast agents. The color scale represents the percentage of animals with a mask in these areas (**Figure 3**). After establishment of the disease, all mice showed Gd- ($n = 19$) and Eu-VSOPs-enhancement ($n = 11$) (bregma coordinates -2.8 to 0.23 mm). Both GBCA and Eu-VSOPs were found throughout the brain. The GBCA-intensity maps, showing large diffuse Gd-enhanced lesions across the brain, indicate that BBB leakage was localized in the same areas among mice, namely near the ventricles. The most affected regions were close to large arteries, such as the left hippocampal artery (bregma coordinate -3.26 mm), present in 80% of the mice (**Figure 3A**). While the cerebellum and brainstem were particularly affected, enhancement was also found in the hippocampus, thalamus, hypothalamus and midbrain. Specifically within the brain area covered by the MRE scan (bregma coordinates -2.84 to 0.23 mm), GBCA-enhancement was detected within the cerebral cortex, cerebral nuclei, brain stem, midbrain and fiber tracts), as shown in details in the **Supplementary Figure 2**. Conversely, Eu-VSOP accumulation was more diffuse with a less predictable pattern, with the highest incidence in the vicinity of the basilar

artery (bregma coordinate -3.26 mm) and the anterior cerebral artery (bregma coordinate -6.76 mm) of about 40% (**Figure 3B**). An overview of the Eu-VSOP distribution across the brain can be found in **Supplementary Figure 3**. Within the brain section covered by MRE, the signal distribution was found spread inside the hippocampus, cerebral nuclei, brain stem, midbrain and fiber tracts. **Table 1** additionally shows the incidence of Gd and Eu-VSOP across the whole brain.

Next, we assessed the global effect of neuroinflammation on viscoelasticity. Therefore, viscoelastic properties of the whole brain, disregarding the ventricles, were measured at baseline and after establishment of EAE symptoms. A significant softening (reduction in stiffness, i.e., decrease in c in m/s) was observed ($p < 0.0001$, baseline 3.15 ± 0.11 m/s vs. EAE 2.89 ± 0.20 m/s, $n = 19$), whereas the fluidity depicted by the loss angle (ϕ in rad) ($p = 0.6070$, baseline 0.69 ± 0.03 m/s vs. EAE 0.70 ± 0.06 m/s, $n = 19$) was unaffected (**Figure 4**).

MRE Detects Tissue Softening in Areas of Gd-Enhancement

To assess the sensitivity of MRE to measure mechanical alterations in areas of BBB leakage detected exclusively by Gd-enhancement, GBCA masks generated from percentage change images calculated from T1-weighted MR images were overlaid on MRE parameter maps (ϕ and c) as illustrated in **Figures 5A,B**.

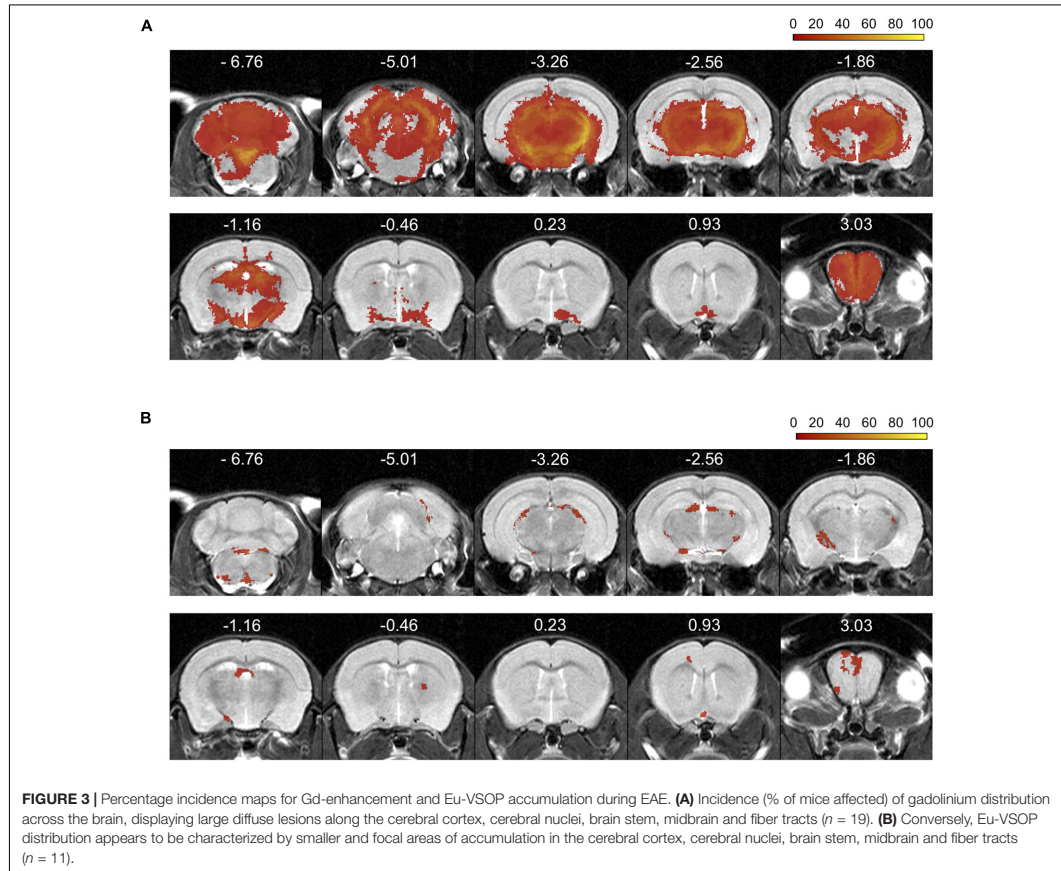
A significant reduction in shear wave speed (c) after EAE establishment was observed compared to baseline ($p = 0.0183$; baseline 3.28 ± 0.38 m/s vs. EAE 2.99 ± 0.51 m/s, $n = 19$), indicating softening of brain tissue, whereas fluidity (phase angle, ϕ) remained unaltered ($p = 0.3683$; baseline 0.85 ± 0.08 rad vs. EAE 0.86 ± 0.09 rad, $n = 19$) (**Figure 5C**).

MRE Detects Marked Tissue Softening in Sites of Eu-VSOP Accumulation

Eight of the 11 mice with Eu-VSOP accumulation showed accumulation in regions covered by the MRE scans (bregma -2.84 to 0.23 mm). The masks solely comprising Eu-VSOP accumulation were overlaid on the MRE parameter maps, c and ϕ , as shown in **Figures 6A,B**. Tomoelastography at baseline and after EAE induction revealed a significant reduction in stiffness (c in m/s) in sites with Eu-VSOP accumulation (within hippocampus, cerebral nuclei, brain stem, midbrain and fiber tracts) ($p = 0.0235$, baseline 3.03 ± 0.39 m/s vs. EAE 2.55 ± 0.47 m/s, $n = 8$); whereas fluidity, depicted by ϕ in rad, was unaffected ($p = 0.1168$, baseline 0.91 ± 0.17 rad vs. EAE 0.87 ± 0.20 rad, $n = 8$) (**Figure 6C**).

Sites of Eu-VSOP Accumulation Display Pronounced Softening Compared to the Overall Brain Alterations

We further investigated whether MRE is sensitive to mechanical changes at sites of inflammation detected by MRI with either GBCA or Eu-VSOPs. For that, the percentage change in stiffness and fluidity in areas with Gd-enhancement or Eu-VSOP accumulation was compared to the rest of the brain (**Figure 7A**). Our analysis revealed no significant difference in the percentage



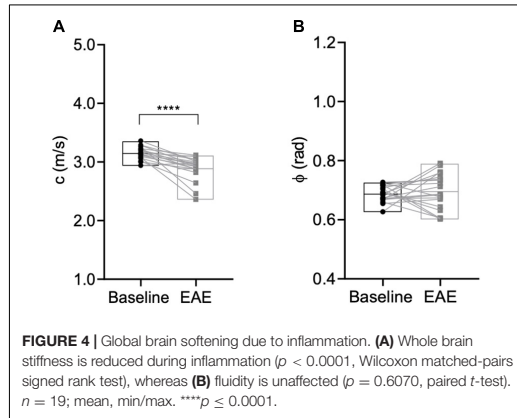
change between sites with Gd-enhancement (within cerebral cortex, cerebral nuclei, brain stem, midbrain and fiber tracts) compared to non-enhancing areas for either stiffness ($p = 0.3321$,

Gd-enhanced areas $-9.76 \pm 13.32\%$ vs. non-enhanced areas $-7.18 \pm 6.21\%$, $n = 19$) or fluidity ($p = 0.1246$, Gd-enhanced areas $4.47 \pm 7.96\%$ vs. rest of the brain $1.07 \pm 10.56\%$, $n = 19$) (**Figure 7B**). However, when we compared the percentage change in stiffness between areas with Eu-VSOP accumulation and those without Eu-VSOP accumulation, we observed a significant difference ($p = 0.0483$, areas with Eu-VSOP accumulation $-16.81 \pm 16.49\%$ vs. areas without accumulation $-5.85 \pm 3.81\%$, $n = 8$) (**Figure 7B**). This effect was also seen for global stiffness after establishment of EAE signs vs. stiffness at sites of Eu-VSOP accumulation ($p = 0.0229$, whole brain 2.93 ± 0.16 m/s vs. Eu-VSOP accumulation 2.55 ± 0.47 m/s, $n = 8$) (**Supplementary Figure 4**). This result indicates that, besides being sensitive to global brain changes, MRE can effectively identify areas affected by inflammatory processes that are detectable by Eu-VSOP accumulation only. Fluidity in these above mentioned locations, however, was unaffected ($p = 0.2889$, areas with Eu-VSOP accumulation $-5.29 \pm 8.33\%$ vs. non-hypointense areas $-2.16 \pm 6.63\%$, $n = 8$) (**Figure 7B**).

TABLE 1 | Incidence of Gd-enhancement and Eu-VSOP accumulation.

Anatomical label	Incidence (%)	
	Gd mask	Eu-VSOP mask
Cerebral cortex	100	72.7
Cerebral nuclei	100	54.5
Brain stem	78.9	90.9
Midbrain	100	63.6
Hindbrain	100	63.6
Cerebellum	100	54.5
Fiber tracts	100	90.9

Incidence in percent of Gd-enhancement and Eu-VSOP accumulation, per brain region, across the whole brain.



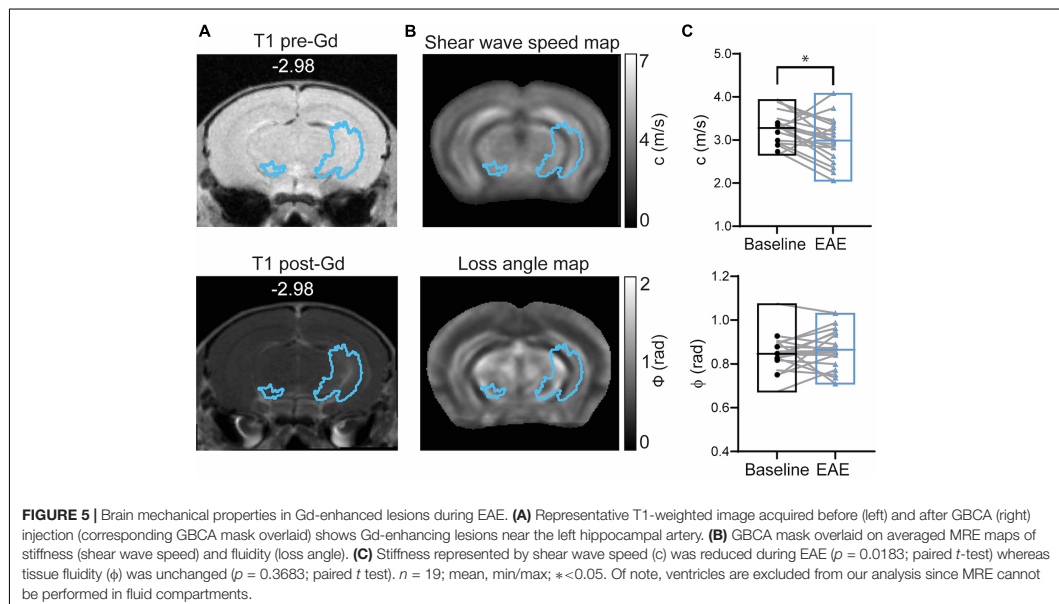
Visualization of Eu-VSOPs by IMC Reveals Association of Eu-VSOP Accumulation With Inflammatory Damage

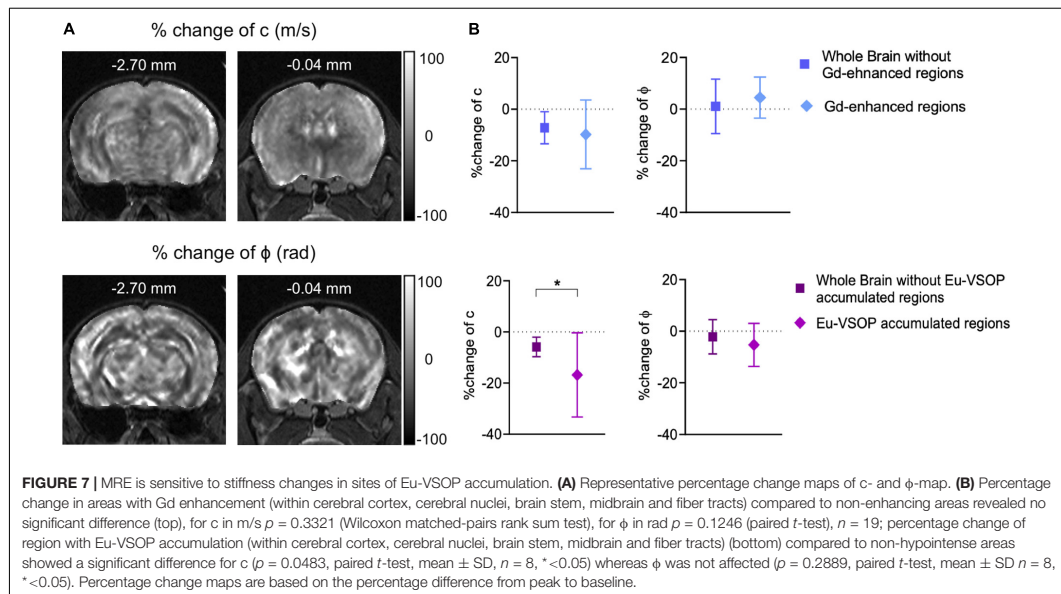
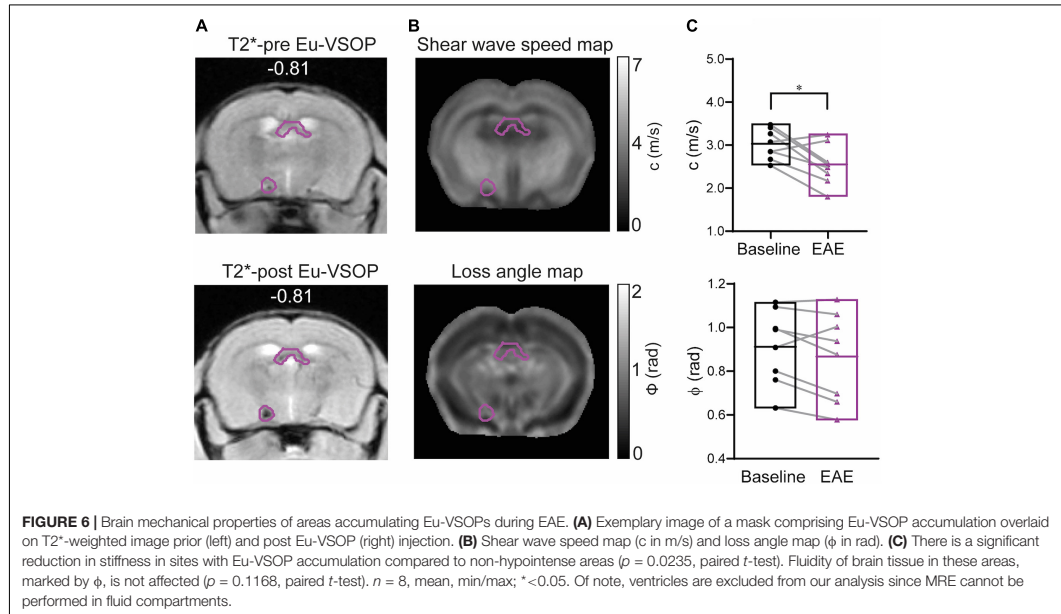
To confirm that the histopathological changes are indeed associated with inflammation-induced Eu-VSOP accumulation, we investigated inflammation in EAE and healthy control brain sections as well as the tissue distribution of Eu-VSOP and co-localization with different inflammatory and barrier cells using IMC (Figures 8, 9).

When compared with healthy control, EAE mice showed evident inflammation, with gliosis, represented by increase in Iba⁺ (white) cells and GFAP (green), as well as infiltration of immune cells (CD45, cyan) (Figure 8, white arrows). In sites where Eu-VSOPs were visualized by MRI, the particles were found to be associated with sites of inflammatory damage. In particular, areas of Eu-VSOP accumulation presented CD45 + leukocyte infiltration, mostly concentrated in perivascular cuffs, in the periventricular space (Figure 9A, arrowheads) as well as in the choroid plexus (Figure 9B, white arrows). Iba-1 + cells (microglia, macrophages) were frequently localized alongside immune infiltrates. Perivascularly, Eu-VSOP accumulation was confined to these sites of injury and colocalized with Iba-1 + and CD45 + positive cells. Furthermore, Eu-VSOPs (red dots) were found to be especially associated to the vessel walls, where they were co-localized with activated endothelial cells (CD31+). In the ventricles, Eu-VSOPs (red dots) were confined to the choroid plexus, showing a clear association with the presence of immune infiltrates (Figure 9B). No particles were found to be co-localized with NeuN + neurons. Due to the IMC resolution of 1 μm and the particle dynamic diameter of 7 nm, quantification of the particle count could not be determined.

DISCUSSION

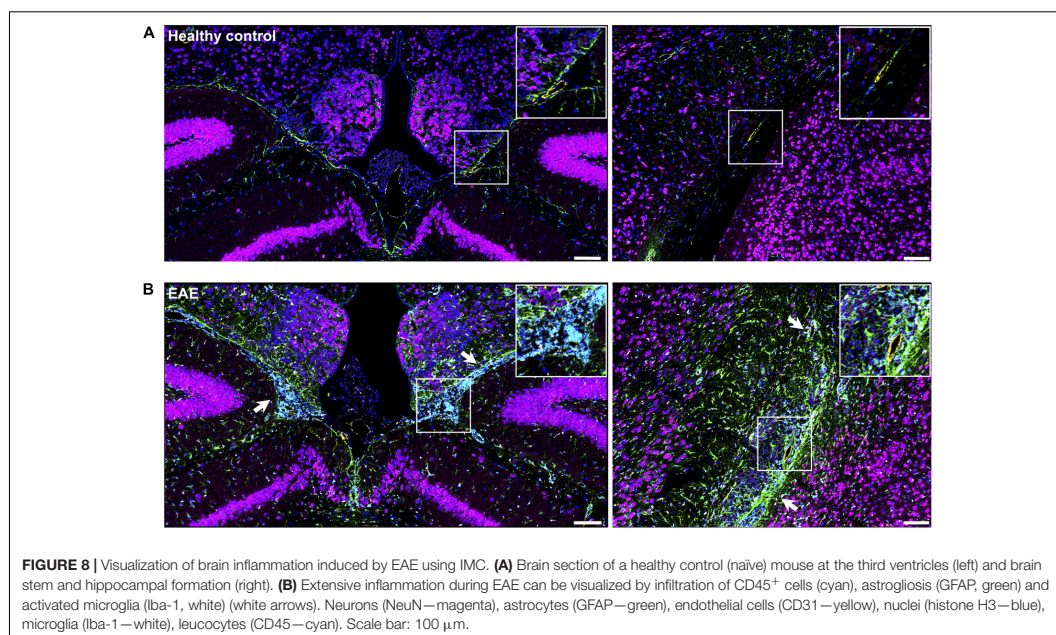
MRE has been previously shown to identify global changes in brain stiffness both in MS and in its animal model, EAE (Wuerfel et al., 2010; Streitberger et al., 2012; Riek et al., 2012; Millward et al., 2015; Wang et al., 2020). To further understand the





neuropathological alterations detected by MRE, we combined MRE with GBCA- and Eu-VSOP-enhanced MRI. Tissue viscoelasticity was then evaluated in areas of BBB leakage (GBCA-enhancing areas) and in sites with Eu-VSOP accumulation, i.e.,

areas where we have previously identified activated myeloid cells and/or altered endothelium or epithelia. To the best of our knowledge, this study for the first time combines analysis of these biochemical imaging markers with MRE findings



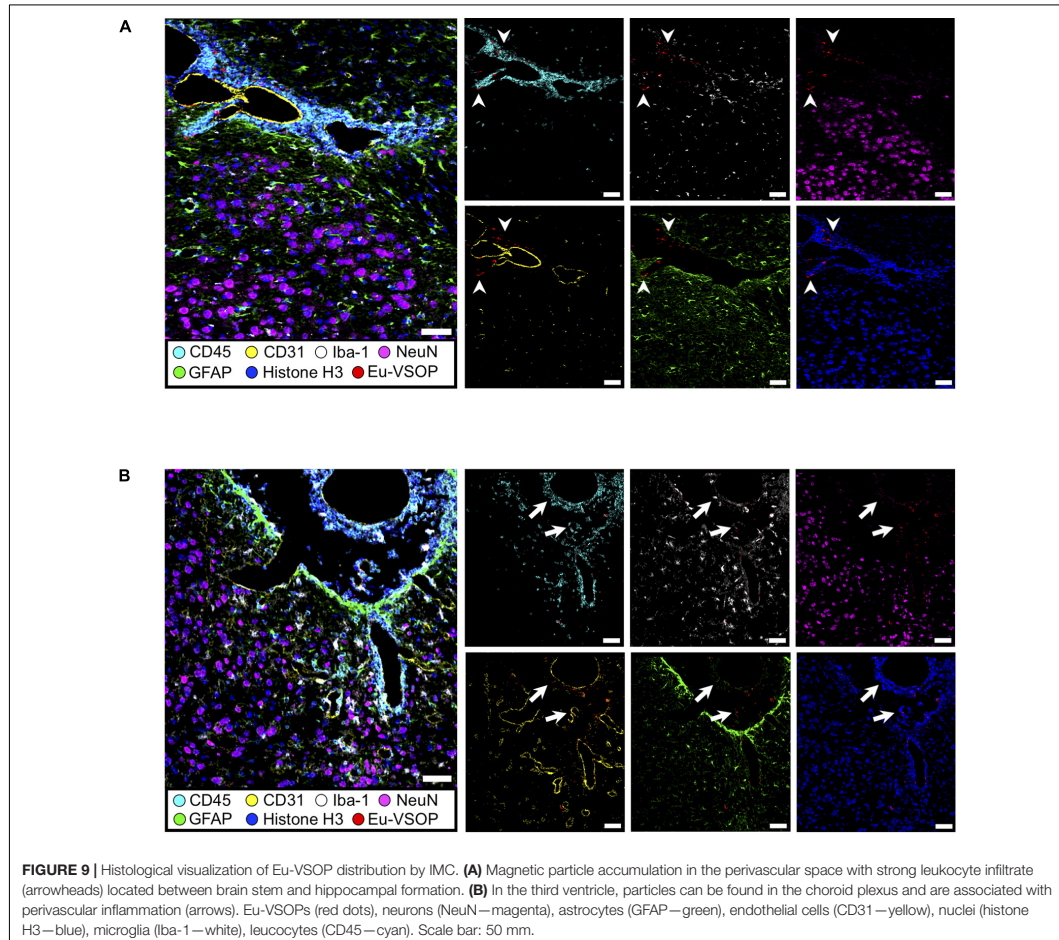
across multiple slices in a mouse model of neuroinflammation, revealing that areas of exclusive GBCA or Eu-VSOP signal displayed significant tissue softening. When these areas were compared with non-enhancing brain areas, stiffness changes at sites of Eu-VSOP accumulation showed more pronounced softening than areas of Gd-enhancement, suggesting that MRE is especially sensitive to detect inflammation-associated changes in tissue viscoelasticity. Subsequent histological visualization of Eu-VSOPs by IMC confirmed their distribution in areas of intense focal inflammation, likely undergoing significant tissue remodeling.

Here, brain viscoelastic properties were investigated in the adoptive transfer EAE model using SJL mice. The induction of this model, introduced by injection of a pre-activated population of myelin epitope-specific CD4 + T cells, results in a more severe disease with large cerebral infiltrations compared to active immunization, as used in previous studies (Riek et al., 2012; Wang et al., 2020). While in C57BL/6 mice, immunized with myelin oligodendrocyte glycoprotein (MOG) (Miller and Karpus, 2007), principally spinal cord lesions are detected, making this model less suitable for cranial MRE studies (Millward et al., 2015). Thus, the relapse-remitting adoptive transfer model in SJL mice is an appropriate tool for brain imaging studies.

In this study we confirm previous work reporting a significant global decrease in stiffness during neuroinflammation in both patients and mouse models of neuropathologies such as Alzheimer (Murphy et al., 2011; Munder et al., 2018), Parkinson disease (Lipp et al., 2013; Klein et al., 2014; Hain et al., 2016), and MS (Wuerfel et al., 2010; Streitberger et al., 2012) (Riek et al.,

2012; Millward et al., 2015; Fehlner et al., 2016; Wang et al., 2020). Based on gene expression and histopathological investigations, this reduction in stiffness correlated with the severity of inflammation. In the EAE model, an increased expression of CD3, a T-cell lineage marker (Riek et al., 2012), and F4/80 gene expression, a marker for macrophages (Millward et al., 2015), positively correlated with brain softening. Furthermore, enhanced expression of the extracellular matrix glycoprotein fibronectin was correlated with decreased stiffness, hinting at a role of neurovascular remodeling at lesion sites that contributes to changes in mechanical tissue properties (Wang et al., 2020). However, previously MRE changes were only investigated in large brain areas within one slice and thus could not account for regionally resolved inflammation. By combining contrast-enhanced MRI and multifrequency MRE with tomoelastography post processing, we were able to directly measure changes in viscoelastic properties at sites of neuroinflammation. Although, MRE was limited to the same brain segment included in previous studies using tomoelastography (Bertalan et al., 2019; Bertalan et al., 2020; Guo et al., 2019), known for acquiring multifrequency wavefield for high-resolution MRE, we were able to acquire multiple slices ranging from bregma -2.84 to 0.23 and with a resolution sufficient to resolve areas of focal inflammation. This allowed us to register MRE maps to a reference atlas, thus making the comparison within areas of contrast agent enhancement possible.

GBCA-enhanced MRI visualizes BBB permeability not only in MS patients but also in EAE models (Hawkins et al., 1990; Nessler et al., 2007; Schellenberg et al., 2007; Smorodchenko et al., 2007;



Tysiak et al., 2009; Wuerfel et al., 2007; Waiczies et al., 2012). To investigate the potential of MRE in identifying BBB-related pathological events, we directly compared mechanical properties of the brain and Gd distribution. Here, the quantification of viscoelastic parameters revealed a significant decrease in tissue stiffness in adoptive transfer EAE.

As apparent from the incidence maps, all mice had GBCA enhancement, as also shown by Smorodchenko et al., 2007. Confirming previous results (Smorodchenko et al., 2007; Wuerfel et al., 2007), our findings showed marked involvement of the brain, with extensive cerebellar enhancement (bregma -7.32 and -5.50 mm), notably at the 4th ventricle; similarly, but to a lesser extent, the brain stem was also affected. Cerebellar susceptibility to BBB breakdown is an expected outcome of this model and is attributable to the high degree of vascularization in this area (Tonra, 2002). Other regions showing Gd-enhancement included

the periventricular areas, hippocampus, thalamus, hypothalamus and midbrain (bregma -3.26 to -1.86), with particularly pronounced enhancement close to major vessels such as the hippocampal artery and in their adjacency. This pattern of enhancement has been described in other EAE models before (Kuharik et al., 1988; Smorodchenko et al., 2007; Wuerfel et al., 2007).

However, Gd-enhancing areas showed a reduction in stiffness similar to that observed in non-enhancing areas of the inflamed brain. Given that Gd-enhancement is often visualized as areas of diffuse hyperintensity and much more extensive compared with the pattern of Eu-VSOP accumulation, we hypothesize that the viscoelastic effect observed in areas of Gd-enhancement does not reflect strictly localized histopathological alterations purely associated with BBB breakdown, but rather indicates predominantly a disseminated softening due to the inflammatory

state of the brain. Although GBCA diffusion within the tissue primarily represents increased BBB permeability and has been correlated with glial cell activation (Nessler et al., 2007; Morrissey et al., 1996), its spatial distribution is not only limited to these events. After crossing the BBB, GBCA diffusion and dispersion throughout the tissue could also be attributed to factors such as the contrast agent's distribution in the interstitial and intracellular spaces, an inherent property of a molecule's biodistribution (Aime and Caravan, 2009), the degree of vascular disruption and leakiness (Layne et al., 2018), or the reduction of perfusion or extracellular space in areas of inflammatory lesions (Nessler et al., 2007).

Previous studies have shown that Gd-enhancing lesions are present before disease signs become apparent (Wuerfel et al., 2007) but rarely correlate with the presence of characteristic immune infiltrate-derived lesions, a hallmark of EAE and MS (Nessler et al., 2007; Nathoo et al., 2014). In contrast, we show that Eu-VSOPs also accumulate in areas that are not enhanced by GBCA and are present at sites of immune cell infiltration, which is in alignment with the literature (Tysiak et al., 2009; Millward et al., 2019; Berndt et al., 2017). More precisely, we found Eu-VSOPs to be dispersed and mostly located in the vicinity of vessels and ventricles, as indicated in the incidence maps. In the cerebellum, comprising approximately the bregma coordinates -7.32 to -5.50 mm, Eu-VSOP accumulations were found next to the 4th ventricle, the dorsomedial cerebellar arteries, lateral superior cerebral artery, and close to the basilar artery. In the bregma -3.26 mm to 0.23 mm, including structures such as the hippocampus, and the lateral and 3rd ventricles, Eu-VSOPs appear to be located close to the anterior choroidal artery (for anatomical references refer to Dorr et al. (2007) and Xiong et al. (2017)). Different routes have been proposed to explain how VSOPs can enter the brain: phagocytosis by peripheral macrophages (Tysiak et al., 2009; Millward et al., 2019) and activated T cells (Wuerfel et al., 2007), which then infiltrate the CNS; passive diffusion through the leaky BBB as freely diffusing particles as observed in the parenchyma of EAE mice (Millward et al., 2013); and binding to endothelial or epithelial barriers (Plewes et al., 1995; Streitberger et al., 2012). Eu-VSOPs were imaged 24 h after injection when they have been shown to be cleared from the blood (Wuerfel et al., 2007). Therefore, we propose that hypointense signals seen in T2* images originate primarily from VSOP bound to altered ECM components (Berndt et al., 2017) or from particles phagocytosed by peripheral macrophages or/and activated microglia present at sites of inflammation (Tysiak et al., 2009; Millward et al., 2013, 2019). However, it cannot be excluded that these hypointense signals originate from particles phagocytosed by intravascular immune cells patrolling the endothelium and ready to cross upon inflammatory signals as reported in Masthoff et al., 2018 (Masthoff et al., 2018). Taken together, these evidence indicate that magnetic particles reveal histopathological alterations other than the well-known BBB disruption underlying GBCA enhancement (Tysiak et al., 2009; Millward et al., 2013; Berndt et al., 2017).

Importantly, our results show that, during inflammation, stiffness is particularly reduced in regions of Eu-VSOP

accumulation compared to global brain softening. To elucidate underlying alterations in sites with Eu-VSOP accumulation that might contribute to the marked reduction in stiffness, we performed histological assessment of the particles. Differently from the unspecific method to detect iron particles, the Prussian blue stain, here we show that Eu-VSOPs can be visualized by IMC. The IMC allows a distinguishable detection of the Eu present in the core of the particles, and additionally, provides important information on the cellular environment in sites of particle accumulation. We found that Eu-VSOPs accumulated at sites of inflammation, as co-localization with leukocyte infiltrate was evident, in line with our previous reports (Millward et al., 2013). In areas without hypointense signal, particles may be found scattered in the tissue, possibly after diffusing through the disrupted BBB and accumulating in the brain parenchyma. Consequently, passively diffused particles would not contribute to the MRI signal 24 h after injection as much as the phagocytosed particles accumulated in sites of strong inflammation.

In contrast to tissue from EAE mice, histological analysis of healthy control further confirmed no Eu-VSOP accumulation in the non-inflamed brain tissue, indicating that Eu-VSOP accumulation is caused by processes of inflammation. Accumulations within the investigated inflamed tissue sections were mostly concentrated in the perivascular cuffs and in the periventricular space as well as in the choroid plexus. In areas of inflammatory alterations, we found particles co-localized with endothelial cells, which could have been uptaken *via* inflammation-induced alterations of sulfated glycosaminoglycans on the endothelial glycocalyx (Berndt et al., 2017) and with CD45 + and Iba-1 + cells, suggesting that they were phagocytosed. During EAE, astrogliosis and pronounced microglial activation were observed, presenting a typically hypertrophic and ramified morphology. Eu-VSOPs were also specifically co-localized with activated microglia, consistent with previous reports (Wuerfel et al., 2007; Tysiak et al., 2009; Millward et al., 2013, 2019). Atomic force microscopy has shown that glial cells are relatively softer than their neighboring neurons (Lu et al., 2006), as GFAP-expressing cells were associated with lower stiffness values (Moeendarbary et al., 2017). Therefore, in inflamed regions, the presence of softer glial cells could be one contributing factor to the marked decrease in stiffness observed in sites of Eu-VSOP accumulation. Additionally, the inflammatory activity of infiltrating peripheral immune cells and activated glial cells in these areas could result in extensive remodeling of the ECM. In addition, secretion of metalloproteinases during neuroinflammation leads to the degradation of ECM components, which facilitates further disruption of the BBB [for a review refer to Rosenberg (2002)]. A dynamic alteration of the ECM structure with accumulation of other matrix components, such as fibronectin, has also been demonstrated for EAE and correlates with neural tissue softening (Wang et al., 2020).

Moreover, although there are no studies directly associating vasogenic edema with viscoelastic changes in EAE, reports on mice with stroke lesions have linked edema with brain softening in the ipsilateral side (Xu et al., 2013, 2014). Thus, it is possible

that vasogenic edema associated with the cellular inflammation depicted may also influence tissue elasticity in areas with VSOPs.

The pronounced softening observed at sites of Eu-VSOP accumulation suggests that an intense focal inflammatory process has a strong effect on viscoelastic parameters. This could be attributable to a combined influence of activated glial cells, accumulation of immune cells, local edema, and/or remodeling of the extracellular matrix, especially in the microenvironment of the neurovascular unit. On the other hand, GBCA-enhanced MRI reflects a transient event of enhanced vessel permeability and may only account for one aspect of the inflammatory state in a multifactorial disease model. Hence, the contribution of the dynamic disturbance of the BBB possibly results in a different distribution of Eu-VSOP accumulation compared to Gd-enhancement.

To be able to distinguish neuroinflammatory processes visualized either by GBCA or by VSOPs, masks comprising solely each contrast agent were generated. Areas, in which Eu-VSOP accumulation overlaps with Gd-enhancement might contain particles that just passively diffuse into the brain parenchyma through a damaged BBB. Thus, particles co-localizing with GBCA-enhancement would not reveal distinct aspects of inflammation different from BBB leakage and were not considered for this investigation.

One limitation of our study is that the brain area covered by tomoelastography is limited to the bregma areas -2.84 mm to 0.23 mm. It is well documented, for instance, that the cerebellum is a particularly affected region in EAE models (Tonra, 2002; Wuerfel et al., 2007; Millward et al., 2015) though it could not be included in our analysis. Therefore, it would be important to include these regions in future studies to incorporate crucial pathological information into the imaging findings. Moreover, based on previous studies, we consider that 24 h after injection, Magnevist is completely depleted from the blood and the brain (Tysiak et al., 2009; Wang et al., 2020). Thus, an effect on the T2*-weighted image used for quantification of Eu-VSOP is highly unlikely. However, since we did not perform a T1 scan before the second T2*-weighted scan, it is not possible to completely exclude a residual effect of the GBCA.

A noteworthy point to mention is that studies involving *in vivo* VSOP imaging requires intravenous administration of particles with the obvious associated safety concerns if a clinical application in the future is intended. As changes in viscoelastic properties in areas of VSOP accumulation was shown to be detectable by MRE, we propose that MRE may represent a suitable non-invasive imaging method that allows *in vivo* visualization of broad pathological processes. MRE could therefore be applied to both, pre-clinical and clinical settings in the context of neuroinflammation, serving as a tool for research, diagnostic, and therapy monitoring.

CONCLUSION

Combining for the first time Gd-enhancement and Eu-VSOP with *in vivo* multifrequency MRE, we obtained results suggesting that MRE is able to detect non-invasively pathological

processes associated with inflammation beyond BBB disruption and vascular leakage. Such processes visualized by Eu-VSOP-enhanced MRI may involve gliosis and macrophages infiltration as well as alterations of endothelial matrix components and ECM remodeling. MRE may serve to visualize *in vivo* a broad spectrum of pathological processes and represents, therefore, a useful non-invasive imaging tool for neuroinflammation in preclinical and clinical settings.

DATA AVAILABILITY STATEMENT

The raw data supporting the conclusions of this article will be made available by the authors, without undue reservation.

ETHICS STATEMENT

The animal study was reviewed and approved by Berlin State Office for Health and Social Affairs (LAGeSo), Berlin, Germany.

AUTHOR CONTRIBUTIONS

AM and RS: experimental design, data acquisition, data analysis and interpretation, and manuscript writing. YR-S and DK: IMC design, image acquisition, image processing, and manuscript revision. HT: supervision of MRE data analysis and manuscript revision. AK: IMC resources and manuscript revision. JS and MT: Eu-VSOP resources and manuscript revision. SK: technical assistance, supervision of MRI data registration, and manuscript revision. SM and PB-S: technical assistance, supervision of MRI design and data analysis, and manuscript revision. CI-D and IS: conceptualization, data interpretation, funding acquisition, resources, methodology, project administration, supervision, and editing and critical revision of manuscript. All authors fully qualify for authorship and have approved the final version of the manuscript.

FUNDING

This work was funded by the Deutsche Forschungsgemeinschaft (DFG, German Research Foundation)—project number 372486779—SFB 1340_ Projects A01, B05, B06, C01, and C03, the Einstein Center for Neurosciences Berlin (ECN) and the Research Training Group GRK2260 BIOQIC.

ACKNOWLEDGMENTS

We would like to thank Natascha Asselborn for technical assistance.

SUPPLEMENTARY MATERIAL

The Supplementary Material for this article can be found online at: <https://www.frontiersin.org/articles/10.3389/fnins.2021.701308/full#supplementary-material>

REFERENCES

- Aime, S., and Caravan, P. (2009). Biodistribution of gadolinium-based contrast agents, including gadolinium deposition. *J. Magn. Reson. Imaging* 30, 1259–1267. doi: 10.1002/jmri.21969
- Alvarez, J. I., Cayrol, R., and Prat, A. (2011). Disruption of central nervous system barriers in multiple sclerosis. *Biochim. Biophys. Acta* 1812, 252–264.
- Berndt, D., Millward, J. M., Schnorr, J., Taupitz, M., Stangl, V., Paul, F., et al. (2017). Inflammation-induced brain endothelial activation leads to uptake of electrostatically stabilized iron oxide nanoparticles via sulfated glycosaminoglycans. *Nanomedicine* 13, 1411–1421. doi: 10.1016/j.nano.2017.01.010
- Bertalan, G., Guo, J., Tzschätzsch, H., Klein, C., Barnhill, E., Sack, I., et al. (2019). Fast tomoeleostography of the mouse brain by multifrequency single-shot MR elastography. *Magn. Reson. Med.* 81, 2676–2687. doi: 10.1002/mrm.27586
- Bertalan, G., Klein, C., Schreyer, S., Steiner, B., Krefl, B., Tzschätzsch, H., et al. (2020). Biomechanical properties of the hypoxic and dying brain quantified by magnetic resonance elastography. *Acta Biomater.* 101, 395–402. doi: 10.1016/j.actbio.2019.11.011
- de Schellenberger, A. A., Hauptmann, R., Millward, J. M., Schellenberger, E., Kobayashi, Y., Taupitz, M., et al. (2017). Synthesis of europium-doped VSP, customized enhancer solution and improved microscopy fluorescence methodology for unambiguous histological detection. *J. Nanobiotechnol.* 15, 1–14.
- Dorr, A., Sled, J. G., and Kabani, N. (2007). Three-dimensional cerebral vasculature of the CBA mouse brain: a magnetic resonance imaging and micro computed tomography study. *Neuroimage* 35, 1409–1423. doi: 10.1016/j.neuroimage.2006.12.040
- Fehlner, A., Behrens, J. R., Streitberger, K. J., Papazoglou, S., Braun, J., Bellmann-Strobl, J., et al. (2016). Higher-resolution MR elastography reveals early mechanical signatures of neuroinflammation in patients with clinically isolated syndrome. *J. Magn. Reson. Imaging* 44, 51–58. doi: 10.1002/jmri.25129
- Guo, J., Bertalan, G., Meierhofer, D., Klein, C., Schreyer, S., Steiner, B., et al. (2019). Brain maturation is associated with increasing tissue stiffness and decreasing tissue fluidity. *Acta Biomater.* 99, 433–442. doi: 10.1016/j.actbio.2019.08.036
- Hain, E. G., Klein, C., Munder, T., Braun, J., Riek, K., Mueller, S., et al. (2016). Dopaminergic neurodegeneration in the mouse is associated with decrease of viscoelasticity of substantia nigra tissue. *PLoS One* 11:e0161179. doi: 10.1371/journal.pone.0161179
- Hawkins, C., Munro, P., MacKenzie, F., Kesselring, J., Tofts, P., Boulay, E. D., et al. (1990). Duration and selectivity of blood-brain barrier breakdown in chronic relapsing experimental allergic encephalomyelitis studied by gadolinium-DTPA and protein markers. *Brain* 113, 365–378. doi: 10.1093/brain/113.2.365
- Hirsch, S., Braun, J., and Sack, I. (2017). *Magnetic resonance elastography: physical background and medical applications*. Hoboken, NJ: John Wiley & Sons.
- Hiscox, L. V., Johnson, C. L., Barnhill, E., McGarry, M. D., Huston, J., van Beek, E. J., et al. (2016). Magnetic resonance elastography (MRE) of the human brain: technique, findings and clinical applications. *Phys. Med. Biol.* 61, R401–R437.
- Klein, C., Hain, E. G., Braun, J., Riek, K., Mueller, S., Steiner, B., et al. (2014). Enhanced adult neurogenesis increases brain stiffness: *in vivo* magnetic resonance elastography in a mouse model of dopamine depletion. *PLoS One* 9:e92582. doi: 10.1371/journal.pone.0092582
- Klein, S., Staring, M., Murphy, K., Viergever, M. A., and Pluijm, J. P. (2009). Elastix: a toolbox for intensity-based medical image registration. *IEEE Trans. Med. Imaging* 29, 196–205. doi: 10.1109/tmi.2009.2035616
- Koch, S., Mueller, S., Foddiss, M., Bienert, T., von Elverfeldt, D., Knab, F., et al. (2019). Atlas registration for edema-corrected MRI lesion volume in mouse stroke models. *J. Cerebral. Blood Flow Metabol.* 39, 313–323. doi: 10.1177/0271678x17726635
- Kuharik, M., Edwards, M., Farlow, M., Becker, G., Azzarelli, B., Klatte, E., et al. (1988). Gd-enhanced MR imaging of acute and chronic experimental demyelinating lesions. *Am. J. Neuroradiol.* 9, 643–648.
- Lassmann, H. (2008). The pathologic substrate of magnetic resonance alterations in multiple sclerosis. *Neuroimaging Clin. North Am.* 18, 563–576. doi: 10.1016/j.nic.2008.06.005
- Layne, K. A., Dargan, P. I., Archer, J. R., and Wood, D. M. (2018). Gadolinium deposition and the potential for toxicological sequelae—A literature review of issues surrounding gadolinium-based contrast agents. *Br. J. Clin. Pharmacol.* 84, 2522–2534. doi: 10.1111/bcp.13718
- Lipp, A., Trbojevic, R., Paul, F., Fehlner, A., Hirsch, S., Scheel, M., et al. (2013). Cerebral magnetic resonance elastography in supranuclear palsy and idiopathic Parkinson's disease. *NeuroImage Clin.* 3, 381–387. doi: 10.1016/j.nicl.2013.09.006
- Lu, Y.-B., Franze, K., Seifert, G., Steinhäuser, C., Kirchhoff, F., Wolburg, H., et al. (2006). Viscoelastic properties of individual glial cells and neurons in the CNS. *Proc. Natl. Acad. Sci.* 103, 17759–17764. doi: 10.1073/pnas.0606150103
- Manduca, A., Bayly, P. J., Ehman, R. L., Kolipaka, A., Royston, T. J., Sack, I., et al. (2021). MR elastography: Principles, guidelines, and terminology. *Magn. Reson. Med.* 85, 2377–2390. doi: 10.1002/mrm.28627
- Masthoff, M., Gran, S., Zhang, X., Wachsmuth, L., Bietenbeck, M., Helfen, A., et al. (2018). Temporal window for detection of inflammatory disease using dynamic cell tracking with time-lapse MRI. *Sci. Rep.* 8:9563.
- Miller, S. D., and Karpus, W. J. (2007). Experimental autoimmune encephalomyelitis in the mouse. *Curr. Protoc. Immunol.* 15:15.1.
- Millward, J. M., de Schellenberger, A. A., Berndt, D., Hanke-Vela, L., Schellenberger, E., Waiczies, S., et al. (2019). Application of europium-doped very small iron oxide nanoparticles to visualize neuroinflammation with MRI and fluorescence microscopy. *Neuroscience* 403, 136–144. doi: 10.1016/j.neuroscience.2017.12.014
- Millward, J. M., Guo, J., Berndt, D., Braun, J., Sack, I., and Infante-Duarte, C. (2015). Tissue structure and inflammatory processes shape viscoelastic properties of the mouse brain. *NMR Biomed.* 28, 831–839. doi: 10.1002/nbm.3319
- Millward, J. M., Schnorr, J., Taupitz, M., Wagner, S., Wuerfel, J. T., and Infante-Duarte, C. (2013). Iron oxide magnetic nanoparticles highlight early involvement of the choroid plexus in central nervous system inflammation. *ASN Neuro* 5:e00110.
- Moecendarbary, E., Weber, I. P., Sheridan, G. K., Koser, D. E., Soleman, S., Haenzi, B., et al. (2017). The soft mechanical signature of glial scars in the central nervous system. *Nat. Commun.* 8, 1–11.
- Morrissey, S. P., Stodal, H., Zettl, U., Simonis, C., Jung, S., Kiefer, R., et al. (1996). *In vivo* MRI and its histological correlates in acute adoptive transfer experimental allergic encephalomyelitis: quantification of inflammation and oedema. *Brain* 119, 239–248. doi: 10.1093/brain/119.1.239
- Munder, T., Pfeffer, A., Schreyer, S., Guo, J., Braun, J., Sack, I., et al. (2018). MR elastography detection of early viscoelastic response of the murine hippocampus to amyloid β accumulation and neuronal cell loss due to Alzheimer's disease. *J. Magn. Reson. Imaging* 47, 105–114. doi: 10.1002/jmri.25741
- Murphy, M. C., Huston, J. III, Jack, C. R. Jr., Glaser, K. J., Manduca, A., Felmlee, J. P., et al. (2011). Decreased brain stiffness in Alzheimer's disease determined by magnetic resonance elastography. *J. Magn. Reson. Imaging* 34, 494–498. doi: 10.1002/jmri.22707
- Muthupillai, R., Lomas, D., Rossman, P., Greenleaf, J. F., Manduca, A., and Ehman, R. L. (1995). Magnetic resonance elastography by direct visualization of propagating acoustic strain waves. *Science* 269, 1854–1857. doi: 10.1126/science.7569924
- Nathoo, N., Yong, V. W., and Dunn, J. F. (2014). Understanding disease processes in multiple sclerosis through magnetic resonance imaging studies in animal models. *NeuroImage Clin.* 4, 743–756. doi: 10.1016/j.nicl.2014.04.011
- Nessler, S., Boretius, S., Stadelmann, C., Bittner, A., Merkler, D., Hartung, H.-P., et al. (2007). Early MRI changes in a mouse model of multiple sclerosis are predictive of severe inflammatory tissue damage. *Brain* 130, 2186–2198. doi: 10.1093/brain/awm105
- Plewes, D., Betty, I., Urchuk, S., and Soutar, I. (1995). Visualizing tissue compliance with MR imaging. *J. Magn. Reson. Imaging* 5, 733–738. doi: 10.1002/jmri.1880050620
- Riek, K., Millward, J. M., Hamann, I., Mueller, S., Pfueller, C. F., Paul, F., et al. (2012). Magnetic resonance elastography reveals altered brain viscoelasticity in experimental autoimmune encephalomyelitis. *NeuroImage Clin.* 1, 81–90. doi: 10.1016/j.nicl.2012.09.003
- Rosenberg, G. A. (2002). Matrix metalloproteinases in neuroinflammation. *Glia* 39, 279–291. doi: 10.1002/glia.10108
- Schellenberger, A. E., Buist, R., Yong, V. W., Del Bigio, M. R., and Peeling, J. (2007). Magnetic resonance imaging of blood–spinal cord barrier disruption

- in mice with experimental autoimmune encephalomyelitis. *Magn. Reson. Med.* 58, 298–305. doi: 10.1002/mrm.21289
- Schregel, K., Wuerfel, E., Garteiser, P., Gemeinhardt, I., Prozorovski, T., Aktas, O., et al. (2012). Demyelination reduces brain parenchymal stiffness quantified *in vivo* by magnetic resonance elastography. *Proc. Natl. Acad. Sci. U S A.* 109, 6650–6655. doi: 10.1073/pnas.1200151109
- Smorodchenko, A., Wuerfel, J., Pohl, E. E., Vogt, J., Tysiak, E., Glumm, R., et al. (2007). CNS-irrelevant T-cells enter the brain, cause blood–brain barrier disruption but no glial pathology. *Eur. J. Neurosci.* 26, 1387–1398. doi: 10.1111/j.1460-9568.2007.05792.x
- Streitberger, K.-J., Sack, I., Krefling, D., Pfüller, C., Braun, J., Paul, F., et al. (2012). Brain viscoelasticity alteration in chronic-progressive multiple sclerosis. *PLoS One* 7:e29888. doi: 10.1371/journal.pone.0029888
- Taupitz, M., Schnorr, J., Abramjuk, C., Wagner, S., Pilgrim, H., Hünigen, H., et al. (2000). New generation of monomer-stabilized very small superparamagnetic iron oxide particles (VSOP) as contrast medium for MR angiography: Preclinical results in rats and rabbits. *J. Magn. Reson. Imaging* 12, 905–911. doi: 10.1002/1522-2586(200012)12:6<905::aid-jmri14>3.0.co;2-5
- Thompson, A., Baranzini, S., Geurts, J., Hemmer, B., and Ciccarelli, O. (2018). Multiple sclerosis. *Lancet* 391, 1622–1636.
- Tonra, J. R. (2002). Cerebellar susceptibility to experimental autoimmune encephalomyelitis in SJL/J mice: potential interaction of immunology with vascular anatomy. *Cerebellum* 1, 57–68. doi: 10.1080/147342202753203096
- Tysiak, E., Asbach, P., Aktas, O., Waiczies, H., Smyth, M., Schnorr, J., et al. (2009). Beyond blood brain barrier breakdown—*in vivo* detection of occult neuroinflammatory foci by magnetic nanoparticles in high field MRI. *J. Neuroinflamm.* 6, 1–8.
- Tzschätzsch, H., Guo, J., Dittmann, F., Hirsch, S., Barnhill, E., Jöhrens, K., et al. (2016). Tomoelastography by multifrequency wave number recovery from time-harmonic propagating shear waves. *Med. Image Anal.* 30, 1–10. doi: 10.1016/j.media.2016.01.001
- Wagner, S., Schnorr, J., Pilgrim, H., Hamm, B., and Taupitz, M. (2002). Monomer-coated very small superparamagnetic iron oxide particles as contrast medium for magnetic resonance imaging: preclinical *in vivo* characterization. *Investig. Radiol.* 37, 167–177. doi: 10.1097/00004424-200204000-00002
- Waiczies, H., Millward, J. M., Lepore, S., Infante-Duarte, C., Pohlmann, A., Niendorf, T., et al. (2012). Identification of cellular infiltrates during early stages of brain inflammation with magnetic resonance microscopy. *PLoS One* 7:e32796. doi: 10.1371/journal.pone.0032796
- Wang, S., Hesse, B., Roman, M., Stier, D., Castillo-Michel, H., Cotte, M., et al. (2019). Increased retention of gadolinium in the inflamed brain after repeated administration of gadopentetate dimeglumine: a proof-of-concept study in mice combining ICP-MS and micro- and Nano-SR-XRF. *Investig. Radiol.* 54, 617–626. doi: 10.1097/rli.0000000000000571
- Wang, S., Millward, J. M., Hanke-Vela, L., Malla, B., Pilch, K., Gil-Infante, A., et al. (2020). MR elastography-based assessment of matrix remodeling at lesion sites associated with clinical severity in a model of multiple sclerosis. *Front. Neurol.* 10:1382. doi: 10.3389/fneur.2019.01382
- Wuerfel, J., Paul, F., Beierbach, B., Hamhaber, U., Klatt, D., Papazoglou, S., et al. (2010). MR-elastography reveals. *Neuroimage* 49, 2520–2525. doi: 10.1016/j.neuroimage.2009.06.018
- Wuerfel, J., Tysiak, E., Prozorovski, T., Smyth, M., Mueller, S., Schnorr, J., et al. (2007). Mouse model mimics multiple sclerosis in the clinico-radiological paradox. *Eur. J. Neurosci.* 26, 190–198. doi: 10.1111/j.1460-9568.2007.05644.x
- Xiong, B., Li, A., Lou, Y., Chen, S., Long, B., Peng, J., et al. (2017). Precise cerebral vascular atlas in stereotaxic coordinates of whole mouse brain. *Front. Neuroanat.* 11:128. doi: 10.3389/fnana.2017.00128
- Xu, Z. S., Lee, R. J., Chu, S. S., Yao, A., Paun, M. K., Murphy, S. P., et al. (2013). Evidence of changes in brain tissue stiffness after ischemic stroke derived from ultrasound-based elastography. *J. Ultrasound Med.* 32, 485–494. doi: 10.7863/jum.2013.32.3.485
- Xu, Z. S., Yao, A., Chu, S. S., Paun, M. K., McClintic, A. M., Murphy, S. P., et al. (2014). Detection of mild traumatic brain injury in rodent models using shear wave elastography: preliminary studies. *J. Ultrasound Med.* 33, 1763–1771. doi: 10.7863/ultra.33.10.1763
- Zéphir, H. (2018). Progress in understanding the pathophysiology of multiple sclerosis. *Revue Neurol.* 174, 358–363. doi: 10.1016/j.neuro.2018.03.006

Conflict of Interest: The authors declare that the research was conducted in the absence of any commercial or financial relationships that could be construed as a potential conflict of interest.

Publisher's Note: All claims expressed in this article are solely those of the authors and do not necessarily represent those of their affiliated organizations, or those of the publisher, the editors and the reviewers. Any product that may be evaluated in this article, or claim that may be made by its manufacturer, is not guaranteed or endorsed by the publisher.

Copyright © 2021 Silva, Morr, Mueller, Koch, Boehm-Sturm, Rodriguez-Silke, Kunkel, Tzschätzsch, Kühl, Schnorr, Taupitz, Sack and Infante-Duarte. This is an open-access article distributed under the terms of the Creative Commons Attribution License (CC BY). The use, distribution or reproduction in other forums is permitted, provided the original author(s) and the copyright owner(s) are credited and that the original publication in this journal is cited, in accordance with accepted academic practice. No use, distribution or reproduction is permitted which does not comply with these terms.




Publication 2: Sexual Dimorphism in Extracellular Matrix Composition and Viscoelasticity of the Healthy and Inflamed Mouse Brain

Journal Data Filtered By: **Selected JCR Year: 2020** Selected Editions: SCIE,SSCI
 Selected Categories: **"BIOLOGY"** Selected Category Scheme: WoS
Gesamtanzahl: 93 Journale

Rank	Full Journal Title	Total Cites	Journal Impact Factor	Eigenfactor Score
1	BIOLOGICAL REVIEWS	17,047	12.820	0.019750
2	Physics of Life Reviews	1,942	11.025	0.003280
3	CURRENT BIOLOGY	78,289	10.834	0.116100
4	BIOSCIENCE	22,560	8.589	0.012470
5	eLife	68,113	8.140	0.287820
6	PLOS BIOLOGY	39,598	8.029	0.059920
7	BMC BIOLOGY	8,577	7.431	0.015750
8	Communications Biology	4,996	6.268	0.016030
9	PHILOSOPHICAL TRANSACTIONS OF THE ROYAL SOCIETY B- BIOLOGICAL SCIENCES	56,921	6.237	0.055730
10	Science China-Life Sciences	6,307	6.038	0.006960
11	BIOLOGICAL RESEARCH	2,563	5.612	0.002270
12	BIOELECTROCHEMISTRY	6,107	5.373	0.004870
13	PROCEEDINGS OF THE ROYAL SOCIETY B- BIOLOGICAL SCIENCES	64,652	5.349	0.061070
14	FASEB JOURNAL	54,279	5.191	0.044390
15	Current Opinion in Insect Science	3,455	5.186	0.008610
16	Biology-Basel	2,726	5.079	0.003990
17	QUARTERLY REVIEW OF BIOLOGY	4,781	4.875	0.000920
18	Life Science Alliance	1,208	4.591	0.004260
19	COMPUTERS IN BIOLOGY AND MEDICINE	9,751	4.589	0.011860
20	Biology Direct	2,265	4.540	0.002430
21	Geobiology	2,793	4.407	0.003600
22	BIOESSAYS	11,559	4.345	0.011680
23	ASTROBIOLOGY	4,963	4.335	0.005570
24	SAUDI JOURNAL OF BIOLOGICAL SCIENCES	6,487	4.219	0.007240
25	EXCLI Journal	2,642	4.068	0.002870
26	Interface Focus	2,863	3.906	0.004480
27	Life-Basel	1,851	3.817	0.003870
28	Biology Letters	12,880	3.703	0.016230
29	JOURNAL OF EXPERIMENTAL BIOLOGY	40,334	3.312	0.026860
30	JOURNAL OF BIOLOGICAL RHYTHMS	4,128	3.182	0.003270
31	YALE JOURNAL OF BIOLOGY AND MEDICINE	2,938	3.026	0.003300

Article

Sexual Dimorphism in Extracellular Matrix Composition and Viscoelasticity of the Healthy and Inflamed Mouse Brain

Clara Sophie Batzdorf ¹, Anna Sophie Morr ², Gergely Bertalan ², Ingolf Sack ², Rafaela Vieira Silva ^{1,3,†} and Carmen Infante-Duarte ^{1,*,†}

- ¹ Experimental and Clinical Research Center, Max Delbrück Center for Molecular Medicine and Charité—Universitätsmedizin Berlin, Corporate Member of Freie Universität Berlin and Humboldt-Universität zu Berlin, Lindenberger Weg 80, 13125 Berlin, Germany; clara.batzdorf@charite.de (C.S.B.); rafaela.vieira-da-silva@charite.de (R.V.S.)
- ² Department of Radiology, Charité—Universitätsmedizin Berlin, Corporate Member of Freie Universität Berlin and Humboldt-Universität zu Berlin, Charitéplatz 1, 10117 Berlin, Germany; anna-sophie.morr@charite.de (A.S.M.); gergely.bertalan@charite.de (G.B.); ingolf.sack@charite.de (I.S.)
- ³ Einstein Center for Neurosciences Berlin, Charité—Universitätsmedizin Berlin, Corporate Member of Freie Universität Berlin and Humboldt-Universität zu Berlin, Charitéplatz 1, 10117 Berlin, Germany
- * Correspondence: carmen.infante@charite.de
- † These authors contributed equally to this work.

Simple Summary: In multiple sclerosis (MS), an autoimmune disease of the central nervous system that primarily affects women, gender differences in disease course and in brain softening have been reported. It has been shown that the molecular network found between the cells of the tissue, the extracellular matrix (ECM), influences tissue stiffness. However, it is still unclear if sex influences ECM composition. Therefore, here we investigated how brain ECM and stiffness differ between sexes in the healthy mouse, and in an MS mouse model. We applied multifrequency magnetic resonance elastography and gene expression analysis for associating in vivo brain stiffness with ECM protein content in the brain, such as collagen and laminin. We found that the cortex was softer in males than in females in both healthy and sick mice. Softening was associated with sex differences in expression levels of collagen and laminin. Our findings underscore the importance of considering sex when studying the constitution of brain tissue in health and disease, particularly when investigating the processes underlying gender differences in MS.

Abstract: Magnetic resonance elastography (MRE) has revealed sexual dimorphism in brain stiffness in healthy individuals and multiple sclerosis (MS) patients. In an animal model of MS, named experimental autoimmune encephalomyelitis (EAE), we have previously shown that inflammation-induced brain softening was associated with alterations of the extracellular matrix (ECM). However, it remained unclear whether the brain ECM presents sex-specific properties that can be visualized by MRE. Therefore, here we aimed at quantifying sexual dimorphism in brain viscoelasticity in association with ECM changes in healthy and inflamed brains. Multifrequency MRE was applied to the midbrain of healthy and EAE mice of both sexes to quantitatively map regional stiffness. To define differences in brain ECM composition, the gene expression of the key basement membrane components laminin (*Lama4*, *Lama5*), collagen (*Col4a1*, *Col1a1*), and fibronectin (*Fn1*) were investigated by RT-qPCR. We showed that the healthy male cortex expressed less *Lama4*, *Lama5*, and *Col4a1*, but more *Fn1* (all $p < 0.05$) than the healthy female cortex, which was associated with 9% softer properties ($p = 0.044$) in that region. At peak EAE cortical softening was similar in both sexes compared to healthy tissue, with an 8% difference remaining between males and females ($p = 0.006$). Cortical *Lama4*, *Lama5* and *Col4a1* expression increased 2 to 3-fold in EAE in both sexes while *Fn1* decreased only in males (all $p < 0.05$). No significant sex differences in stiffness were detected in other brain regions. In conclusion, sexual dimorphism in the ECM composition of cortical tissue in the mouse brain is reflected by in vivo stiffness measured with MRE and should be considered in future studies by sex-specific reference values.



Citation: Batzdorf, C.S.; Morr, A.S.; Bertalan, G.; Sack, I.; Silva, R.V.; Infante-Duarte, C. Sexual Dimorphism in Extracellular Matrix Composition and Viscoelasticity of the Healthy and Inflamed Mouse Brain. *Biology* **2022**, *11*, 230. <https://doi.org/10.3390/biology11020230>

Academic Editor: Xinhua Shu

Received: 17 December 2021

Accepted: 28 January 2022

Published: 31 January 2022

Publisher's Note: MDPI stays neutral with regard to jurisdictional claims in published maps and institutional affiliations.



Copyright: © 2022 by the authors. Licensee MDPI, Basel, Switzerland. This article is an open access article distributed under the terms and conditions of the Creative Commons Attribution (CC BY) license (<https://creativecommons.org/licenses/by/4.0/>).

Keywords: multiple sclerosis; experimental autoimmune encephalomyelitis; sexual dimorphism; brain viscoelasticity; magnetic resonance elastography; extracellular matrix; cerebral cortex; neuroinflammation; basement membrane

1. Introduction

Multiple Sclerosis (MS) is a chronic inflammatory demyelinating disease of the central nervous system (CNS) affecting approximately 2.8 million people worldwide [1]. It displays a prominent sexual dimorphism in relation to susceptibility, incidence, pathology, and progression [2]. In women, the risk of MS is three times higher than in men, with disease onset occurring at earlier ages, but, generally, with slower progression [3–8]. While the higher susceptibility in women is associated with sex hormones and a differential immune response to inflammation, worsened progression in men is linked to enhanced neurodegeneration [2,7,9]. Moreover, MS incidence in women has been increasing over the last decades probably due to a sex-dependent response to environmental and lifestyle factors [5,6], with a current estimated female to male ratio of 2–4:1 [1,10].

The mechanical properties of the brain investigated by magnetic resonance elastography (MRE) also display sex differences. MRE is a non-invasive method that, based on the induction of shear waves through harmonic vibrations, allows the assessment of viscoelastic properties of the brain tissue *in vivo* [11]. MRE of healthy individuals showed that male brains were softer than female brains [12–14]. In response to inflammation, however, the brains of female MS patients exhibited stronger reduction in viscoelasticity compared to age-matched healthy males [12,15,16]. Similarly, in the MS mouse model, experimental autoimmune encephalomyelitis (EAE), we previously demonstrated a reduction in brain stiffness in sick mice [17–19]. This softening behavior seemed to be associated with inflammatory processes such as immune cell infiltration, demyelination, and loss of the blood–brain barrier (BBB) integrity, as well as remodeling of the extracellular matrix (ECM) [18–21]. We also recently showed that brain viscoelastic properties seem to be particularly dependent on ECM organization and axonal structure [22].

Furthermore, in MS, the ECM composition at lesion sites appears to be altered. Active lesions are marked, among others, by the deposition of fibronectin, correlating with BBB disruption and the accumulation of laminin and collagen type IV in the basement membrane and perivascular cuffs [18,23,24]. Moreover, it has been reported that estrogen can influence the production of matrix metalloproteinases [25,26], indicating that the degradation of ECM components may be influenced by sex.

Laminins, collagens, and fibronectin are mainly found in the ECM of the basement membrane in the brain and play an important role in the regulation of the BBB integrity [27]. Furthermore, collagen type I provides tensile strength and stiffness, while collagen type IV is responsible for flexible networks [28]. However, how sex-specific differences influence neuroinflammatory remodeling of the ECM and, consequently, viscoelastic brain properties, remains unclear.

Therefore, the aim of this study was to investigate sex effects on brain viscoelasticity in healthy and EAE mice via multifrequency MRE, which allows the accurate analysis of small cerebral regions [29], and to analyze sexual dimorphism in the remodeling of brain ECM.

2. Materials and Methods

2.1. Animals and EAE Model

All animal experiments were approved by the Berlin State Office for Health and Social Affairs (LAGeSo, G106/19) and conducted in strict adherence to the European guidelines for the care and use of laboratory animals under directive 2010/63/EU of the European Parliament and of the Council of 22 September 2010.

SJL mice that were 10–15 weeks old (Janvier, SAS, Le Genest Saint Isle, France), and are known for exhibiting sex-dependent susceptibility to EAE induction [30,31], were

investigated. The mice were housed under standard conditions with a 12:12h light–dark-cycle and ad libitum access to food and water. The four experimental groups consisted of female healthy ($n = 14$), male healthy ($n = 14$), female EAE ($n = 23$) and male EAE ($n = 19$) mice. To induce EAE, the animals were immunized with 250 μg of proteolipid peptide PLP_{139–151}, emulsified in 100 μL complete Freund’s adjuvant (Thermo Fisher Scientific, Waltham, MA, USA) and 800 μg Mycobacterium tuberculosis H37Ra (Difco, Detroit, MI, USA). Furthermore, 250 ng of pertussis toxin (List Biological Laboratories, Campbell, CA, USA) resuspended in phosphate-buffered saline (PBS) (Gibco, Grand Island, NY, USA) was injected intraperitoneally on day 0 and day 2 after immunization. Mice were monitored daily for clinical signs and scored as follows: 0.5—tail paresis or weak righting reflex; 1—tail plegia or tail paresis and weak righting reflex; 1.5—tail plegia and weak righting reflex; 2.0—additional hind limb paresis; 3.0—paraplegia; 4.0—additional forelimb paresis; 5.0—moribund or dead animal. To comply with animal welfare guidelines, all mice with a score higher than 3 were euthanized and removed from the study ($n_{\text{female}} = 2$, $n_{\text{male}} = 1$). The EAE model using SJL mice has been shown to be more suitable for cerebral MRE studies than EAE in C57BL/6, since PLP-induced EAE in SJL consistently leads to the development of brain lesions and to elasticity alterations in brain structures [17–19,32,33].

2.2. MRE Acquisition

MRE acquisition was performed on a preclinical 7 Tesla MRI scanner (BioSpec, Bruker, Ettlingen, Germany) operated with ParaVision 6.1 software (Bruker, Billerica, MA, USA) using a 20-mm diameter 1H-RF quadrature volume coil (RAPID Biomedical, Rimpar, Germany). The set up was similar to that previously described [19,29]. EAE mice were scanned based on their individual score at the peak of disease around day 10–12 after immunization. Age-matched healthy control mice were scanned on the same experimental days. To this end, mice were placed on a custom-built animal holder and anesthetized with 1.5–2.0% isoflurane in 30% O₂ and 70% N₂O by mask under continuous respiratory monitoring, using a pressure-sensitive pad placed on the dorsal thorax (Small Animal Instruments Inc., Stony Brook, NY, USA). Body temperature was monitored using a rectal probe and kept constant by circulating warm water through pads integrated in the animal holder. External vibrations were created by a custom-made driver system, using a non-magnetic piezoceramic actuator, and translated to the skull via a transducer rod to the head cradle of the mouse to induce shear waves in the brain [19]. Multifrequency single-shot MRE was conducted by consecutively exciting five external vibrational frequencies (1000, 1100, 1200, 1300, and 1400 Hz) which were encoded by a single-shot EPI sequence. Seven coronal slices with a slice thickness of 0.8 mm and a 0.18 mm \times 0.18 mm spatial resolution were acquired. The covered brain region was consistent with previous MRE studies [19,29], which facilitated the comparison of values. Further imaging parameters were TA = 9 min, TE = 53 ms, TR = 4000 ms, FOV = 16.2 mm \times 10.8 mm, and matrix size = 90 \times 60.

2.3. Data Reconstruction

Multifrequency MRE data were reconstructed using the tomoelastography post-processing pipeline, as described previously [29]. Viscoelasticity parameter maps were obtained based on shear wave speed c (in m/s), as a marker for tissue stiffness, and phase angle φ (in rad, also denoted as loss angle of the complex shear modulus), as a marker of tissue fluidity. Regions of interest (cerebral cortex, hippocampus, thalamic area, whole coronal midbrain slice) were defined manually, according to anatomical structures in a blinded fashion using MATLAB (Version 9.4 (R2018a). The MathWorks Inc.; 2018, Natick, MA, USA). Due to technical errors, $n_{\text{male naive}} = 1$ had to be excluded from the MRE analysis.

2.4. Tissue Processing

Animals were sacrificed directly after the MRE measurements with an overdose of ketamine (Inresa Arzneimittel GmbH, Freiburg im Breisgau, Germany) and xylazine (CP-Pharma, Burgdorf, Germany) followed by cardiac perfusion with PBS (Gibco, Grand

Island, NY, USA). The brains were extracted and one hemisphere was preserved in 4% paraformaldehyde (PFA) (Carl Roth, Karlsruhe, Germany) overnight at 4 °C, following dehydration in 30% sucrose at 4 °C. Afterwards, the tissue was embedded in O.C.T. (Sakura Finetek, Tokyo, Japan) and stored at −80 °C until preparation for histological staining. From the other half of the brain, the cerebral cortex and hippocampus were carefully extracted under a microscope, then freeze-dried in liquid nitrogen and stored at −80 °C for gene expression analysis. Post-MRE tissue processing was performed on a subgroup of animals ($n_{\text{female naive}} = 6$, $n_{\text{male naive}} = 6$, $n_{\text{female EAE}} = 6$, $n_{\text{male EAE}} = 7$).

2.5. Gene Expression Analysis

RNA was extracted from the hippocampus and the cerebral cortex using the Quick-RNA-MiniPrep Kit (Zymo Research, Irvine, CA, USA), and cDNA synthesis was carried out with the High-Capacity cDNA Reverse Transcription Kit (Thermo Fisher Scientific, USA), according to the manufacturer's instructions. Quantitative RT-PCR was performed with the QuantStudio 6 Flex Real-Time PCR system (Thermo Fisher Scientific, USA) using TaqMan® probes for the following genes: *Lama4*, *Lama5*, *Col4a1*, *Col1a1*, and *Fn1* (Thermo Fisher Scientific, USA; Supplementary Table S1). *Hprt1* served as the endogenous reference [34,35]. Collagens (*Col4a1*, *Col1a1*) provide fibrillar and net-like structures [28], while laminins (*Lama4*, *Lama5*) and fibronectin (*Fn1*), which are glycoproteins, are important for cellular attachment to the matrix [36,37] and influence collagen organization [38]. Therefore, we considered these proteins to be important regulators of the mechanical properties of the brain ECM.

2.6. Histology

For immunofluorescence staining the tissue was cut into 6 µm slices, thawed, fixed with 4% PFA for 15 min and then blocked with PBS containing 8% horse serum (Gibco, USA), 3% bovine serum albumin (Sigma-Aldrich, Darmstadt, Germany) and 1% Triton TM X-100 (Thermo Fisher Scientific, USA) for one hour at room temperature. Sections were then incubated overnight with the primary antibodies at 4 °C, diluted in PBS containing 20% blocking solution. As primary antibodies, we used mouse anti-fibronectin, 1:400 (Novus Biologicals, 2755-8, Littleton, CO, USA), rabbit monoclonal anti-collagen IV (EPR22911-127), 1:400 (Abcam, ab236640, Cambridge, UK) and rat monoclonal anti-CD3 (17A2), 1:100 (Invitrogen, 14-0032-82, Carlsbad, CA, USA). On the following day, sections were incubated with secondary antibodies: anti-rat, anti-mouse, and anti-rabbit, conjugated with Alexa-Fluor 488 or 568, 1:500 (Invitrogen, Carlsbad, CA, USA) for one hour at room temperature and counterstained with 4',6-diamidino-2-phenylindole (DAPI) at 1:10,000. Images were acquired at 20 times magnification with the Keyence Fluorescence Microscope BZ-X800 (Keyence Corporation, Osaka, Japan).

2.7. Statistical Analysis

Analyses were performed using GraphPad Prism 9.3 (GraphPad Software, La Jolla, CA, USA) with significance levels defined as * $p < 0.05$, ** $p < 0.01$, *** $p < 0.001$. All p -values below 0.1 are reported. Statistical group comparison was performed with an unpaired two-tailed t test, or with two-way analysis of variance (ANOVA) with post-hoc pairwise comparisons where appropriate. Values are reported with means, standard deviation (SD) and a 95% confidence interval (CI). Graphs are reported with means and a 95% CI.

3. Results

3.1. Sex-Specific Viscoelastic Properties of Healthy Mouse Brain

To determine sex differences in the brain's mechanical properties, the viscoelasticity of healthy female (♀) and male (♂) midbrains were compared. The predefined regions of interest were averaged for mean values of shear wave speed c (in m/s) and fluidity ϕ (in rad). Representative MRE parameter maps for the whole midbrain slice covering the cortex, hippocampus, and thalamus are depicted in Figure 1.

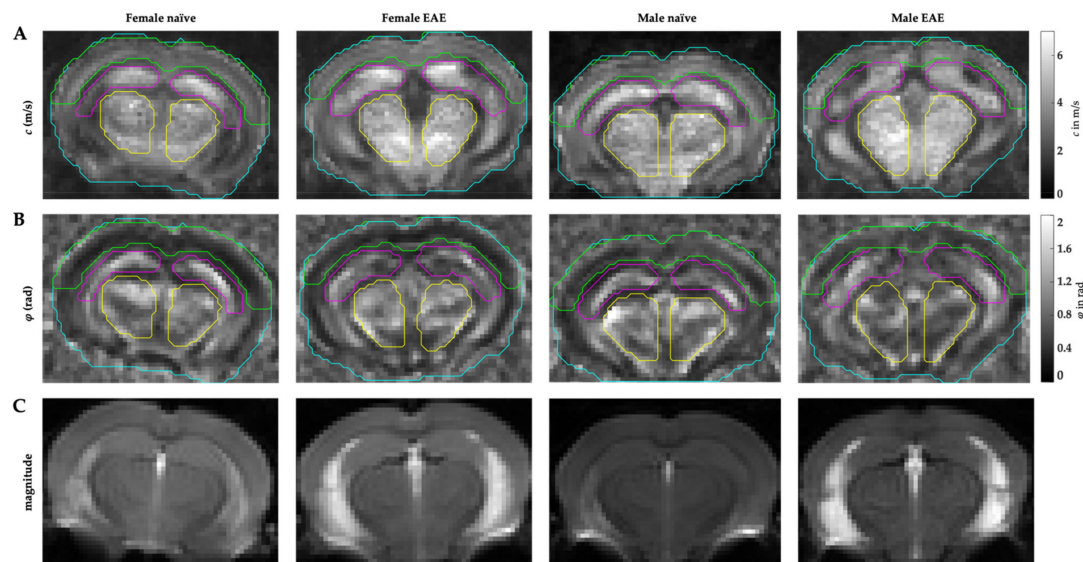


Figure 1. Representative parameter maps of the coronal murine midbrain with defined regions of interest in female/male naïve and female/male EAE. (A) stiffness maps in c (m/s), (B) fluidity-maps in φ (rad), (C) anatomical magnitude images (arbitrary units). Cyan = whole midbrain, green = cerebral cortex, magenta = hippocampus, yellow = thalamic area.

No differences in c or φ were observed when comparing the whole midbrain area of males and females (Figure 2A,B). However, sex became an important variable when considering the cortical viscoelasticity, which was on average 9% softer in males than in healthy age-matched females (mean $c_{\text{female}} = 2.90 \pm 0.33$ m/s, 95%CI 2.71–3.09 m/s; mean $c_{\text{male}} = 2.65 \pm 0.29$ m/s, 95%CI 2.63–2.78 m/s; $p = 0.044$). No sex-related differences in c or φ for the hippocampus or the thalamic area were detected.

3.2. Differences in Extracellular Matrix Composition in the Healthy Brain of Males and Females

Gene expressions of laminins (*Lama5* and *Lama4*), collagens (*Col4a1* and *Col1a1*), and fibronectin (*Fn1*) were quantified in the cerebral cortex and hippocampus as a control region in healthy male ($n = 6$) and age-matched female ($n = 6$) mice. Figure 3 represents relative gene expression levels in healthy males compared to females. Laminin and collagen type IV expression was significantly lower in the male cortex than in the female one (*Lama5* – 4.0-fold, $p = 0.019$; *Lama4* – 3.4-fold, $p = 0.006$; *Col4a1* – 1.6-fold, $p = 0.029$), while collagen type I expression did not present sexual dimorphism (Figure 3A). In contrast, a higher expression of fibronectin was found in the cortex of healthy males (*Fn1* 1.9-fold, $p = 0.002$). No differences related to sex were observed in the hippocampus (Figure 3B).

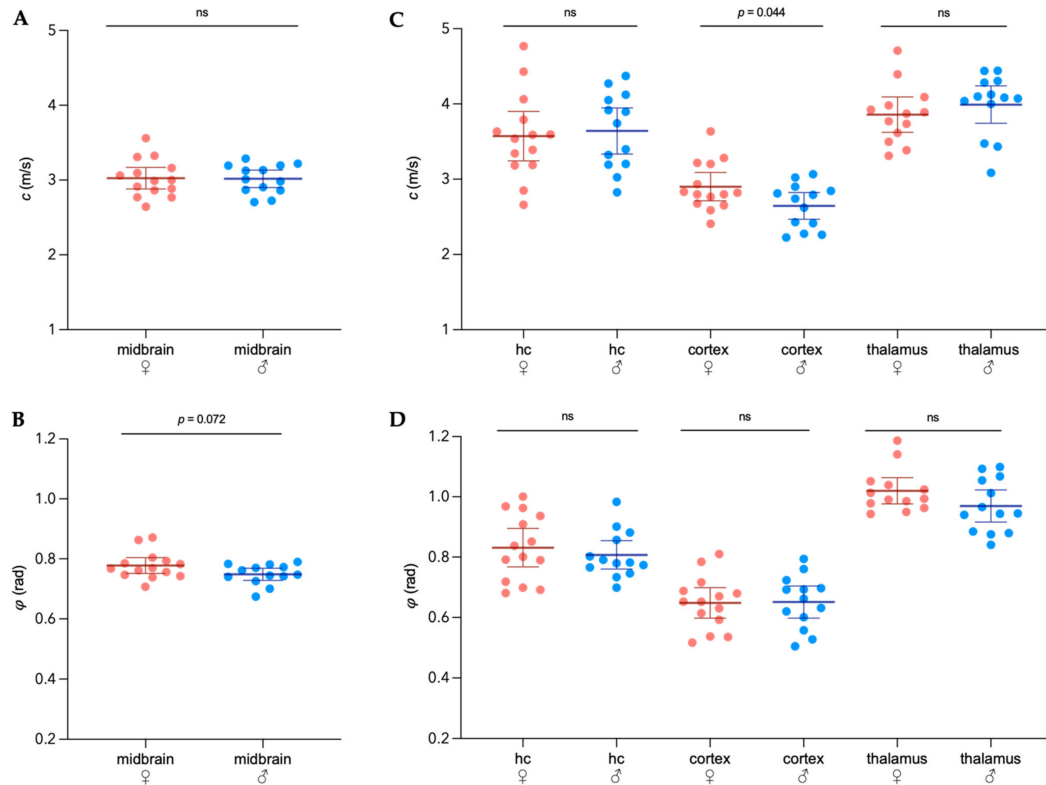


Figure 2. Sexual dimorphism in viscoelastic properties of healthy adult mouse brains. Mean shear wave speed c in m/s (A) and fluidity ϕ in rad (B) in the whole coronal section of the midbrain of female and male mice. (C) Regional analysis of stiffness (c) between sexes in the cortex, hippocampus, and thalamus. (D) Regional assessment of fluidity (ϕ). $n_{\text{female}} = 14$, $n_{\text{male}} = 13$, hc = hippocampus; representation of individual data points with mean and 95% CI. Group comparison performed by t test. ns = not significant.

3.3. Sex-Specific Changes of Brain Viscoelastic Properties during EAE

Next, we investigated whether viscoelasticity changes of the brain following inflammation revealed a sexual dimorphism. For that, data from healthy mice were compared with a cohort of female and male mice at the peak EAE ($n_{\text{female}} = 21$, mean score = 2.3; $n_{\text{male}} = 18$, mean score = 2.3).

Only the male EAE group showed a 5% global reduction of stiffness in the midbrain ($c_{\text{male naive}} = 3.02 \pm 0.19$ m/s, 95%CI 2.90–3.13 m/s; $c_{\text{male EAE}} = 2.86 \pm 0.15$ m/s, 95%CI 2.78–2.93 m/s; $p = 0.024$) when averaging the whole coronal section, while fluidity remained unaltered (Figure 4A). In the hippocampus, no significant stiffness changes were observed at peak EAE in both sexes, although a trend could be seen for male EAE.

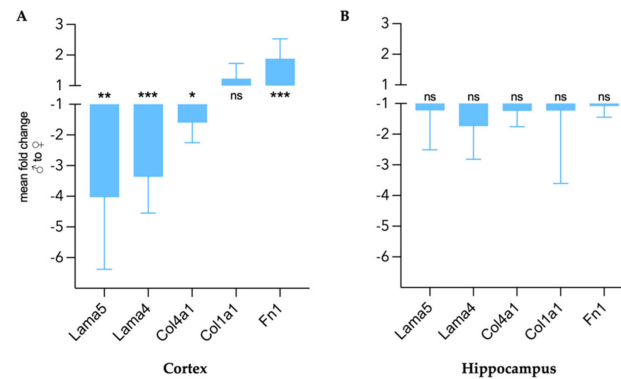


Figure 3. Sex differences in gene expression of ECM components in healthy cerebral cortex (A) and hippocampus (B) expressed as mean fold change of male gene expression compared to female with 95% CI. $n_{\text{female}} = 6$, $n_{\text{male}} = 6$. Group comparison performed with unpaired *t* test with Welch correction. *Lama5* = laminin $\alpha 5$, *Lama4* = laminin $\alpha 4$, *Col4a1* = collagen type IV α , *Col1a1* = collagen type I $\alpha 1$, *Fn1* = fibronectin 1. * $p < 0.05$, ** $p < 0.01$, *** $p < 0.001$, ns = not significant.

When considering different brain regions, the elasticity of the cortex was the most affected during EAE. We detected a 7% reduction for female and 6% for male mice when compared with age-matched control mice ($c_{\text{female naive}} = 2.90 \pm 0.33$ m/s, 95%CI 2.71–3.09 m/s; $c_{\text{female EAE}} = 2.70 \pm 0.16$ m/s, 95%CI 2.63–2.78 m/s; $p = 0.013$; $c_{\text{male naive}} = 2.65 \pm 0.29$ m/s, 95%CI 2.63–2.78 m/s; $c_{\text{male EAE}} = 2.49 \pm 0.12$ m/s, 95%CI 2.43–2.55 m/s; $p = 0.067$). The comparison between sexes revealed, however, no sex-related differences in the overall cortical softening during inflammation. The male EAE cortex was approximately 8% softer than the female EAE cortex ($p = 0.006$), maintaining the sex-dependent difference in stiffness observed in healthy mice (Figure 4B, center). In the thalamus, no inflammation-related changes of the mechanical properties were observed (Figure 4B, right). In both sexes, regional fluidity was not affected by EAE (Supplementary Figure S1).

3.4. Extracellular Matrix Remodeling in Female and Male EAE Brains

To assess inflammation-induced changes of the ECM components that appeared to be differentially expressed in male and female tissues, we investigated the gene expression levels of laminins, collagen type I and IV and fibronectin in the cerebral cortex and hippocampus of healthy and EAE mice. As shown in Figure 5A and Table 1, at peak EAE, the cortical expression of *Lama4* and *Lama5* increased similarly in both sexes (all $p < 0.05$). Given the baseline differences between healthy animals, their expression remained significantly higher in the female EAE group compared to the male (*Lama5* 3.85-fold, *Lama4* 3.86-fold, all $p < 0.001$) (Table 1). However, for *Col4a1* we observed a 3.0-fold increase in the cortex in female EAE and 2.0-fold in male EAE (all $p < 0.01$) in comparison to the respective healthy group, augmenting the initial sex difference from 1.6-fold in healthy mice to 2.38-fold ($p < 0.001$) in EAE. In addition, a decreased expression of *Col1a1* (−2.1-fold, $p < 0.001$) and *Fn1* (−1.4-fold, $p = 0.018$) was observed in the male cortex.

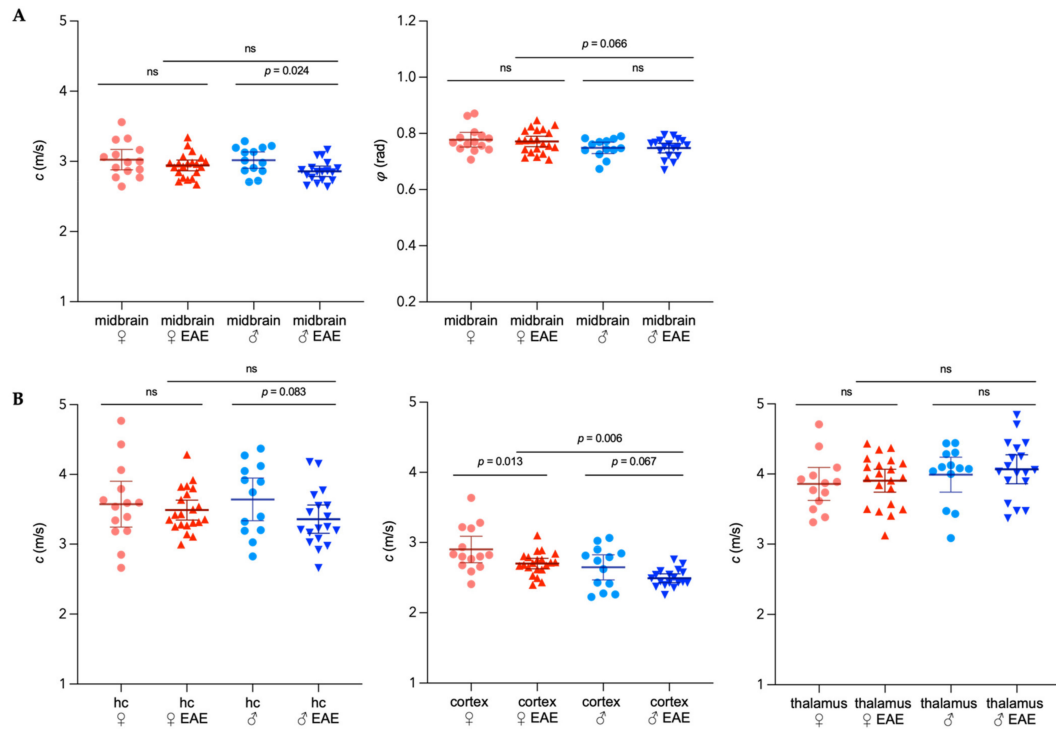


Figure 4. Sex-specific viscoelastic properties of the mouse brain in healthy conditions and EAE. (A) Shear wave speed c in m/s and fluidity ϕ in rad in the whole coronal midbrain. (B) Regional distribution of c in the hippocampus (hc), cortex and thalamic area; light red = healthy female; dark red = EAE female; light blue = healthy male; dark blue = EAE male. Representation of individual data points with mean and 95%CI. $n_{female\ naive} = 14$, $n_{male\ naive} = 13$, $n_{female\ EAE} = 21$, $n_{male\ EAE} = 18$. Two-way ANOVA with Fisher’s LSD post-hoc comparisons. ns = not significant.

Table 1. Sex-specific fold changes in gene expression of ECM components in EAE compared to healthy and between EAE in cortex and hippocampus.

Gene	Cortex			Hippocampus		
	♀ EAE/Naive	♂ EAE/Naive	EAE ♂/♀	♀ EAE/Naive	♂ EAE/Naive	EAE ♂/♀
<i>Lama5</i>	2.91	3.04	−3.85	1.83	−1.08	−2.42
<i>Lama4</i>	3.10	2.70	−3.86	1.08	1.11	−1.69
<i>Col4a1</i>	2.99	2.01	−2.38	−1.51	−1.37	−1.12
<i>Col1a1</i>	−1.29	−2.12	−1.34	−2.07	−1.33	1.26
<i fn1<="" i=""></i>	1.12	−1.43	1.18	−1.19	1.14	1.24

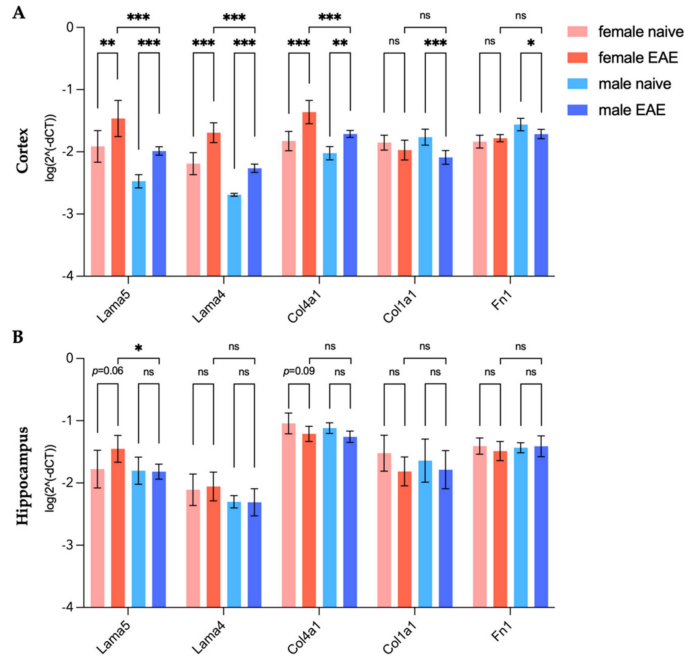


Figure 5. Sex-specific gene expression of ECM targets in healthy and EAE mice in the cortex (A) and hippocampus (B) relative to endogenous reference *Hprt1*. Representation of mean log²(-ΔCT) with 95% CI. $n_{\text{female naive}} = 6$, $n_{\text{male naive}} = 6$, $n_{\text{female EAE}} = 6$, $n_{\text{male EAE}} = 7$. Two-way ANOVA with Tukey's post-hoc comparisons. * $p < 0.05$, ** $p < 0.01$, *** $p < 0.001$, ns = not significant.

In the hippocampus (Figure 5B), we observed mild effects of inflammation on the expression of the selected ECM-components. *Lama5* expression remained unaltered for males at peak EAE, but increased 1.83-fold in females ($p = 0.064$), leading to a significant 2.41-fold difference ($p = 0.025$) between the sexes in the disease state (Figure 5B). Other investigated genes did not show any significant changes in the hippocampus regarding disease status or sex.

To visualize the ECM remodeling in both sexes and confirm the gene expression data, we performed representative immunohistological stainings in the cerebral cortex of two of our targets, fibronectin and collagen type IV. A representative cortical image of each group is shown in Figure 6. Collagen type IV was present around vessel-like structures, resembling the formation of the endothelial basement membranes (Figure 6A). Corroborating gene expression data, an upregulation of collagen type IV was observed in EAE mice for both sexes, compared to their corresponding healthy controls, with especially pronounced expression in female EAE. Similarly, fibronectin was also present in vessel-like structures, as demonstrated in Figure 6B. Interestingly, in healthy males, fibronectin appeared widely distributed around cell bodies.

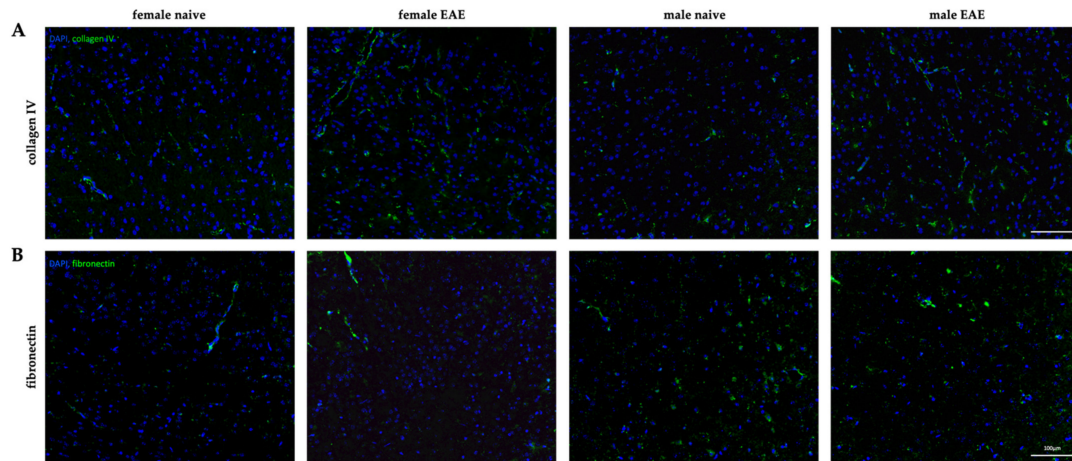


Figure 6. Sexual dimorphism in cortical ECM remodeling in EAE. (A) Immunofluorescence of collagen type IV (green) in healthy condition (naive) and at peak EAE for female (left) and male (right) cortices. (B) Cortical fibronectin (green) staining of female (left) and male (right) healthy and EAE mice. DAPI (blue). 20× magnification. Scale: 100 μm.

Additionally, to investigate whether ECM remodeling was associated with the presence of leukocyte infiltration, the cortical tissue was stained for CD3 to identify perivascular infiltrates in the cerebral cortex. Only one out of five male EAE mice presented a cortical perivascular lesion, and no leukocyte infiltrate was detected in females (Supplementary Figure S2). This indicates that the observed changes affecting elasticity and ECM composition in EAE were not related to acute lesion formation but diffuse inflammatory events.

4. Discussion

In this study, we built on our previous work on ECM alterations during neuroinflammation investigated by MRE, and further focused on sexual dimorphism, which potentially affects ECM composition and brain viscoelasticity. Our data provided evidence of sexual dimorphism in the ECM of cortical tissue, namely with respect to basement membrane proteins that may directly impact tissue structure or, as a result of the local inflammatory process, indirectly contribute to the observed divergence in tissue stiffness and the response to neuroinflammation.

Using MRE, we demonstrated here, for the first time, that the murine healthy brain exhibits sex-dependent differences in mechanical properties. Stiffness differences seem to primarily affect the cerebral cortex, as the male healthy cortex was, on average, 9% softer than the female one. This data is in line with previous MRE studies in humans that indicated significant sex differences in healthy brain viscoelasticity, with male brains being 9 to 11% softer, on average [12,13].

Furthermore, we demonstrated a significantly higher expression of laminin and collagen type IV in the healthy female cortex, while fibronectin was about two times more expressed in the male cerebral cortex than in the female cortex. Laminin, collagen type IV, and fibronectin are predominantly located within the basement membrane of CNS tissue [23,27]. Since these components have been shown to have relevant mechanical features [28,39–46] (extensively reviewed by [47–49]), our results indicate that differences in the constitution of the basement membrane may have an impact on cortical stiffness in a sex-specific manner.

In this line, sexual dimorphism has been reported in non-neuronal ECM, such as in tendons or vocal folds [50,51]. Moreover, estradiol and testosterone have been reported

to have a differential effect on fibronectin synthesis depending on the investigated cells, which is in agreement with our results on the high fibronectin to collagen ratio in the male cortex [52]. Likewise, collagen turnover seems to exhibit a strong sex-dependence across the lifespan, with pronounced changes in women around menopause [53], and the connection between collagen content in the skin and circulating estrogen levels is well established [54]. Nonetheless, we cannot exclude that cellular differences between the female and male cortex may have contributed to the observed sex-specific disparity in stiffness. Studies in stroke models suggest a correlation between stiffness and neuronal cell count [55], which has been shown to differ between sexes [56]. While men seem to have more cortical neurons, female cerebral cortices show considerably larger neuropil [56,57]. On the other hand, cellular composition directly influences ECM configuration regarding its components, as well as post-translational processing such as cross-linking [28] which, then again, influences mechanical properties [41] and thereby cannot be considered as an independent variable.

No sex-specific differences in viscoelastic properties of the hippocampus were observed in our study, although more microglia and astrocytes are present in the dentate gyrus of female mice [58], while the neuronal density in the same area seems to be higher in males [59]. In addition, we did not observe differences in viscoelastic properties of the thalamus, which is in line with previous data in humans that showed no sexual dimorphism in the deep gray area [14]. Nonetheless, future studies should address possible viscoelastic changes in thalamic subregions. This will be of particular interest since the lateral posterior nucleus, the mouse homologue for the human pulvinar nucleus, has been shown to be functionally connected to cortical areas including auditory, visual, and somatosensory cortices [60,61] and to present sex-dependent differences in connectivity [62].

Under neuroinflammatory conditions, we observed a mild effect in females and a significant softening of the midbrain of 5% in male EAE, although previous studies reported a global softening in female EAE brains [17–19] as well as for MS patients of both sexes [12]. This discrepancy could be explained by the limitation of the analyzed region, which was restricted to a single coronal slice, and did not cover the usually affected cerebellum or optic nerve [63,64]. Another factor to consider when comparing these results with our previous MRE studies [17–19,32] is our current focus on regional viscoelasticity values based on multifrequency inversion, which allows a higher resolution, and is therefore more sensitive to regional alterations, as studies in human subjects have shown [65–67].

When assessing regional mechanical properties, both female and male mice showed a similar degree of cortical softening during EAE. In both sexes, inflammation led to reduced stiffness, resulting in an 8% softer cortex in males than females in EAE, which is similar to the intersexual difference of 9% observed in healthy mice. No significant effects of inflammation on tissue elasticity were observed for the other investigated regions. Thus, multifrequency MRE revealed the murine cortex as the brain region with the largest sex-specific variation in stiffness under normal and neuroinflammatory conditions.

Interestingly, this effect was reflected by the gene expression of main proteins forming the ECM basement membrane, which presented pronounced sex differences in the cortex, and almost none in the hippocampus. In the cerebral cortex, both female and male EAE showed significantly higher expression of laminins and collagen type IV compared to healthy mice. This is in coherence with previous work on glial scars, attributing tissue softening to the enhanced expression of laminin and collagen type IV [68]. However, our results also revealed higher laminin and collagen expression in the healthy female cortex compared to the softer healthy male cortex. Nonetheless, previous work has indicated that tissue stiffness is intricately regulated by the interaction of cellular adhesion and matrix composition, providing seemingly paradoxical results when comparing healthy and pathological tissue properties [69]. Additionally, stiffness of collagen type IV has been shown to be dependent on the degree of crosslinking [41] which was not investigated here, and might explain the discrepancies between data in healthy and diseased tissue, since neuroinflammation triggers an increase in ECM degradation [70].

In both MS and EAE, deposition of basement membrane molecules associated with activated microglia in the vicinity of white matter lesions contribute to the disruption of the BBB integrity [23,24,71]. Our histological data support the elevated presence of collagen type IV around vessel-like structures in the cortex in EAE, while we did not observe perivascular leukocyte infiltration in that region. This is expected from peptide-induced EAE pathology, where inflammation mainly affects the spinal cord, cerebellum, and the optic nerve [63], and does not habitually lead to cortical lesions [64]. Pathological changes in the cortex are proposed to be directly related to spinal lesion formation via Wallerian degeneration [72], but are also highly dependent on meningeal inflammation with soluble factors leading to demyelination and neurodegeneration [73]. Therefore, we propose that the cortical changes observed here, which differ greatly from ECM remodeling described in white matter lesions [18,23], result from underlying meningeal and spinal inflammation rather than from the infiltration of leukocytes into the cortical parenchyma.

Obviously, alterations of the basement membrane cannot solely explain the elasticity changes observed in the cortical tissue, but could rather reflect the inflammatory, activated state of matrix-producing cells, such as astrocytes, oligodendrocyte precursor or endothelial cells [74]. It is reasonable to posit that stiffness changes result, at least partially, from the inflammatory state of these cells. Nonetheless, another relevant aspect that cannot be discarded, is the influence of basement membrane components on the interstitial matrix, the largest component of the brain ECM [75]. Since the interstitial matrix is in part constituted by laminins and collagens [27], it is possible that enhanced expression of such components at vascular sites leads to a partial diffusion into the parenchymal space [74]. These molecules could then interact with and alter the ECM of other compartments, such as the perineuronal matrix, resulting in a major structural effect contributing to the elastic changes here discussed.

The inflammation-induced upregulation of *Lama4* and *Lama5* was about 3-fold in both sexes. However, considering baseline differences, their expression was still about 4-fold higher in female EAE than in male EAE, demonstrating that the effect size of the inherent sex differences was larger than the observed inflammatory effect. In addition, we observed a downregulation of *Col1a1* and *Fn1* in EAE male cortices. The histological correlates showed a reduction of fibronectin in the inflamed male cortex compared to the healthy group, affecting not only the vasculature but also fibronectin in association with cortical nuclei. This is in contrast with previous research, which described the deposition of fibronectin in MS lesions [23,24] in association with perivascular infiltrates and tissue softening [18]. Given the absence of leukocyte infiltrates in the cortex, it is conceivable that cortical fibronectin and collagen type I levels were not increased, and may not have contributed to cortical softening. As most of our knowledge about neuroinflammatory ECM remodeling stems from white matter lesions [23], ECM changes in normal-appearing gray matter are still not well understood.

In addition, none of the investigated regions exhibited changes in tissue fluidity φ between naive and EAE mice of the same sex, which has been equally described in our previous studies in acute EAE [17–19,32]. Tissue fluidity is influenced by the motility of structure elements in the viscoelastic network [76] and, thus, seems to reflect cellular confinement [77]. This confinement is affected by the interaction and organization of macromolecular networks in the ECM [77,78]. Since we did not observe any changes in fluidity properties between healthy and EAE brains across all regions, we expect the complexity of the tissue architecture to be similar between sexes and not affected by inflammation.

Taken together, our data on the cortical remodeling of the ECM in the context of EAE suggests sex-specific processes. Sex-dependent changes in the expression levels of basement membrane proteins seem to have the same net effect on macroscopic viscoelastic properties of the cortex because we observed a similar amount of softening in both sexes. Since tissue stiffness depends on both the cellular and ECM composition, as well as their structural arrangement [19,22,41,55,68,79], the combination of up- and downregulation of different matrix components may counterbalance their effect on mechanical properties

and may even serve as a protective measure. Future studies with larger group sizes will allow for in-depth analyses of the individual contribution of matrix components to the viscoelastic behavior of the brain. Furthermore, as viscoelastic matrix properties have been shown to strongly influence neuronal and astrocytic growth as well as the differentiation of oligodendrocytes [80–82], it remains to be determined how the absolute sex differences in cortical stiffness affect cellular behavior and remyelination in EAE.

5. Conclusions

In conclusion, by applying multifrequency MRE we were able to demonstrate, for the first time, significant sex differences in viscoelastic properties of the cortex of healthy and EAE mice. Softening was not associated with lesion formation but with ECM remodeling, as reflected by the gene expression changes observed for collagen type IV, laminin, and fibronectin. Understanding sexual dimorphism in the composition of the ECM is important in neurobiology, and might help understand sex-dependent responses to environmental factors, as well as provide guidance for the development of individualized treatments of MS. Moreover, possible implications of sex-specific mechanical properties on the cellular behavior in neuroinflammatory conditions need to be investigated. Regarding future imaging studies, sex-specific reference values for MRE in MS should be established.

Supplementary Materials: The following are available online at <https://www.mdpi.com/article/10.3390/biology11020230/s1>, Figure S1: Regional distribution of sex-specific fluidity φ in the midbrain of the mouse in healthy and EAE. Figure S2: Singular cortical lesion in the midbrain in male EAE. Table S1: Gene symbols and corresponding primers for TaqMan® assays.

Author Contributions: Conceptualization, C.I.-D., C.S.B. and R.V.S.; methodology, C.S.B., R.V.S. and A.S.M.; software, C.S.B. and A.S.M.; validation, C.S.B., R.V.S. and A.S.M.; formal analysis, C.S.B.; investigation, C.S.B., R.V.S. and A.S.M.; resources, C.I.-D. and I.S.; data curation, C.S.B.; writing—original draft preparation, C.S.B.; writing—review and editing, R.V.S., C.I.-D., A.S.M., I.S. and G.B.; visualization, C.S.B.; supervision, R.V.S. and C.I.-D.; project administration, C.S.B.; funding acquisition, C.I.-D., I.S. and C.S.B. All authors have read and agreed to the published version of the manuscript.

Funding: The work was funded by the German Research Foundation, SFB1340-1 “Matrix in Vision” project B05, the nonprofit Hertie foundation (P1190047 to C.S.B and C.I.D) and the Research Training Group GRK2260 BIOQIC.

Institutional Review Board Statement: This study was approved by the Berlin State Office for Health and Social Affairs (LAGeSo, G106/19) and conducted in strict adherence to the European guidelines for the care and use of laboratory animals under directive 2010/63/EU of the European Parliament and of the Council of 22 September 2010.

Informed Consent Statement: Not applicable.

Data Availability Statement: The raw data supporting the conclusions of this article are available upon request from the corresponding author.

Acknowledgments: The authors thank Philipp Boehm-Sturm and Susanne Mueller from the Department of Experimental Neurology, Center for Stroke Research and the NeuroCure Cluster of Excellence, Charité Core Facility 7T Experimental MRIs at the Charité - Universitätsmedizin Berlin, Germany, for the support with the MRE experiments.

Conflicts of Interest: The authors declare no conflict of interest. The funders had no role in the design of the study; in the collection, analyses, or interpretation of data; in the writing of the manuscript, or in the decision to publish the results.

References

1. *The Multiple Sclerosis International Federation, Atlas of MS*, 3rd ed.; Multiple Sclerosis International Federation: London, UK, 2020.
2. Gilli, F.; DiSano, K.D.; Pachner, A.R. Sex Matters in Multiple Sclerosis. *Front. Neurol.* **2020**, *11*, 616. [[CrossRef](#)] [[PubMed](#)]
3. Bergamaschi, R. Prognostic Factors in Multiple Sclerosis. *Int. Rev. Neurobiol.* **2007**, *79*, 423–447. [[CrossRef](#)] [[PubMed](#)]
4. Voskuhl, R.R.; Patel, K.; Paul, F.; Gold, S.M.; Scheel, M.; Kuchling, J.; Cooper, G.; Assever, S.; Chien, C.; Brandt, A.U.; et al. Sex Differences in Brain Atrophy in Multiple Sclerosis. *Biol. Sex Differ.* **2020**, *11*, 49. [[CrossRef](#)]

5. Bove, R.; Chitnis, T. The Role of Gender and Sex Hormones in Determining the Onset and Outcome of Multiple Sclerosis. *Mult. Scler. J.* **2014**, *20*, 520–526. [[CrossRef](#)] [[PubMed](#)]
6. Dunn, S.E.; Gunde, E.; Lee, H. Sex-Based Differences in Multiple Sclerosis (MS): Part II: Rising Incidence of Multiple Sclerosis in Women and the Vulnerability of Men to Progression of This Disease. *Curr. Top. Behav. Neurosci.* **2015**, *26*, 57–86. [[CrossRef](#)] [[PubMed](#)]
7. Dunn, S.E.; Lee, H.; Pavri, F.R.; Zhang, M.A. Sex-Based Differences in Multiple Sclerosis (Part I): Biology of Disease Incidence. *Curr. Top. Behav. Neurosci.* **2015**, *26*, 29–56. [[CrossRef](#)]
8. Magyari, M. Gender Differences in Multiple Sclerosis Epidemiology and Treatment Response. *Dan. Med. J.* **2016**, *63*, B5212.
9. Golden, L.C.; Voskuhl, R. The Importance of Studying Sex Differences in Disease: The Example of Multiple Sclerosis. *J. Neurosci. Res.* **2017**, *95*, 633–643. [[CrossRef](#)]
10. Koch-Henriksen, N.; Sørensen, P.S. The Changing Demographic Pattern of Multiple Sclerosis Epidemiology. *Lancet Neurol.* **2010**, *9*, 520–532. [[CrossRef](#)]
11. Hiscox, L.V.; Johnson, C.L.; Barnhill, E.; McGarry, M.D.J.; Huston, J.; van Beek, E.J.R.; Starr, J.M.; Roberts, N. Magnetic Resonance Elastography (MRE) of the Human Brain: Technique, Findings and Clinical Applications. *Phys. Med. Biol.* **2016**, *61*, R401–R437. [[CrossRef](#)]
12. Wuerfel, J.; Paul, F.; Beierbach, B.; Hamhaber, U.; Klatt, D.; Papazoglou, S.; Zipp, F.; Martus, P.; Braun, J.; Sack, I. MR-Elastography Reveals Degradation of Tissue Integrity in Multiple Sclerosis. *NeuroImage* **2010**, *49*, 2520–2525. [[CrossRef](#)] [[PubMed](#)]
13. Sack, I.; Beierbach, B.; Wuerfel, J.; Klatt, D.; Hamhaber, U.; Papazoglou, S.; Martus, P.; Braun, J. The Impact of Aging and Gender on Brain Viscoelasticity. *NeuroImage* **2009**, *46*, 652–657. [[CrossRef](#)] [[PubMed](#)]
14. Arani, A.; Murphy, M.C.; Glaser, K.J.; Manduca, A.; Lake, D.S.; Kruse, S.A.; Jack, C.R.; Ehman, R.L.; Huston, J. Measuring the Effects of Aging and Sex on Regional Brain Stiffness with MR Elastography in Healthy Older Adults. *NeuroImage* **2015**, *111*, 59–64. [[CrossRef](#)] [[PubMed](#)]
15. Streitberger, K.-J.; Sack, I.; Krefting, D.; Pfüller, C.; Braun, J.; Paul, F.; Wuerfel, J. Brain Viscoelasticity Alteration in Chronic-Progressive Multiple Sclerosis. *PLoS ONE* **2012**, *7*, e29888. [[CrossRef](#)]
16. Fehlner, A.; Behrens, J.R.; Streitberger, K.-J.; Papazoglou, S.; Braun, J.; Bellmann-Strobl, J.; Ruprecht, K.; Paul, F.; Würfel, J.; Sack, I. Higher-Resolution MR Elastography Reveals Early Mechanical Signatures of Neuroinflammation in Patients with Clinically Isolated Syndrome. *J. Magn. Reson. Imaging JMRI* **2016**, *44*, 51–58. [[CrossRef](#)]
17. Riek, K.; Millward, J.M.; Hamann, I.; Mueller, S.; Pfueller, C.F.; Paul, F.; Braun, J.; Infante-Duarte, C.; Sack, I. Magnetic Resonance Elastography Reveals Altered Brain Viscoelasticity in Experimental Autoimmune Encephalomyelitis. *NeuroImage Clin.* **2012**, *1*, 81–90. [[CrossRef](#)]
18. Wang, S.; Millward, J.M.; Hanke-Vela, L.; Malla, B.; Pilch, K.; Gil-Infante, A.; Waiczies, S.; Mueller, S.; Boehm-Sturm, P.; Guo, J.; et al. MR Elastography-Based Assessment of Matrix Remodeling at Lesion Sites Associated With Clinical Severity in a Model of Multiple Sclerosis. *Front. Neurol.* **2019**, *10*, 1382. [[CrossRef](#)]
19. Silva, R.V.; Morr, A.S.; Mueller, S.; Koch, S.P.; Boehm-Sturm, P.; Rodriguez-Sillke, Y.; Kunkel, D.; Tzschätzsch, H.; Kühl, A.A.; Schnorr, J.; et al. Contribution of Tissue Inflammation and Blood-Brain Barrier Disruption to Brain Softening in a Mouse Model of Multiple Sclerosis. *Front. Neurosci.* **2021**, *15*, 701308. [[CrossRef](#)]
20. Schregel, K.; Wuerfel nee Tysiak, E.; Garteiser, P.; Gemeinhardt, I.; Prozorovski, T.; Aktas, O.; Merz, H.; Petersen, D.; Wuerfel, J.; Sinkus, R. Demyelination Reduces Brain Parenchymal Stiffness Quantified in Vivo by Magnetic Resonance Elastography. *Proc. Natl. Acad. Sci. USA* **2012**, *109*, 6650–6655. [[CrossRef](#)]
21. Weickenmeier, J.; de Rooij, R.; Budday, S.; Steinmann, P.; Ovaert, T.C.; Kuhl, E. Brain Stiffness Increases with Myelin Content. *Acta Biomater.* **2016**, *42*, 265–272. [[CrossRef](#)]
22. Guo, J.; Bertalan, G.; Meierhofer, D.; Klein, C.; Schreyer, S.; Steiner, B.; Wang, S.; Vieira da Silva, R.; Infante-Duarte, C.; Koch, S.; et al. Brain Maturation Is Associated with Increasing Tissue Stiffness and Decreasing Tissue Fluidity. *Acta Biomater.* **2019**, *99*, 433–442. [[CrossRef](#)] [[PubMed](#)]
23. Ghorbani, S.; Yong, V.W. The Extracellular Matrix as Modifier of Neuroinflammation and Remyelination in Multiple Sclerosis. *Brain* **2021**, *144*, 1958–1973. [[CrossRef](#)] [[PubMed](#)]
24. Van Horssen, J.; Dijkstra, C.D.; De Vries, H.E. The Extracellular Matrix in Multiple Sclerosis Pathology. *J. Neurochem.* **2007**, *103*, 1293–1301. [[CrossRef](#)] [[PubMed](#)]
25. Voskuhl, R.R.; Gold, S.M. Sex-Related Factors in Multiple Sclerosis Susceptibility and Progression. *Nat. Rev. Neurol.* **2012**, *8*, 255–263. [[CrossRef](#)] [[PubMed](#)]
26. Gold, S.M.; Sasidhar, M.V.; Morales, L.B.; Du, S.; Sicotte, N.L.; Tiwari-Woodruff, S.K.; Voskuhl, R.R. Estrogen Treatment Decreases Matrix Metalloproteinase (MMP)-9 in Autoimmune Demyelinating Disease through Estrogen Receptor Alpha (ERalpha). *Lab. Invest. J. Tech. Methods Pathol.* **2009**, *89*, 1076–1083. [[CrossRef](#)] [[PubMed](#)]
27. Lau, L.W.; Cua, R.; Keough, M.B.; Haylock-Jacobs, S.; Yong, V.W. Pathophysiology of the Brain Extracellular Matrix: A New Target for Remyelination. *Nat. Rev. Neurosci.* **2013**, *14*, 722–729. [[CrossRef](#)]
28. Miller, R.T. Mechanical Properties of Basement Membrane in Health and Disease. *Matrix Biol. J. Int. Soc. Matrix Biol.* **2017**, *57*–58, 366–373. [[CrossRef](#)]
29. Bertalan, G.; Guo, J.; Tzschätzsch, H.; Klein, C.; Barnhill, E.; Sack, I.; Braun, J. Fast Tomoelastography of the Mouse Brain by Multifrequency Single-Shot MR Elastography. *Magn. Reson. Med.* **2019**, *81*, 2676–2687. [[CrossRef](#)]

30. Teuscher, C.; Bunn, J.Y.; Fillmore, P.D.; Butterfield, R.J.; Zachary, J.F.; Blankenhorn, E.P. Gender, Age, and Season at Immunization Uniquely Influence the Genetic Control of Susceptibility to Histopathological Lesions and Clinical Signs of Experimental Allergic Encephalomyelitis. *Am. J. Pathol.* **2004**, *165*, 1593–1602. [[CrossRef](#)]
31. Papenfuss, T.L.; Rogers, C.J.; Gienapp, I.; Yurrita, M.; McClain, M.; Damico, N.; Valo, J.; Song, F.; Whitacre, C.C. Sex Differences in Experimental Autoimmune Encephalomyelitis in Multiple Murine Strains. *J. Neuroimmunol.* **2004**, *150*, 59–69. [[CrossRef](#)]
32. Millward, J.M.; Guo, J.; Berndt, D.; Braun, J.; Sack, I.; Infante-Duarte, C. Tissue Structure and Inflammatory Processes Shape Viscoelastic Properties of the Mouse Brain. *NMR Biomed.* **2015**, *28*, 831–839. [[CrossRef](#)] [[PubMed](#)]
33. Millward, J.M.; Ariza de Schellenberger, A.; Berndt, D.; Hanke-Vela, L.; Schellenberger, E.; Waiczies, S.; Taupitz, M.; Kobayashi, Y.; Wagner, S.; Infante-Duarte, C. Application of Europium-Doped Very Small Iron Oxide Nanoparticles to Visualize Neuroinflammation with MRI and Fluorescence Microscopy. *Neuroscience* **2019**, *403*, 136–144. [[CrossRef](#)] [[PubMed](#)]
34. Zamani, A.; Powell, K.L.; May, A.; Semple, B.D. Validation of Reference Genes for Gene Expression Analysis Following Experimental Traumatic Brain Injury in a Pediatric Mouse Model. *Brain Res. Bull.* **2020**, *156*, 43–49. [[CrossRef](#)] [[PubMed](#)]
35. Kang, Y.; Wu, Z.; Cai, D.; Lu, B. Evaluation of Reference Genes for Gene Expression Studies in Mouse and N2a Cell Ischemic Stroke Models Using Quantitative Real-Time PCR. *BMC Neurosci.* **2018**, *19*, 3. [[CrossRef](#)] [[PubMed](#)]
36. Bennisroune, A.; Romier-Crouzet, B.; Blaise, S.; Laffargue, M.; Efremov, R.G.; Martiny, L.; Maurice, P.; Duca, L. Elastic Fibers and Elastin Receptor Complex: Neuraminidase-1 Takes the Center Stage. *Matrix Biol. J. Int. Soc. Matrix Biol.* **2019**, *84*, 57–67. [[CrossRef](#)] [[PubMed](#)]
37. Culav, E.M.; Clark, C.H.; Merrilees, M.J. Connective Tissues: Matrix Composition and Its Relevance to Physical Therapy. *Phys. Ther.* **1999**, *79*, 308–319. [[CrossRef](#)] [[PubMed](#)]
38. Guarnieri, D.; Battista, S.; Borzacchiello, A.; Mayol, L.; De Rosa, E.; Keene, D.R.; Muscariello, L.; Barbarisi, A.; Netti, P.A. Effects of Fibronectin and Laminin on Structural, Mechanical and Transport Properties of 3D Collageneous Network. *J. Mater. Sci. Mater. Med.* **2007**, *18*, 245–253. [[CrossRef](#)]
39. Storm, C.; Pastore, J.J.; MacKintosh, F.C.; Lubensky, T.C.; Janmey, P.A. Nonlinear Elasticity in Biological Gels. *Nature* **2005**, *435*, 191–194. [[CrossRef](#)]
40. Li, H.; Zheng, Y.; Han, Y.L.; Cai, S.; Guo, M. Nonlinear Elasticity of Biological Basement Membrane Revealed by Rapid Inflation and Deflation. *Proc. Natl. Acad. Sci. USA* **2021**, *118*, e2022422118. [[CrossRef](#)]
41. Bhawe, G.; Colon, S.; Ferrell, N. The Sulfilimine Cross-Link of Collagen IV Contributes to Kidney Tubular Basement Membrane Stiffness. *Am. J. Physiol. Ren. Physiol.* **2017**, *313*, F596–F602. [[CrossRef](#)]
42. Pastor-Pareja, J.C.; Xu, T. Shaping Cells and Organs in Drosophila by Opposing Roles of Fat Body-Secreted Collagen IV and Perlecan. *Dev. Cell* **2011**, *21*, 245–256. [[CrossRef](#)] [[PubMed](#)]
43. Candiello, J.; Balasubramani, M.; Schreiber, E.M.; Cole, G.J.; Mayer, U.; Halfter, W.; Lin, H. Biomechanical Properties of Native Basement Membranes. *FEBS J.* **2007**, *274*, 2897–2908. [[CrossRef](#)] [[PubMed](#)]
44. Gould, D.B.; Phalan, F.C.; Breedveld, G.J.; van Mil, S.E.; Smith, R.S.; Schimenti, J.C.; Aguglia, U.; van der Knaap, M.S.; Heutink, P.; John, S.W.M. Mutations in Col4a1 Cause Perinatal Cerebral Hemorrhage and Porencephaly. *Science* **2005**, *308*, 1167–1171. [[CrossRef](#)] [[PubMed](#)]
45. Gould, D.B.; Phalan, F.C.; van Mil, S.E.; Sundberg, J.P.; Vahedi, K.; Massin, P.; Bousser, M.G.; Heutink, P.; Miner, J.H.; Tournier-Lasserre, E.; et al. Role of COL4A1 in Small-Vessel Disease and Hemorrhagic Stroke. *N. Engl. J. Med.* **2006**, *354*, 1489–1496. [[CrossRef](#)]
46. Pöschl, E.; Schlötzer-Schrehardt, U.; Brachvogel, B.; Saito, K.; Ninomiya, Y.; Mayer, U. Collagen IV Is Essential for Basement Membrane Stability but Dispensable for Initiation of Its Assembly during Early Development. *Dev. Camb. Engl.* **2004**, *131*, 1619–1628. [[CrossRef](#)]
47. Leclech, C.; Natale, C.F.; Barakat, A.I. The Basement Membrane as a Structured Surface—Role in Vascular Health and Disease. *J. Cell Sci.* **2020**, *133*, jcs239889. [[CrossRef](#)]
48. Yurchenco, P.D. Basement Membranes: Cell Scaffoldings and Signaling Platforms. *Cold Spring Harb. Perspect. Biol.* **2011**, *3*, a004911. [[CrossRef](#)]
49. Morrissey, M.A.; Sherwood, D.R. An Active Role for Basement Membrane Assembly and Modification in Tissue Sculpting. *J. Cell Sci.* **2015**, *128*, 1661–1668. [[CrossRef](#)]
50. Sarver, D.C.; Kharaz, Y.A.; Sugg, K.B.; Gumucio, J.P.; Comerford, E.; Mendias, C.L. Sex Differences in Tendon Structure and Function. *J. Orthop. Res. Off. Publ. Orthop. Res. Soc.* **2017**, *35*, 2117–2126. [[CrossRef](#)]
51. Kim, J.M.; Shin, S.-C.; Park, G.-C.; Lee, J.-C.; Jeon, Y.K.; Ahn, S.J.; Thibeault, S.; Lee, B.-J. Effect of Sex Hormones on Extracellular Matrix of Lamina Propria in Rat Vocal Fold. *Laryngoscope* **2020**, *130*, 732–740. [[CrossRef](#)]
52. Soldano, S.; Montagna, P.; Villaggio, B.; Parodi, A.; Gianotti, G.; Sulli, A.; Seriollo, B.; Secchi, M.E.; Cutolo, M. Endothelin and Sex Hormones Modulate the Fibronectin Synthesis by Cultured Human Skin Scleroderma Fibroblasts. *Ann. Rheum. Dis.* **2009**, *68*, 599–602. [[CrossRef](#)] [[PubMed](#)]
53. Kehlet, S.N.; Willumsen, N.; Armbrecht, G.; Dietzel, R.; Brix, S.; Henriksen, K.; Karsdal, M.A. Age-Related Collagen Turnover of the Interstitial Matrix and Basement Membrane: Implications of Age- and Sex-Dependent Remodeling of the Extracellular Matrix. *PLoS ONE* **2018**, *13*, e0194458. [[CrossRef](#)] [[PubMed](#)]
54. Hall, G.; Phillips, T.J. Estrogen and Skin: The Effects of Estrogen, Menopause, and Hormone Replacement Therapy on the Skin. *J. Am. Acad. Dermatol.* **2005**, *53*, 555–568. [[CrossRef](#)] [[PubMed](#)]

55. Freimann, F.B.; Müller, S.; Streitberger, K.-J.; Guo, J.; Rot, S.; Ghori, A.; Vajkoczy, P.; Reiter, R.; Sack, I.; Braun, J. MR Elastography in a Murine Stroke Model Reveals Correlation of Macroscopic Viscoelastic Properties of the Brain with Neuronal Density. *NMR Biomed.* **2013**, *26*, 1534–1539. [[CrossRef](#)]
56. Pakkenberg, B.; Gundersen, H.J. Neocortical Neuron Number in Humans: Effect of Sex and Age. *J. Comp. Neurol.* **1997**, *384*, 312–320. [[CrossRef](#)]
57. Rabinowicz, T.; Petetot, J.M.-C.; Gartside, P.S.; Sheyn, D.; Sheyn, T.; de Courten-Myers, G.M. Structure of the Cerebral Cortex in Men and Women. *J. Neuropathol. Exp. Neurol.* **2002**, *61*, 46–57. [[CrossRef](#)] [[PubMed](#)]
58. Mouton, P.R.; Long, J.M.; Lei, D.-L.; Howard, V.; Jucker, M.; Calhoun, M.E.; Ingram, D.K. Age and Gender Effects on Microglia and Astrocyte Numbers in Brains of Mice. *Brain Res.* **2002**, *956*, 30–35. [[CrossRef](#)]
59. Cahill, L. Why Sex Matters for Neuroscience. *Nat. Rev. Neurosci.* **2006**, *7*, 477–484. [[CrossRef](#)]
60. Chou, X.-L.; Fang, Q.; Yan, L.; Zhong, W.; Peng, B.; Li, H.; Wei, J.; Tao, H.W.; Zhang, L.I. Contextual and Cross-Modality Modulation of Auditory Cortical Processing through Pulvinar Mediated Suppression. *eLife* **2020**, *9*, e54157. [[CrossRef](#)]
61. Fang, Q.; Chou, X.-L.; Peng, B.; Zhong, W.; Zhang, L.I.; Tao, H.W. A Differential Circuit via Retino-Colliculo-Pulvinar Pathway Enhances Feature Selectivity in Visual Cortex through Surround Suppression. *Neuron* **2020**, *105*, 355–369.e6. [[CrossRef](#)]
62. Huang, A.S.; Rogers, B.P.; Sheffield, J.M.; Vandekar, S.; Anticevic, A.; Woodward, N.D. Characterizing Effects of Age, Sex and Psychosis Symptoms on Thalamocortical Functional Connectivity in Youth. *NeuroImage* **2021**, *243*, 118562. [[CrossRef](#)] [[PubMed](#)]
63. Kipp, M.; Nyamoya, S.; Hochstrasser, T.; Amor, S. Multiple Sclerosis Animal Models: A Clinical and Histopathological Perspective. *Brain Pathol.* **2017**, *27*, 123–137. [[CrossRef](#)]
64. Scheld, M.; Rütther, B.J.; Große-Veldmann, R.; Ohl, K.; Tenbrock, K.; Dreytmüller, D.; Fallier-Becker, P.; Zendedel, A.; Beyer, C.; Clarner, T.; et al. Neurodegeneration Triggers Peripheral Immune Cell Recruitment into the Forebrain. *J. Neurosci.* **2016**, *36*, 1410. [[CrossRef](#)] [[PubMed](#)]
65. Guo, J.; Hirsch, S.; Fehlner, A.; Papazoglou, S.; Scheel, M.; Braun, J.; Sack, I. Towards an Elastographic Atlas of Brain Anatomy. *PLoS ONE* **2013**, *8*, e71807. [[CrossRef](#)] [[PubMed](#)]
66. Braun, J.; Guo, J.; Lützkendorf, R.; Stadler, J.; Papazoglou, S.; Hirsch, S.; Sack, I.; Bernarding, J. High-Resolution Mechanical Imaging of the Human Brain by Three-Dimensional Multifrequency Magnetic Resonance Elastography at 7T. *NeuroImage* **2014**, *90*, 308–314. [[CrossRef](#)]
67. Streitberger, K.-J.; Fehlner, A.; Pache, F.; Lacheta, A.; Papazoglou, S.; Bellmann-Strobl, J.; Ruprecht, K.; Brandt, A.; Braun, J.; Sack, I.; et al. Multifrequency Magnetic Resonance Elastography of the Brain Reveals Tissue Degeneration in Neuromyelitis Optica Spectrum Disorder. *Eur. Radiol.* **2017**, *27*, 2206–2215. [[CrossRef](#)] [[PubMed](#)]
68. Moeendarbary, E.; Weber, I.P.; Sheridan, G.K.; Koser, D.E.; Soleman, S.; Haenzi, B.; Bradbury, E.J.; Fawcett, J.; Franze, K. The Soft Mechanical Signature of Glial Scars in the Central Nervous System. *Nat. Commun.* **2017**, *8*, 14787. [[CrossRef](#)]
69. Embry, A.E.; Liu, Z.; Henderson, J.M.; Byfield, F.J.; Liu, L.; Yoon, J.; Wu, Z.; Cruz, K.; Moradi, S.; Gillombardo, C.B.; et al. Similar Biophysical Abnormalities in Glomeruli and Podocytes from Two Distinct Models. *J. Am. Soc. Nephrol. JASN* **2018**, *29*, 1501–1512. [[CrossRef](#)]
70. Rempe, R.G.; Hartz, A.M.; Bauer, B. Matrix Metalloproteinases in the Brain and Blood-Brain Barrier: Versatile Breakers and Makers. *J. Cereb. Blood Flow Metab.* **2016**, *36*, 1481–1507. [[CrossRef](#)]
71. Sobel, R.A. The Extracellular Matrix in Multiple Sclerosis: An Update. *Braz. J. Med. Biol. Res.* **2001**, *34*, 603–609. [[CrossRef](#)]
72. Zeis, T.; Kinter, J.; Herrero-Herranz, E.; Weissert, R.; Schaeren-Wiemers, N. Gene Expression Analysis of Normal Appearing Brain Tissue in an Animal Model for Multiple Sclerosis Revealed Grey Matter Alterations, but Only Minor White Matter Changes. *J. Neuroimmunol.* **2008**, *205*, 10–19. [[CrossRef](#)] [[PubMed](#)]
73. Lassmann, H. Pathogenic Mechanisms Associated With Different Clinical Courses of Multiple Sclerosis. *Front. Immunol.* **2019**, *9*, 3116. [[CrossRef](#)] [[PubMed](#)]
74. Ulbrich, P.; Khoshneviszadeh, M.; Jandke, S.; Schreiber, S.; Dityatev, A. Interplay between Perivascular and Perineuronal Extracellular Matrix Remodelling in Neurological and Psychiatric Diseases. *Eur. J. Neurosci.* **2021**, *53*, 3811–3830. [[CrossRef](#)] [[PubMed](#)]
75. Jang, D.G.; Sim, H.J.; Song, E.K.; Kwon, T.; Park, T.J. Extracellular Matrixes and Neuroinflammation. *BMB Rep.* **2020**, *53*, 491–499. [[CrossRef](#)] [[PubMed](#)]
76. Streitberger, K.-J.; Lilaj, L.; Schrank, F.; Braun, J.; Hoffmann, K.-T.; Reiss-Zimmermann, M.; Käs, J.A.; Sack, I. How Tissue Fluidity Influences Brain Tumor Progression. *Proc. Natl. Acad. Sci. USA* **2020**, *117*, 128–134. [[CrossRef](#)] [[PubMed](#)]
77. Chaudhuri, O.; Cooper-White, J.; Janmey, P.A.; Mooney, D.J.; Shenoy, V.B. The Impact of Extracellular Matrix Viscoelasticity on Cellular Behavior. *Nature* **2020**, *584*, 535–546. [[CrossRef](#)]
78. Elosegui-Artola, A. The Extracellular Matrix Viscoelasticity as a Regulator of Cell and Tissue Dynamics. *Curr. Opin. Cell Biol.* **2021**, *72*, 10–18. [[CrossRef](#)]
79. Van Wageningen, T.A.; Antonovaite, N.; Paardekam, E.; Brevé, J.J.P.; Iannuzzi, D.; van Dam, A.-M. Viscoelastic Properties of White and Gray Matter-Derived Microglia Differentiate upon Treatment with Lipopolysaccharide but Not upon Treatment with Myelin. *J. Neuroinflammation* **2021**, *18*, 83. [[CrossRef](#)]
80. Previtera, M.L.; Langhammer, C.G.; Firestein, B.L. Effects of Substrate Stiffness and Cell Density on Primary Hippocampal Cultures. *J. Biosci. Bioeng.* **2010**, *110*, 459–470. [[CrossRef](#)]

81. Georges, P.C.; Miller, W.J.; Meaney, D.F.; Sawyer, E.S.; Janney, P.A. Matrices with Compliance Comparable to That of Brain Tissue Select Neuronal over Glial Growth in Mixed Cortical Cultures. *Biophys. J.* **2006**, *90*, 3012–3018. [[CrossRef](#)]
82. Urbanski, M.M.; Kingsbury, L.; Moussouros, D.; Kassim, I.; Mehjabeen, S.; Paknejad, N.; Melendez-Vasquez, C.V. Myelinating Glia Differentiation Is Regulated by Extracellular Matrix Elasticity. *Sci. Rep.* **2016**, *6*, 33751. [[CrossRef](#)] [[PubMed](#)]

Publication 3: Brain inflammation induces alterations in glycosaminoglycan metabolism and subsequent changes in CS-4S and hyaluronic acid

Journal Data Filtered By: **Selected JCR Year: 2020** Selected Editions: SCIE, SSCI
 Selected Categories: **"BIOCHEMISTRY and MOLECULAR BIOLOGY"** Selected
 Category Scheme: WoS
Gesamtanzahl: 297 Journale

Rank	Full Journal Title	Total Cites	Journal Impact Factor	Eigenfactor Score
1	NATURE MEDICINE	114,401	53.440	0.184050
2	CELL	320,407	41.582	0.526960
3	Molecular Cancer	24,931	27.401	0.030030
4	Annual Review of Biochemistry	24,394	23.643	0.021450
5	Signal Transduction and Targeted Therapy	3,848	18.187	0.005730
6	MOLECULAR CELL	86,299	17.970	0.161840
7	TRENDS IN MICROBIOLOGY	17,553	17.079	0.022820
8	NUCLEIC ACIDS RESEARCH	248,139	16.971	0.387070
9	MOLECULAR BIOLOGY AND EVOLUTION	61,557	16.240	0.082270
10	PROGRESS IN LIPID RESEARCH	7,328	16.195	0.004530
11	MOLECULAR PSYCHIATRY	28,622	15.992	0.046220
12	CELL DEATH AND DIFFERENTIATION	27,701	15.828	0.028730
13	NATURE STRUCTURAL & MOLECULAR BIOLOGY	32,038	15.369	0.051210
14	Nature Chemical Biology	27,428	15.040	0.047880
15	MOLECULAR ASPECTS OF MEDICINE	8,136	14.235	0.006640
16	TRENDS IN BIOCHEMICAL SCIENCES	22,003	13.807	0.025760
17	NATURAL PRODUCT REPORTS	13,293	13.423	0.011160
18	Molecular Plant	15,778	13.164	0.026860
19	Advances in Carbohydrate Chemistry and Biochemistry	752	12.200	0.000200
20	TRENDS IN MOLECULAR MEDICINE	13,213	11.951	0.014720

Rank	Full Journal Title	Total Cites	Journal Impact Factor	Eigenfactor Score
21	Redox Biology	15,982	11.799	0.024930
22	EMBO JOURNAL	76,189	11.598	0.055000
23	MATRIX BIOLOGY	8,972	11.583	0.011010
24	Molecular Systems Biology	10,149	11.429	0.016300
25	PLANT CELL	64,794	11.277	0.036260
26	CURRENT BIOLOGY	78,289	10.834	0.116100
27	BIOCHIMICA ET BIOPHYSICA ACTA- REVIEWS ON CANCER	7,025	10.680	0.007000
28	Cell Systems	5,813	10.304	0.035330
29	ONCOGENE	77,576	9.867	0.059180
30	CELLULAR AND MOLECULAR LIFE SCIENCES	34,003	9.261	0.033790
31	GENOME RESEARCH	47,141	9.043	0.064690
32	CURRENT OPINION IN CHEMICAL BIOLOGY	12,240	8.822	0.014190
33	EMBO REPORTS	19,502	8.807	0.027490
34	EXPERIMENTAL AND MOLECULAR MEDICINE	8,780	8.718	0.013260
35	ANTIOXIDANTS & REDOX SIGNALING	26,971	8.401	0.016700
36	CRITICAL REVIEWS IN BIOCHEMISTRY AND MOLECULAR BIOLOGY	4,576	8.250	0.005370
37	Science Signaling	15,954	8.192	0.023910
38	Cell Chemical Biology	5,236	8.116	0.018050
39	PLOS BIOLOGY	39,598	8.029	0.059920
40	Essays in Biochemistry	3,629	8.000	0.006450
41	BIOINORGANIC CHEMISTRY AND APPLICATIONS	1,406	7.778	0.000890

Rank	Full Journal Title	Total Cites	Journal Impact Factor	Eigenfactor Score
42	Acta Crystallographica Section D-Structural Biology	23,670	7.652	0.020190
43	CYTOKINE & GROWTH FACTOR REVIEWS	7,650	7.638	0.005850
44	FREE RADICAL BIOLOGY AND MEDICINE	52,714	7.376	0.034180
45	Computational and Structural Biotechnology Journal	3,620	7.271	0.006770
46	AMYLOID-JOURNAL OF PROTEIN FOLDING DISORDERS	2,202	7.141	0.003280
47	Cell and Bioscience	3,184	7.133	0.004320
48	Genes & Diseases	1,850	7.103	0.003170
49	Molecular Ecology Resources	13,390	7.090	0.016690
50	Journal of Integrative Plant Biology	6,749	7.061	0.006430
51	BIOMACROMOLECULES	45,724	6.988	0.026020
52	INTERNATIONAL JOURNAL OF BIOLOGICAL MACROMOLECULES	79,246	6.953	0.073720
53	AMERICAN JOURNAL OF RESPIRATORY CELL AND MOLECULAR BIOLOGY	15,280	6.914	0.015050
54	International Review of Cell and Molecular Biology	3,057	6.813	0.004320
55	CURRENT OPINION IN STRUCTURAL BIOLOGY	12,448	6.809	0.018970
56	PROTEIN SCIENCE	16,581	6.725	0.021220
57	International Journal of Biological Sciences	10,778	6.580	0.010540
58	Open Biology	4,059	6.411	0.010280
59	MOLECULAR MEDICINE	6,239	6.354	0.004460
60	Antioxidants	9,076	6.312	0.009480
61	JOURNAL OF PHOTOCHEMISTRY AND PHOTOBIOLOGY B-BIOLOGY	17,015	6.252	0.012740

<https://doi.org/10.1016/j.ijbiomac.2023.123214>

<https://doi.org/10.1016/j.ijbiomac.2023.123214>

<https://doi.org/10.1016/j.ijbiomac.2023.123214>

<https://doi.org/10.1016/j.ijbiomac.2023.123214>

<https://doi.org/10.1016/j.ijbiomac.2023.123214>

<https://doi.org/10.1016/j.ijbiomac.2023.123214>

<https://doi.org/10.1016/j.ijbiomac.2023.123214>

<https://doi.org/10.1016/j.ijbiomac.2023.123214>

<https://doi.org/10.1016/j.ijbiomac.2023.123214>

<https://doi.org/10.1016/j.ijbiomac.2023.123214>

Curriculum Vitae

My curriculum vitae does not appear in the electronic version of my paper for reasons of data protection.

My curriculum vitae does not appear in the electronic version of my paper for reasons of data protection.

Publication list

Silva, R.V., Morr, A. S., Herthum H., Koch, S. P., Mueller S., Batzdorf C.S, Bertalan G., Meyer T., Tzschätzsch H., Kühl A.A., Boehm-Sturm, P., Braun, J., Scheel M., Paul F., Infante-Duarte C., Sack I. (2023). Cerebral tomoelastography detects cortical softening in correlation with disease course in multiple sclerosis. **Manuscript under review.** *Advanced sciences*.

Silva, R.V., Biskup, K., Zabala-Jouvin, J. K., Batzdorf, C. S., Stellmach, C., Morr, A. S., Sack, I., Ludwig, A., Blanchard, V., & Infante-Duarte, C. (2023). Brain inflammation induces alterations in glycosaminoglycan metabolism and subsequent changes in CS-4S and hyaluronic acid. *International journal of biological macromolecules*, 230, 123214. Advance online publication. <https://doi.org/10.1016/j.ijbiomac.2023.123214>
Journal Impact Factor (2022): **8.025**

Morr, A. S., Nowicki, M., Bertalan, G., **Vieira Silva, R.**, Infante Duarte, C., Koch, S. P., Boehm-Sturm, P., Krügel, U., Braun, J., Steiner, B., Käs, J. A., Fuhs, T., & Sack, I. (2022). Mechanical properties of murine hippocampal subregions investigated by atomic force microscopy and in vivo magnetic resonance elastography. *Scientific reports*, 12(1), 16723. <https://doi.org/10.1038/s41598-022-21105-7>
Journal Impact Factor (2022): **4.996**

Anderhalten, L., **Silva, R. V.**, Morr, A., Wang, S., Smorodchenko, A., Saatz, J., Traub, H., Mueller, S., Boehm-Sturm, P., Rodriguez-Sillke, Y., Kunkel, D., Hahndorf, J., Paul, F., Taupitz, M., Sack, I., & Infante-Duarte, C. (2022). Different Impact of Gadopentetate and Gadobutrol on Inflammation-Promoted Retention and Toxicity of Gadolinium Within the Mouse Brain. *Investigative radiology*, 57(10), 677–688. <https://doi.org/10.1097/RLI.0000000000000884>
Journal Impact Factor (2022): **10.065**

Lohmeier, J., **Silva, R. V.**, Tietze, A., Taupitz, M., Kaneko, T., Prüss, H., Paul, F., Infante-Duarte, C., Hamm, B., Caravan, P., & Makowski, M. R. (2022). Fibrin-targeting molecular MRI in inflammatory CNS disorders. *European journal of nuclear medicine and molecular imaging*, 49(11), 3692–3704. <https://doi.org/10.1007/s00259-022-05807-8>

Journal Impact Factor (2022): **10.057**

Batzdorf, C. S., Morr, A. S., Bertalan, G., Sack, I., **Silva, R. V.**, & Infante-Duarte, C. (2022). Sexual Dimorphism in Extracellular Matrix Composition and Viscoelasticity of the Healthy and Inflamed Mouse Brain. *Biology*, *11*(2), 230. <https://doi.org/10.3390/biology11020230>

Journal Impact Factor (2022): **5.168**

Silva, R. V., Morr, A. S., Mueller, S., Koch, S. P., Boehm-Sturm, P., Rodriguez-Sillke, Y., Kunkel, D., Tzschätzsch, H., Kühl, A. A., Schnorr, J., Taupitz, M., Sack, I., & Infante-Duarte, C. (2021). Contribution of Tissue Inflammation and Blood-Brain Barrier Disruption to Brain Softening in a Mouse Model of Multiple Sclerosis. *Frontiers in neuroscience*, *15*, 701308. <https://doi.org/10.3389/fnins.2021.701308>

Journal Impact Factor (2021): **5.152**

Guo, J., Bertalan, G., Meierhofer, D., Klein, C., Schreyer, S., Steiner, B., Wang, S., **Vieira da Silva, R.**, Infante-Duarte, C., Koch, S., Boehm-Sturm, P., Braun, J., & Sack, I. (2019). Brain maturation is associated with increasing tissue stiffness and decreasing tissue fluidity. *Acta biomaterialia*, *99*, 433–442. <https://doi.org/10.1016/j.actbio.2019.08.036>

Journal Impact Factor (2019): **7.242**

Schartner, E., Sabbir, M. G., Saleh, A., **Silva, R. V.**, Roy Chowdhury, S., Smith, D. R., & Fernyhough, P. (2018). High glucose concentration suppresses a SIRT2 regulated pathway that enhances neurite outgrowth in cultured adult sensory neurons. *Experimental neurology*, *309*, 134–147. <https://doi.org/10.1016/j.expneurol.2018.08.001>

Journal Impact Factor (2018): **4.562**

Silva, R. V., Oliveira, J. T., Santos, B. L. R., Dias, F. C., Martinez, A. M. B., Lima, C. K. F., & Miranda, A. L. P. (2017). Long-Chain Omega-3 Fatty Acids Supplementation Accelerates Nerve Regeneration and Prevents Neuropathic Pain Behavior in Mice. *Frontiers in pharmacology*, *8*, 723. <https://doi.org/10.3389/fphar.2017.00723>

Journal Impact Factor (2017): **4.400**

Lima, C. K., Silva, R. M., Lacerda, R. B., Santos, B. L., **Silva, R. V.**, Amaral, L. S., Quintas, L. E., Fraga, C. A., Barreiro, E. J., Guimaraes, M. Z., & Miranda, A. L. (2014). LASSBio-1135: a dual TRPV1 antagonist and anti-TNF-alpha compound orally effective in models of inflammatory and neuropathic pain. *PloS one*, 9(6), e99510. <https://doi.org/10.1371/journal.pone.0099510>
Journal Impact Factor (2014): **3.234**

Acknowledgments

First and foremost, I would like to sincerely thank my supervisor, Prof. Dr. rer. nat. Carmen Infante Duarte, for taking me in, giving me the opportunity to learn and grow in her lab, supervising this thesis. Without her support this thesis would have not been possible. Thank you from the heart.

I also appreciate immensely working with Anna Morr and the time we spent together sharing ideas, concerns, knowledge, and experiments that resulted in many publications and times of joy.

I thank all the collaborators participating the papers that are part of this thesis. In special, Ingolf Sack and his group for providing support with the imaging experiments. Prof Veronique Blanchard and Dr Karina Biskup for collaborating with the glycosaminoglycan analysis as well as PD Dr. Antje Ludwig for her expertise and fruitful discussions on the project.

During my time at AG Infante, I gladly met wonderful people. Some for a short period, others were there for as long as I can remember. I thank each one of you for the support, discussions, suggestions, and moments shared. My heartfelt thanks to Alba del Rio Serrato, Bibiane Seeger, Bimala Mala, Borja Latorre, Clara Batzdorf, Silvina Romero, Maria Schroeder, Roemel Bueno, Julian Bossenmaier, Juliana Garcia Campo, Lina Anderhalten, Maren Malla, Moataz Alabdullah, Natascha Asselborn, Shuanqing Wang, Soledad Romero Tamudo as well as many others whose paths I crossed.

I thank my family for providing me with unconditional support, especially after I moved across the globe to conduct impactful research.

Finally, a special thanks must go to Leonardo Barros, for the support given in the times of need in the course of my PhD, especially for all his assistance and patience troubleshooting my scripts.

In memory of my beloved mother who has given me unconditional support and was so proud of this achievement.